

**Development of Magnetic Refrigerants for Active Magnetic
Regenerative Refrigerators**

by

**Christopher E. J. Reid
B. Sc., University of Manitoba, 1990**

A Thesis Submitted in Partial Fulfilment of the Requirements for the
Degree of

MASTER OF APPLIED SCIENCE

in the Department of Mechanical Engineering

We accept this thesis as conforming to the required standard

[REDACTED]

Dr. John A. Barclay, Supervisor (Department of Mechanical Engineering)

[REDACTED]

Dr. Hans-Holger Rogner, Departmental Member (Department of Mechanical Engineering)

[REDACTED]

Dr. David Harrington, Outside Member (Department of Chemistry)

[REDACTED]

Dr. Pier Schurer, External Examiner (Department of Physics, Royal Roads Military College)

© Christopher E. J. Reid, 1995

University of Victoria

All rights reserved. This thesis may not be reproduced in whole or in part, by photocopy or other means, without the permission of the author.

Abstract

The Cryofuel Systems Group (CFS) was formed as a part of the Institute for Integrated Energy Systems (IESVic) to design and build a cost effective natural gas (NG) refuelling system. A key component of the refuelling system is the liquefier. CFS is developing an active magnetic regenerative refrigerator (AMRR) as a potentially economical means of efficiently liquefying the NG. A magnetic regenerator is the heart of the AMRR device. It provides the thermodynamic work and the passive regeneration to allow the AMRR to operate over large temperature spans. This thesis deals with the development of the magnetic refrigerants that will comprise the regenerator of a prototype that will span from 110 K to 240 K with a cooling power of 700 W. The work has been broken into four parts: selection of the magnetic refrigerants, preparation and characterization of selected materials, manufacture of high performance active magnetic regenerators from the magnetic refrigerants, and testing of fabricated regenerators.

An AMRR is a complicated thermodynamic system that is composed of two interlinked subsystems, the magnetic refrigerant and the circulating heat transfer fluid. To properly select magnetic refrigerants for the AMRR, two fundamental criteria must be satisfied: (1) the material must provide the required temperature difference to the heat transfer fluid at the hot and cold boundaries of the device to allow the specified cooling load (with the net

work and any entropy created) to be pumped and deposited to the environment, and (2) the magnetic material must do enough net work to satisfy a first law thermodynamic energy balance.


When selecting magnetic materials for the AMRR, the fundamental screening characteristic is magnetic entropy change per unit volume of the refrigerant as a function of applied field and temperature. For the temperature range of interest in the prototype, heavy rare earth elements and intra-rare earth alloys are excellent choices because they not only have large magnetic entropy changes, but they are also have good formability characteristics. Several refrigerants must be layered in the regenerator to meet the above selection criteria and to allow the transient start-up of the device. The materials chosen for the prototype AMRR were elemental dysprosium and three alloys of gadolinium and dysprosium.

The selected AMRR materials must be manufactured into highly effective regenerator geometries. Wire screen and packed particle bed geometries offer the best compromise at this time between performance and manufacturing ease. To make an effective packed particle bed, $100\pm 20\mu\text{m}$ particles were manufactured using a rotating plasma arc atomization method. This technique produced high quality dysprosium particles with an effective yield of 29%. Special tests were conducted that showed the bulk resistivity of the $100\mu\text{m}$ particles is at least 13 orders of magnitude greater than pure dysprosium. This makes entropy production due to predicted eddy currents negligible.


As is the case with particles, highly effective wire screen geometries require

very fine media and hence, the availability of small diameter rare earth wire. Dysprosium was successfully drawn to a diameter of $66\mu\text{m}$ but began to break at this point because the original as-cast grain structure was not treated. Indications are that with an initial hot swage, the wire can be drawn to $\sim 25\mu\text{m}$. To our knowledge, this is the first time such wire has been made, and it gives the capability to weave up to 400 mesh screens. Because of the high set-up cost of fine screen weaving with new and unfamiliar material, packed particle beds were chosen for the prototype. Fine mesh wire screens will theoretically outperform packed particles when considering the AMRR prototype operating conditions. If the experimental performance is as excellent, the cost of future development will be justified. Randomly stacked mats of these wires may be a practical alternative.

Examiners:




Dr. John A. Barclay, Supervisor (Department of Mechanical Engineering)



Dr. Hans-Holger Rogner, Departmental Member (Department of Mechanical Engineering)



Dr. David Harrington, Outside Member (Department of Chemistry)



Dr. Pier Schurer, External Examiner (Department of Physics, Royal Roads Military College)

Table of Contents

List of Figures	x
List of Tables	xiv
Nomenclature	xvi
Acknowledgements	xix
1. Introduction	1
1.1 Motivation	1
1.2 Thesis Objectives	6
1.2.1 Overall AMRR Project	6
1.2.2 Thesis Focus	7
1.3 Theory Behind Active Magnetic Regenerative Refrigerators (AMRR)	7
1.3.1 General Concept	7
1.3.2 Active Magnetic Regenerators	9
1.3.3 Prototype System Configuration and Operation	11
1.3.4 The Magnetocaloric Effect	15
1.3.4.1 The Lanthanide Series	16
1.3.4.2 ΔT_{ad} vs T Curves for the Lanthanides	17
1.4 Relevant Prior Work	18
1.4.1 Selection of Magnetic Materials for the AMRR	18

1.4.2 Preparation of Rare Earth Magnetic Materials	21
1.4.3 Characterization of Rare Earth Magnetic materials	21
1.4.4 Analysis of High Performance Regenerators	22
1.4.4.1 Passive Regenerator Analysis	22
1.4.4.2 Active Regenerator Analysis	23
1.4.5 Manufacture of Regenerators From Rare Earth Magnetic Materials	24
1.4.5.1 Passive Regenerator Manufacture	24
1.4.5.2 Active Regenerator Manufacture	24
2. Selection of Magnetic Materials for the AMRR	26
2.1 Thermodynamic Requirements	26
2.1.1 Detailed AMRR Operation	26
2.1.2 Material Selection Criteria	33
2.2 Reversible AMRRs	34
2.3 Real AMRRs	39
2.3.1 ΔT_{ad} Boundary Conditions Criteria	42
2.3.2 Work Criteria	44
2.3.3 ΔT_{ad} versus T Profile (or active work distribution) Considerations	46
2.3.4 Material Mass Optimizing Considerations	48
2.4 Real Material Selection	49
2.4.1 Ferromagnetic Materials	49
2.4.2 Boundary ΔT_{ad} Criteria	50
2.4.3 Required Work Criteria	51
2.4.4 Transient Start-up Concerns	52
2.4.5 Selected Material Mass Optimization	52
2.4.6 Other Material Properties	55

3. Preparation of Magnetic Materials	57
3.1 Selected Alloys	57
3.2 Commercial Grade Rare Earth Materials	58
3.3 Alloy Preparation	59
3.3.1 Arc Melting	59
3.3.2 Sample Mounting and Polishing	59
3.3.3 Etching	60
3.4 Sample Verification	61
3.4.1 Photomicroscopy	62
3.4.2 Scanning Electron Microscopy (SEM)	62
4. Characterization of Selected Magnetic Materials	63
4.1 Physical Properties	63
4.1.1 Oxide Layer Formation	64
4.2 Magnetic Properties	65
4.2.1 Magnetocaloric Effect	66
4.2.2 Magnetic Hysteresis	70
4.3 Transport Properties	71
4.4 Mechanical Properties	73
4.5 Elastic Properties	75
5. Manufacture of High Performance Active Magnetic Regenerator Media	76
5.1 Selection of Regenerator Geometries	76
5.1.1 Discussion of Important AMRR Regenerator Design Parameters	77
5.1.2 Selection of Potential AMR Geometries	81
5.1.3 In-depth Parametric Analysis of Chosen AMRR Geometries	83

5.2 Manufacture of Particles From Magnetic Materials	87
5.2.1 Spherical Particles	87
5.2.1.1 Gas Atomization	87
5.2.1.2 Centrifugal Atomization	89
5.2.2 Irregular-shaped Particles	95
5.3 Manufacture of Wire From Magnetic Materials	96
5.3.1 Experimental Method and Results	96
5.3.2 Wire Screens	100
5.4 Manufacturing Cost Considerations in Selecting Regenerator Geometries	100
6. Testing Regenerator Geometries	102
6.1 Identifying Parameters to Test	102
6.2 Regenerator Eddy Current Generation	103
6.2.1 Methodology and Test Apparatus	103
6.2.3 Results	104
6.3 Effective Longitudinal Conductivity Tests	106
6.3.1 Methodology and Test Apparatus	107
6.3.2 Computer Simulation	109
7. Conclusions and Future Work	110
7.1 Conclusions	110
7.2 Future Work	113
8. References	115

Appendix A

Evaluation of the Adiabatic Temperature Change of Magnetic Materials .	123
A.1 Direct Measurement	123
A.2 Measurement of Specific Heat and Magnetization Data	123
A.3 Measurement of Specific Heat Data	124
A.4 Measurement of Magnetization Data	125

Appendix B

Calculations of Boundary ΔT_{ad} for a Real AMRR	126
B.1 Calculating $\Delta T_{ad,c}$	126
B.2 Calculating $\Delta T_{ad,h}$	128

Appendix C

Other Investigated Magnetic Refrigerants	132
--	-----

Appendix D

Regenerator Simulation Computer Program	135
---	-----

List of Figures

Figure 1.1a: Geographic distribution of identified reserves and cumulative production of natural gas as of January 1990, and undiscovered resources as of January 1991	3
Figure 1.3.1a: Magnetic Cycle processes (with gas cycle analogues)	8
Figure 1.3.2a: Material temperature profiles for AMRR	10
Figure 1.3.3a: Wheel-shaped rotary AMRR prototype design	12
Figure 1.3.3b: Details of regenerator compartments in the rotary AMRR prototype	14
Figure 1.3.4a: Dipole magnetization of a simple ferromagnet	15
Figure 1.3.4.1a: Lanthanide (rare earth) elements	17
Figure 1.3.4.2a: ΔT_{ad} vs T Curves	18
Figure 2.1.1a: Heat flow among the AMRR thermodynamic subsystems ..	28
Figure 2.1.1b: T-s diagram for a single material element of an active magnetic regenerator undergoing a magnetic Ericsson cycle	30

Figure 2.1.1c: (i) Single elemental AMRR material executing brayton cycle. (ii) Series of magnetic elements undergoing unique AMRR cycle	32
Figure 2.2a: (i) Envelope of T-s diagram of single material for a reversible AMRR. (ii) ΔT_{ad} vs T profile of the same material	37
Figure 2.2b: Possible ΔT_{ad} vs T profiles that satisfy reversible AMRR requirements	38
Figure 2.3.2a: (i) Envelope of T-s diagram of single material for real AMRR. (ii) ΔT_{ad} vs T profile of same material	45
Figure 2.3.3a: Typical passive regenerator temperature vs radius profile ..	46
Figure 2.3.3b: Possible monotonically increasing T vs radius profiles	48
Figure 2.4.4a: (i) Superimposed adiabatic temperature change profiles of the selected materials over the operating temperature range with six Tesla applied field. (ii) Resulting composite adiabatic temperature change profile after cropping	54
Figure 3.4a: Phase diagram of the Dy-Gd system	61
Figure 4.2.1a: T/c_H vs absolute temperature and field for dysprosium	66
Figure 4.2.1b: Magnetic ordering temperatures for Gd-Dy alloys	69

Figure 4.2.2a: Magnetic hysteresis curve for a typical ferromagnetic material operating near its ordering temperature	70
Figure 4.3a: C-Axis electrical resistivity of some heavy rare earth metals as a function of temperature	71
Figure 4.3b: Specific heat (i) of dysprosium and (ii) gadolinium as a function of temperature	72
Figure 4.4a: Room temperature tension-tension fatigue life curves for yttrium, dysprosium, and erbium with maximum tensile stress give in terms of the fraction of respective ultimate tensile strengths	74
Figure 5.1.2a: Possible regenerator geometries	81
Figure 5.1.3a: FOM of particle and wire screen regenerator geometries for prototype AMRR flow conditions.	86
Figure 5.2.1.1a: Schematic of gas atomization apparatus	88
Figure 5.2.1.2a: Two-step RSR atomization process	91
Figure 5.2.1.2b: Single-step REP atomization process	92
Figure 5.2.1.2c: Nuclear Metals REP and PREP apparatus	93
Figure 5.2.1.2d: SEM of ~100 micron dysprosium particles produced using single-step REP atomization process	94

Figure 5.3.1a: Schematic of billet used to hot extrude dysprosium	97
Figure 5.3.1b: 200X micrograph of cross section of material composite showing the Dy core, Nb barrier, and the Cu jacket	98
Figure 6.2.1a: Schematic of regenerator resistance testing device	104
Figure 6.2.3a: Resistivity vs. plate pressure for 100 micron diameter dysprosium particle bed	105
Figure 6.3.1a: Example of possible temperature vs. time profiles for selected points along a test regenerator bed	107
Figure 6.3.1b: Schematic of device used to obtain temperature/time profiles for regenerator beds	108
Figure C.1: Magnetic phase diagram for Tb-Yb alloy system	133

List of Tables

Table 1.1a: CARB emission standards for light-duty vehicles	4
Table 1.1b: CARB minimum phase-in schedule (up to year 2000) for lightduty vehicles	4
Table 2.4.3a: Chosen Magnetic Materials for the AMRR Prototype	52
Table 2.3a: Quoted Prices for some Heavy Rare Earth Materials	56
Table 3.2a: Chemical Analysis of 99.9% Pure Dysprosium Ingot	58
Table 3.3a: Grinding and Polishing Sequence for Heavy Rare Earth Alloys	60
Table 4.1a: Room temperature physical properties of the heavy rare earth metals and their melting and boiling points	64
Table 4.2a: Selected magnetic properties of the heavy rare earth metals ...	65
Table 4.2.1a: Magnetic structures of heavy rare earth metals	68

Table 4.3a: Transport properties of some of the rare earth metals	71
Table 4.4a: Room temperature mechanical properties of several heavy rare earth metals	73
Table 4.4b: Impact properties of heavy rare earths	74
Table 4.5a: Elastic properties of some heavy rare earth metals at room temperature	75
Table 5.2.1.2a: Common centrifugal atomization processes for the production of metal powders	89
Table 5.2.1.2b: Particle distribution and masses of Dy PREP trial run	93
Table 5.3.1a: Diameter, length and description of wire samples delivered.	98

Nomenclature

a_c = frontal (cross sectional) area of regenerator bed (m^2)

a_f = regenerator minimum free flow area, $a_c \alpha$ (m^2)

a_s = regenerator heat transfer area (m^2)

c_p = constant pressure specific heat of fluid (J/kgK)

c_H = specific heat of solid at constant field (J/kgK)

c_s = specific heat of solid (J/kgK)

COP = coefficient of performance (dimensionless)

d_h = hydraulic diameter (m)

d_p = particle diameter (m)

f = friction factor (dimensionless)

G = regenerator fluid flow mass velocity, m_f/a_c (kg/sm^2)

H = applied magnetic field (A/m)

L = regenerator bed flow length (m)

m = specific magnetization of solid (Am^2/kg)

\dot{m}_f = heat transfer fluid mass flow rate (kg/s)

$\dot{m}_{s,active}$ = material mass flow rate to perform required power (kg/s)

$\dot{m}_{s,passive}$ = material mass flow rate to perform required regeneration (kg/s)

N_{tu} = number of heat transfer units (dimensionless)

Pr = Prandlt number (dimensionless)

\dot{Q}_c = cooling power (W)

\dot{Q}_h = heat rejection (W)

\dot{Q}_r = heat transferred in regenerator between solid and fluid (W)

\dot{Q}_{nf} = heat transfer between fluid and solid in the no-flow region (W)

R = universal gas constant (J/molK)

Re = Reynold's number (dimensionless)

\dot{S}_{cond} = entropy generated by longitudinal heat conduction effects (W/K)

\dot{S}_{ht} = entropy generated by finite heat transfer between solid and fluid in flow region (W/K)

\dot{S}_{pdrop} = entropy generated by viscous dissipation of energy in regenerator (W/K)

\dot{S}_{void} = entropy generated by finite heat transfer between solid and fluid in no-flow region (W/K)

St = Stanton number (dimensionless)

T = absolute temperature (K)

T_c = average cold end heat transfer temperature (K)

T_h = average hot end heat transfer temperature (K)

T_{nf} = average no-flow heat transfer temperature (K)

\dot{V}_f = volumetric flow rate (m³/s)

V_{reg} = regenerator bed flow volume (m³)

V_T = total regenerator bed volume (m³)

\dot{W}_{rev} = reversible work rate (W)

\dot{W}_{net} = net cycle work rate (W)

α = porosity (dimensionless)

ΔP = fluid pressure drop across regenerator bed (Pa)

Δs_m = specific magnetic entropy change in solid (J/kgK)

ΔT_{ad} = adiabatic temperature change of the magnetic regenerative material (K)

ΔT_c = cold end heat exchanger temperature change (K)

ΔT_h = hot end heat exchanger temperature change (K)

ΔT_{ht} = average temperature difference between solid and fluid caused by finite heat transfer coefficient (K)

ΔT_{nf} = average temperature difference between solid and fluid caused by finite heat transfer coefficient in the no-flow region (K)

ΔT_{void} = temperature change in solid caused by energy dilution of solid by entrained fluid in no-flow region (K)

ΔT_{wash} = average temperature change in solid caused by energy dilution or 'washing' of solid by fluid in flow region (K)

η_{reg} = regenerator efficiency (reversible work/actual work)

λ = overall effective thermal conductivity in regenerator bed (W/mK)

μ = dynamic viscosity (kg/ms)

μ_o = magnetic permeability of free space (N/A²)

ρ = density (kg/m³)

τ_o = unit surface shear stress (Pa/m²)

Acknowledgements

First and foremost, I would like to thank my supervisor, John Barclay, for his guidance and support over the past years, and, equally as important, for creating a work atmosphere that was both challenging and genuinely enjoyable. I also wish to thank the whole group at IESVic and Cryofuel Systems, including fellow graduate students, post docs, and support staff. This is an exceptional group of people who made July days in L-Hut almost seem bearable.

I am grateful for the research opportunity that was made possible by funding from NSERC and Centra Gas. I am also grateful for the facilities and assistance provided by Royal Military College, Defence Research Establishment Pacific (DREP), and the Université du Québec á Trois-Rivières (UQTR).

Finally, I wish to thank my friends and family (besonders meiner Freundin, Ulrike) for their support, patience and encouragement.

Chapter 1

Introduction

1.1 Motivation

The Cryofuel System Group (CFS) is part of the Institute for Integrated Energy Systems (IESVic), a centre at the University of Victoria. One of the goals of IESVic members is to identify technological barriers and attractors in the transportation energy system. Once the attractors and barriers have been identified, the Institute members search for ways to promote the attractors, knock down the barriers, and create economic opportunities for Canada. CFS was formed to implement technical solutions that will help achieve some of these objectives.

IESVic members recognize that the transportation system evolution will be guided by the world's increased utilization of low-carbon and carbon-free fuels such as natural gas (NG) or hydrogen. The main identified attractors for the use of low or no carbon fuels are abated air pollution and reduction in the dependence on foreign oil. The major identified barrier to the wide spread adoption of non-conventional fuels is unfavourable economics.

- Foreign oil dependence - North America uses over 85 quadrillion kJs of energy annually and the transportation sector accounts for about 25% of

this total. Currently, alternative fuels supply less than 1% of the transportation energy market, the rest is oil-derived. The transportation market makes up about 60% of North America's oil consumption. As of 1994, the United States imported 61% of its crude oil [1]. The large dependence on foreign oil prompted the 1992 National Energy Policy Act (EPACT) in the U.S.. EPACT mandates that federal and alternative fuel provider fleets must convert to alternative fuel vehicles (AFVs) by a set schedule beginning in 1994. If the EPACT goal of reducing oil imports by 10% in 2000 and 30% in 2010 begins to look improbable, EPACT will include municipal and private fleets in its mandate. Under EPACT regulations, super-clean diesel and reformulated gasoline are not considered alternative fuels [2]. The only alternative fuels that are best capable of supplying the North America transportation sector are NG (and hydrogen in the distant future). Natural gas is an abundant fuel that is better distributed globally than oil. Figure 1.1a shows the geographic distribution of ultimate resources of conventional natural gas in the world as of 1990. Using the values in Figure 1.1a and factoring in consumed supplies, North America has identified reserves extending for about the next 25 years at the going consumption rate as well as vast amounts of undiscovered as well as unconventional resources. NG also has an existing well-developed infrastructure throughout North America. Hydrogen fuel will be linked to that of NG for the near future. Most hydrogen will be produced by steam methane reforming and will require the NG feedstock. The local availability of these fuels makes them very attractive alternatives.

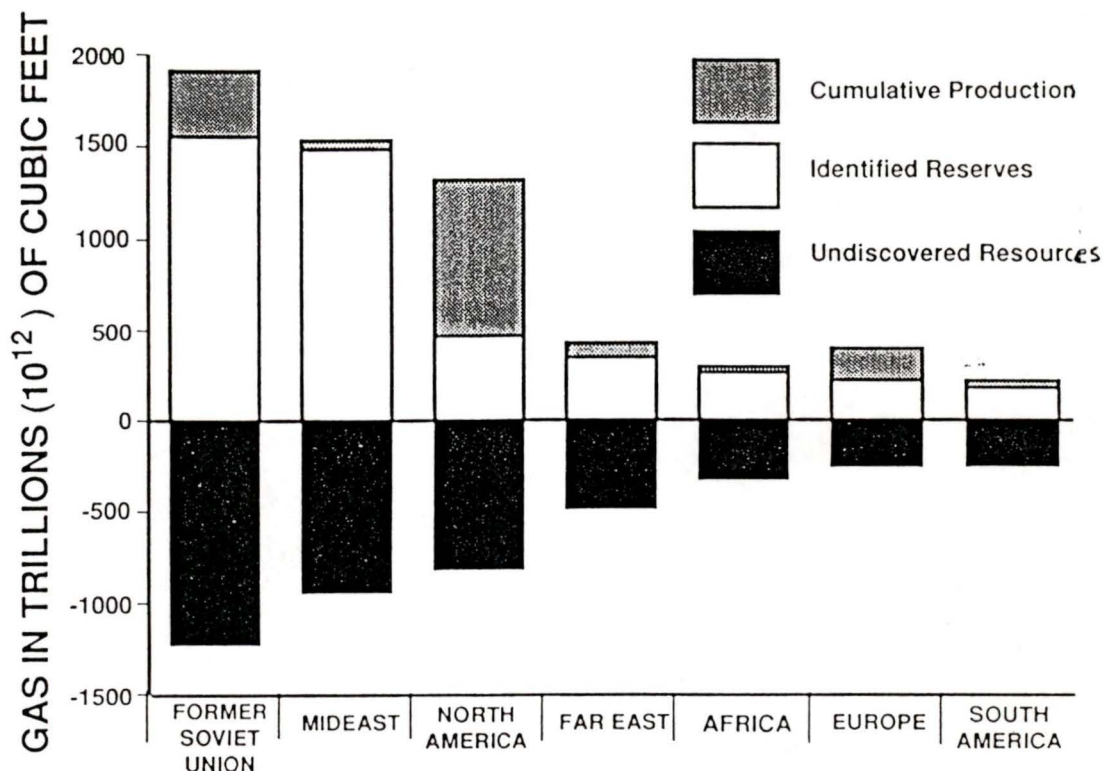


Figure 1.1a: Geographic distribution of identified reserves and cumulative production of natural gas as of January 1990, and undiscovered resources as of January 1991 [3].

- Environmental factor - Low or zero carbon content fuels provide an attractive solution to the urban pollution problems caused primarily by gasoline and diesel fuelled vehicles. Also, the contribution of greenhouse gases from the transportation sector can be slowed or even stopped by adoption of these alternative fuels. Urban pollution is a mixture of several pollutants where particulates, non-methane gases, carbon monoxide, and nitric oxide (NO_x) are the major contributors. Recently, the U.S. has begun to legislate the use of lower polluting alternative fuels. The California Air Resources Board (CARB) has set standards for tailpipe emissions and has

had legislation passed that mandates conversion of vehicles that meet the progressively more stringent standards. The Environmental Protection Agency has recently recommended that the CARB legislation be adopted by all other states as a standard urban pollution abatement policy [4]. Table 1.1a shows the CARB emission standards for light duty vehicles [5].

Table 1.1a: CARB emission standards for light-duty vehicles; NMOG = non-methane organic gases; NMHC = non-methane hydrocarbons; TLEV = transitional low emission vehicle; LEV = low emission vehicle; ULEV = ultra low emission vehicle.

Pollutant	Grams per Mile		
	TLEV	LEV	ULEV
NMOG	0.125	0.075	0.04
CO	3.4	3.4	1.7
NO _x	0.4	0.2	0.2
Formaldehyde	0.015	0.015	0.008

Table 1.1b shows the mandated conversion schedule for light-duty vehicles specified by CARB [6].

Table 1.1b: CARB minimum phase-in schedule (up to year 2000) for light-duty vehicles; ZEV = zero emission vehicle.

Model Year	TLEV	LEV	ULEV	ZEV
1994	10%			
1995	15%			
1996	20%			
1997		25%	2%	
1998		48%	2%	2%
1999		73%	2%	2%
2000		96%	2%	2%

Canadian cities are facing a similar problem with urban pollution and CARB style legislation is beginning to be seriously considered [7]. Natural gas, when burned in dedicated engines, can easily meet the ULEV emission standards [8]. Hydrogen will also meet ULEV standards and, when used in a fuel cell, will meet ZEV criteria. The environmental attractor is a function of public mood and perception and, consequently, cannot be considered a long term driver to alternate fuels.

- **Economics** - While foreign oil concerns and environmental factors are attractors to the use of low and no carbon based fuels, economics is presently the major barrier. Alternative fuels simply will not penetrate the transportation market if their use is ultimately uneconomical. IESVic members recognize this and have identified cost effective refuelling infrastructure as the technical barrier to the increased use of alternate fuels. CFS has set its primary goal to design and manufacture refuelling stations that will make the use of natural gas competitive with conventional fuels on a cost basis. CFS is focusing on natural gas as a pathway to hydrogen. NG is the current alternative fuel of choice because it can be cheaply supplied, it has excellent fuel characteristics, and a well developed infrastructure exists. Because the feedstock price of NG is, on average, about 70 to 80% of conventional transportation fuels, the task of making the fuel economical is to reduce the capital and operating expenses of the refuelling system. CFS is building a magnetic NG liquefier that will be a core component of this refuelling system. By producing liquefied natural gas (LNG), compressed natural gas (CNG) can also be offered by using a cryogenic liquid pump. This means that a single station will be able to deliver LNG for medium to heavy duty applications and CNG for light-duty applications or for vehicles where range and weight are not so critical. Magnetic liquefaction has the advantage of potentially high operating

efficiencies. This will help reduce operating costs. The capital cost of the system will initially be high, but with subsequent research and increased demand, it is hoped that this will be lowered to the point where the NG economics will be improved by introducing magnetic liquefiers into refuelling systems.

CFS is currently funded by NSERC and Centra Gas and has a five year mandate to build an active magnetic regenerative refrigerator (AMRR) to efficiently liquefy NG. CFS will demonstrate the technology by liquefying natural gas that has a boiling point of 110 K @ 0.1 MPa (hydrogen boils at 20 K at this pressure).

1.2 Thesis Objectives

1.2.1 Overall AMRR Project

The research and development of the world's first AMRR to liquefy natural gas is a large undertaking. Consequently, the project has been divided into several parts, each being researched by different investigators. These parts include:

- magnetic working materials and regenerator fabrication;
- superconducting magnet subsystem;
- regenerator test apparatus;
- computer simulation design aid, and
- overall system integration.

The research efforts are coordinated in a parallel fashion to produce a 700 Watt AMRR prototype that will span the temperature range of 240-110 K. A conventional gas cycle refrigerator will be used as an upper stage to bridge the 240 K to ambient temperature span.

1.2.2 Thesis Focus

The objective of this thesis is to develop and manufacture highly effective active magnetic regenerators for an AMRR used to liquefy natural gas. A great deal of research is required to achieve this objective. In particular, the required work can be divided into:

- selection of magnetic materials for the AMRR;
- preparation of selected magnetic materials;
- characterization of selected magnetic materials;
- manufacture of high performance active magnetic regenerators from selected magnetic materials, and
- testing of fabricated regenerators.

This thesis has been written to reflect the above divisions and to detail the work completed in each. The work presented here will be considered independently of the parallel research efforts that are occurring in the overall project.

1.3 Theory Behind Active Magnetic Regenerative Refrigerators (AMRR)

1.3.1 General Concept

Magnetic refrigerators employ the magnetocaloric effect (MCE) of ferromagnetic materials to achieve cooling. The MCE is a phenomenon that takes place when certain magnetic materials are subjected to magnetic fields. The MCE occurs when a magnetic solid heats up when adiabatically magnetized, and cools down again when adiabatically demagnetized (see section 1.3.4 for further details on the MCE). During a simple magnetic refrigeration cycle, magnetized material is periodically put in contact with a

high temperature sink and demagnetized material is put in contact with a low temperature source. These steps are linked by magnetization and demagnetization processes. This description is generic and could be based on several thermodynamic cycles (Carnot, Brayton, Stirling, etc.) The cycle is analogous to that of a gas refrigerator where the compression and expansion processes are replaced by the magnetization and demagnetization processes (see Figure 1.3.1a). Many rare earth elements have large magnetic moments and therefore may exhibit large MCEs at or near their Curie or ordering temperatures. This feature makes them excellent candidates for the working materials in magnetic refrigerators.

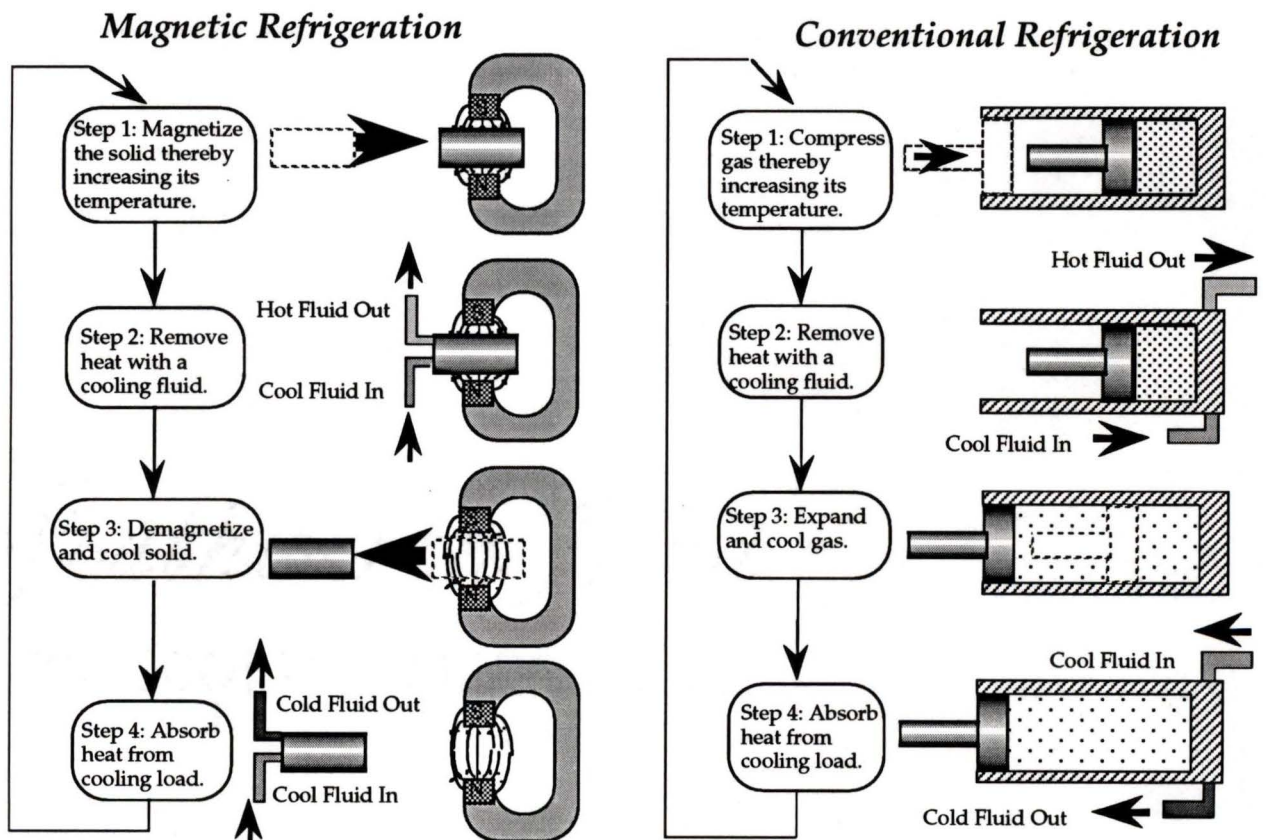


Figure 1.3.1a: Magnetic Cycle processes (with gas cycle analogues).

1.3.2 Active Magnetic Regenerators

The temperature span of a simple magnetic refrigeration cycle is constrained by the magnitude of the magnetocaloric effect of the material used. To extend this temperature span, the addition of a regenerative heat exchanger and a circulating heat transport medium is necessary. The refrigerator design being developed at Cryofuel Systems uses an active magnetic regenerative device to span the temperature range of 110 K to 240 K [9]. In this arrangement, the thermodynamic work and regeneration are accomplished by using several suitable ferromagnetic materials that function as both the thermal storage and as the working material in the refrigeration cycle. These materials are formed into highly effective regenerative geometries (such as fine particles or wire meshes) with porosities ranging from 40 to 80%. The thermodynamic work is accomplished by each infinitesimal element of magnetic material in the AMRR undergoing a magnetic cycle as the regenerative magnetic material is cycled in and out of the magnetic field. These elements are linked by the convective heat transport fluid. During the magnetization half of the cycle, the material deposits both stored heat and work-generated heat into the fluid where it is subsequently rejected to the environment at the hot-end heat exchanger. When the magnetic regenerator cycles out of the field, the fluid deposits heat into the material and can, in turn, pick up the refrigeration load at the cold end heat exchanger. Figure 1.3.2a shows the fluid and material temperature profiles for an AMRR during the cycle operation. The symbol ϕ in Figure 1.3.2a is a representation of the thermal energy change that the fluid removes from and deposits to the material as it flows through it (fluid washing effects). At the beginning of the blow (profile (ii)), the fluid enters at T_c . By the end of the blow (profile (iii)), the fluid has washed enough energy from the solid to reduce the solid temperature profile.

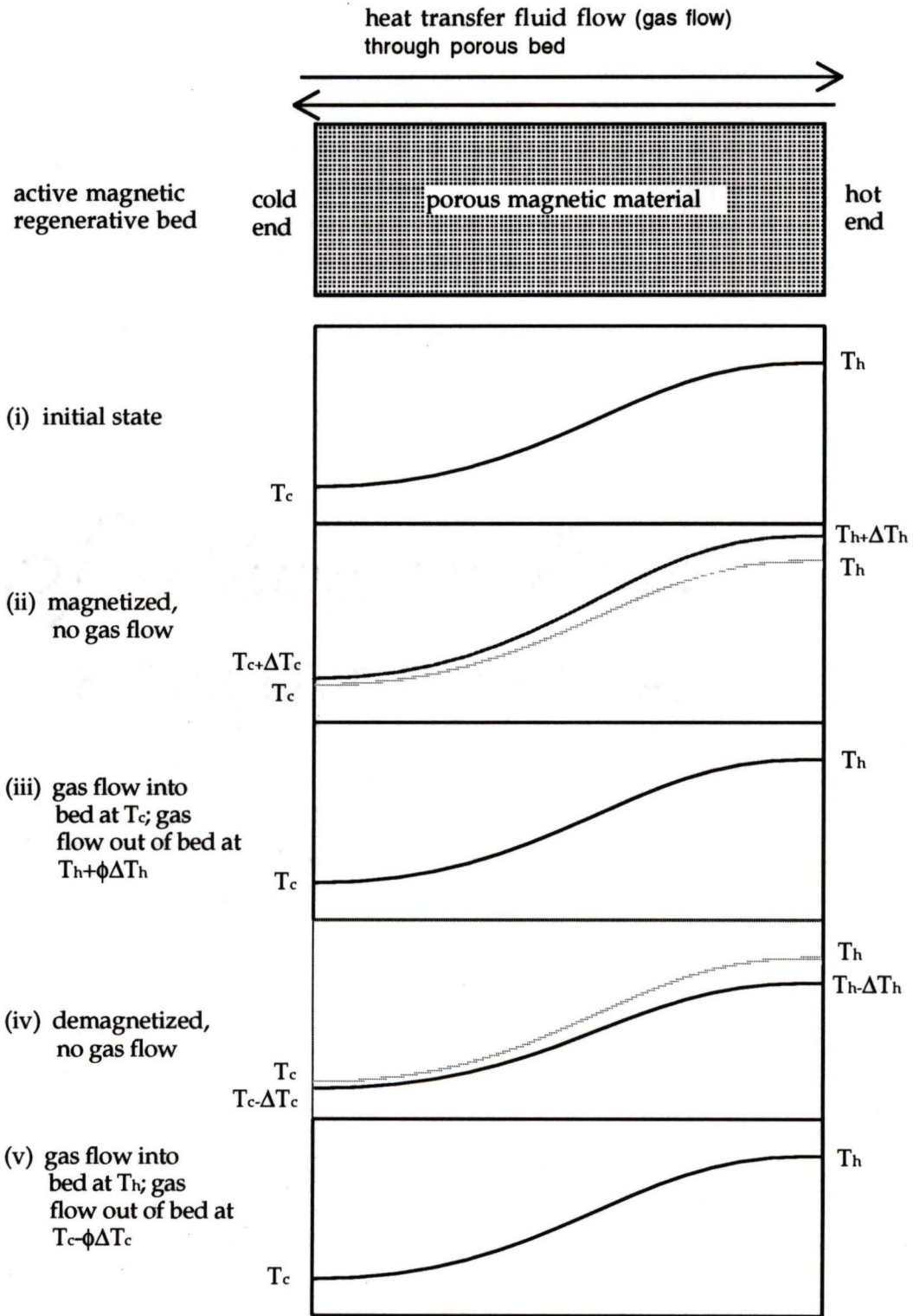


Figure 1.3.2a: Material temperature profiles for AMRR. Soft lines indicate initial state and ϕ is some value between 1 and 0 [10].

The value of ϕ represents the average temperature of the fluid exiting the regenerator during the blow. In the case depicted in Figure 1.3.2a, ϕ is equal to 0.5 because the material recovers its initial state after the gas flows in (iii) and (v). The material profiles are depicted this way for clarity only. The value of ϕ will be a direct function of the ratio of the material and heat transfer fluid's thermal mass.

The magnetic work done by each piece of magnetic material during the cycle is a function of the magnitude of the adiabatic temperature change and the material thermal energy change (washing) caused by the heat transfer fluid. Because of this, the correct selection and arrangement of the materials used in the AMRR is crucial to achieving high efficiencies in the cycle [11] [12] [13]. Before real materials are chosen, it is necessary to perform an analysis of the thermodynamic requirements of the AMRR system to determine the material selection criteria for an ideal material. Once these criteria are established and pertinent material properties are considered, real material(s) can be selected and arranged in the regenerator.

1.3.3 Prototype System Configuration and Operation

The AMRR design configuration chosen by the Cryofuel Systems Group is a wheel-shaped rotary device schematically shown in Figure 1.3.3a. In this prototype device, the wheel is made of suitable magnetic materials and serves as the active magnetic regenerator. Helium is the heat exchange fluid that picks up a heat and entropy load at the cold end and rejects it at the hot end by being circulated through the magnetized and demagnetized active magnetic regenerator media. The high magnetic region will be created by a superconducting magnet configuration that will cover about 120° of the wheel.

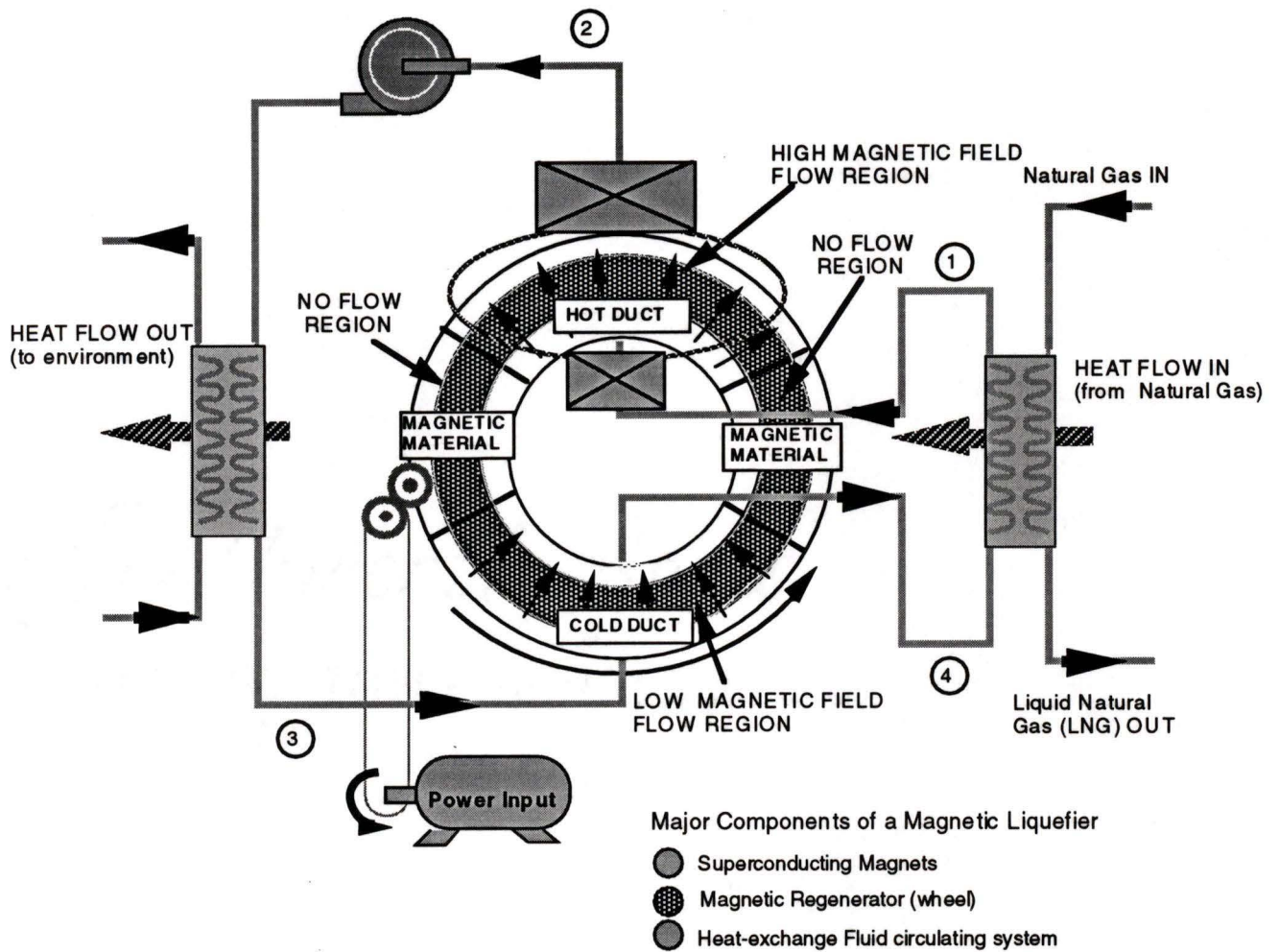


Figure 1.3.3a: Wheel-shaped rotary AMRR prototype design.

The magnetic fields generated will average about 6 Tesla over the high field flow region. Other specifications for this prototype include [14]:

- cooling power (\dot{Q}_c) = 700 W
- cold source temperature = 110 K
- hot end rejection temperature = 240 K

- helium flow rate = 0.096 kg/s
- magnetic refrigerant mass flow rate = 125 kg/s
- helium pressure = 5 MPa
- regenerator matrix = 100×10^{-6} m diameter particles
- operating frequency = 5 Hz

The overall operation of the rotary AMRR device can be understood by following the heat exchange fluid (or gas) as it completes one cycle. The following description uses the state points listed in Figure 1.3.3a and the magnetic regenerator information provided in Figure 1.3.2a:

- state 1: The gas (helium in this case) has just passed through the cold end load heat exchanger and is at T_c . At this point the regenerator material temperature profile is like profile (i) in Figure 1.3.2a. Before the gas passes through the magnetic regenerator, the regenerator bed is magnetized and heats up to resemble profile (ii) in Figure 1.3.2a.
- state 2: The helium has passed through the magnetized regenerator and is at a temperature greater than the environment ($T_h + \phi \Delta T_h$).
- state 3: The helium has passed through the hot end environment heat exchanger and is now at T_h . The regenerator has rotated out of the high field region, is demagnetized and has a temperature gradient like profile (iv) in Figure 1.3.2a.
- state 4: The heat transfer fluid has passed through the demagnetized regenerator and is at $T_c - \phi \Delta T_c$. The helium is now ready to pick up the natural gas cooling load and repeat the overall cycle. At this point, the material has recovered its initial state (profile (v), Figure 1.3.2a).

It is unlikely that a single magnetic material will have all of the required characteristics that the AMRR requires to meet the operating specifications. The regenerative wheel will be divided into radial compartments to

accommodate the selected magnetic material and to provide layering of different magnetic refrigerants as well as axial compartments to avoid azimuthal flow. Several materials will need to be physically layered radially adjacent to each other. Figure 1.3.3b shows the details of the regenerator component of the AMRR prototype.

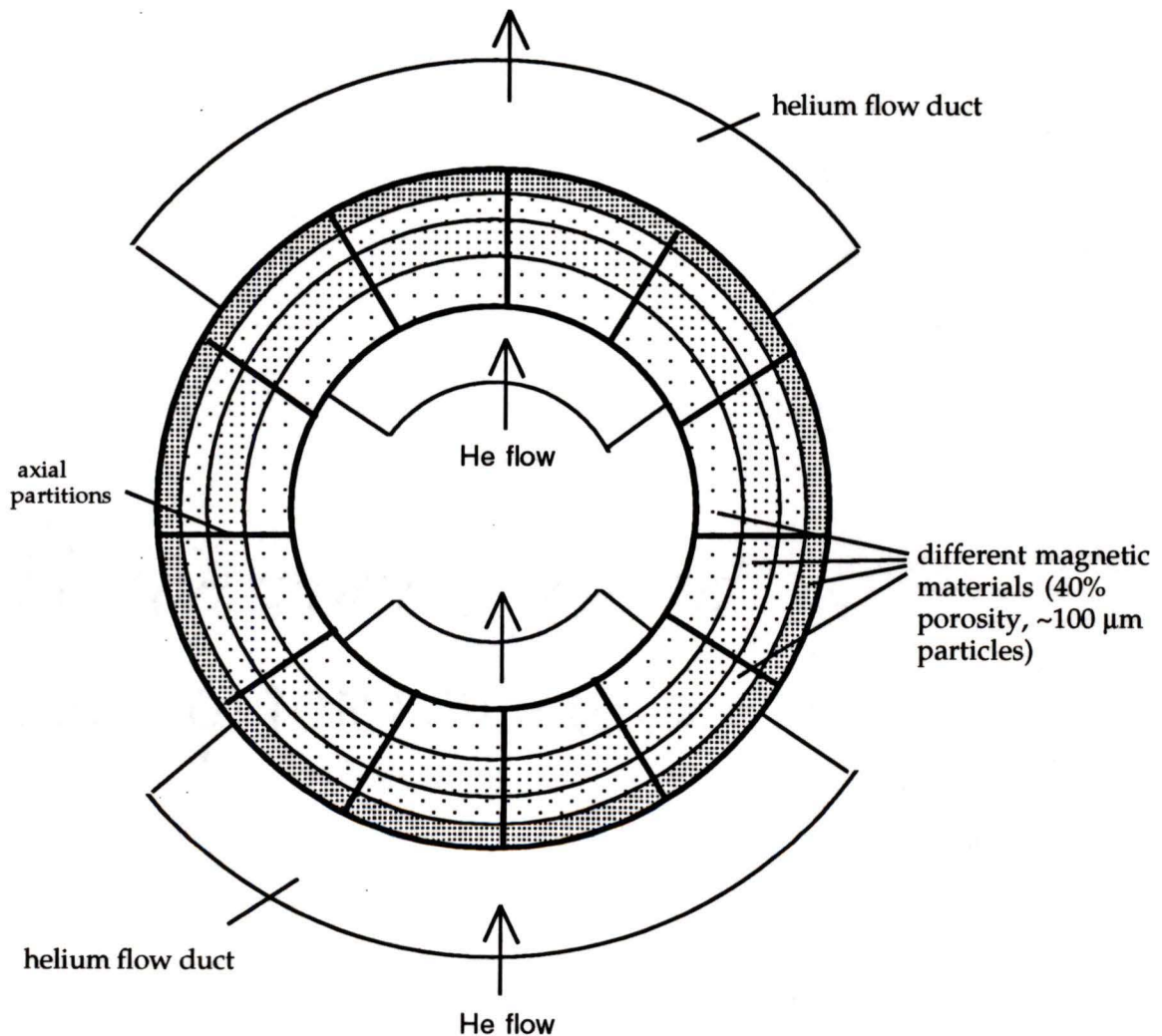


Figure 1.3.3b: Details of regenerator compartments in the rotary AMRR prototype.

1.3.4 The Magnetocaloric Effect

The magnetocaloric effect (MCE) is the basis for all magnetic refrigeration systems. When a magnetic field is applied to a simple ferromagnet, the exchange coupled magnetic dipole moments align with the applied field. This causes a transfer of entropy from the magnetic system to the phonons in the materials's crystal lattice. Under adiabatic conditions the requirements of constant system entropy results in a temperature increase of the bulk material. In ferromagnetic systems, the material is most susceptible to an applied field at the absolute temperature where the material begins to spontaneously order its magnetic dipoles, a transition point known as the Curie Temperature. At the Curie temperature, the energy of the magnetic moments begin to dominate the lattice thermal energy. Accordingly, the amount of applied magnetic field to change the system entropy is less at this point. Figure 1.3.4a shows the dipole magnetization process for a simple ferromagnet.

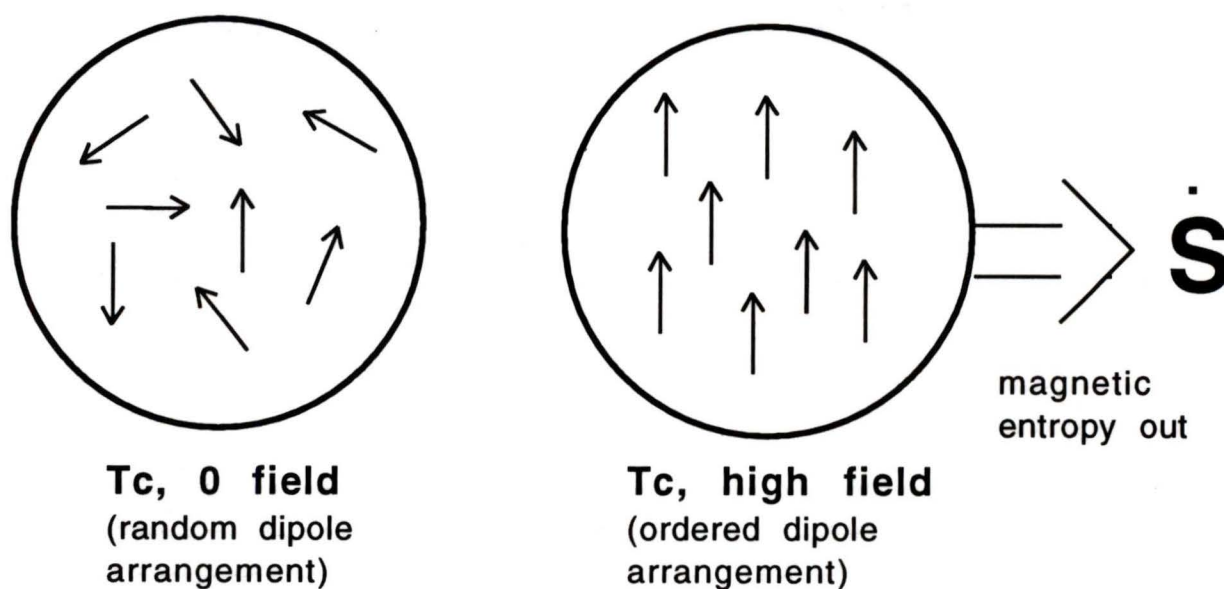


Figure 1.3.4a: Dipole magnetization of a simple ferromagnet.

The MCE of a given material can be evaluated in several ways. It can be measured directly, or calculated given the material's magnetization and specific heat data as a function of temperature and applied magnetic field. The MCE or adiabatic temperature change is calculated by [15]:

$$\Delta T_{\text{ad}} = \mu_0 \int_{H_1}^{H_2} \left[\frac{T}{C_H} \left(\frac{\delta m}{\delta T} \right)_H \right] dH. \quad (1.1)$$

Appendix A shows how the adiabatic temperature change of a material can be evaluated using several different approaches.

1.3.4.1 The Lanthanide Series

The Lanthanide series of elements in the periodic table (elements 57-70, sometimes including Yttrium, see Figure 1.3.4.1a) are commonly referred to as the rare earth materials. These elements and alloys/compounds thereof are of great importance as magnetic refrigerants because of their large magnetic moments. The lanthanides are grouped together because of their common electronic structure. The 5s, 5p, and 6s orbitals are filled, while the 4f orbital varies from 2 to 14 electrons with increasing atomic number. This leads to these materials displaying some of the largest MCEs of all magnetic materials. In this thesis, all magnetic materials considered were crystalline rare earth elements, alloys or compounds because of their good formability characteristics.

1 H 1.008																	2 He 4.003	
3 Li 6.941	4 Be 9.012											5 B 10.81	6 C 12.01	7 N 14.01	8 O 16.00	9 F 19.00	10 Ne 20.18	
11 Na 22.99	12 Mg 24.31											13 Al 26.98	14 Si 28.09	15 P 30.97	16 S 32.06	17 Cl 35.45	18 Ar 39.95	
19 K 39.10	20 Ca 40.08	21 Sc 44.96	22 Ti 47.90	23 V 50.94	24 Cr 52.00	25 Mn 54.94	26 Fe 55.85	27 Co 58.93	28 Ni 58.70	29 Cu 63.55	30 Zn 65.38	31 Ga 69.72	32 Ge 72.59	33 As 74.92	34 Se 78.96	35 Br 79.90	36 Kr 39.95	
37 Rb 85.47	38 Sr 87.62	39 Y 88.91	40 Zr 91.22	41 Nb 92.91	42 Mo 95.94	43 Tc (98)	44 Ru 101.1	45 Rh 102.9	46 Pd 106.4	47 Ag 107.9	48 Cd 112.4	49 In 114.8	50 Sn 118.7	51 Sb 121.8	52 Te 127.6	53 I 126.9	54 Xe 131.3	
55 Cs 132.9	56 Ba 137.3	<i>Lanthanide Series</i>											81 Tl 204.4	82 Pb 207.2	83 Bi 209.0	84 Po (209)	85 At (210)	86 Rn (222)
87 Fr (223)	88 Ra (226)	20	57 La 138.9	58 Ce 140.1	59 Pr 140.9	60 Nd 144.2	61 Pm (145)	62 Sm 150.4	63 Eu 152.0	64 Gd 157.3	65 Tb 158.9	66 Dy 162.5	67 Ho 164.9	68 Er 167.3	69 Tm 168.9	70 Yb 173.0		
		89 Ac (227)	Th 232.0	Pa (231)	U 238.0	Np (237)	Pu (244)	Am (243)	Cm (247)	Cf (251)	Bk (247)	Es (252)	Fm (257)	Md (258)	No (259)			

Figure 1.3.4.1a: Lanthanide (rare earth) elements.

1.3.4.2 ΔT_{ad} vs T Curves for the Lanthanides

The MCE or adiabatic temperature changes of materials can be best represented by an adiabatic temperature change vs absolute temperature (ΔT_{ad} vs T) curve. Figure 1.3.4.2a shows the ΔT_{ad} vs T curve for several elemental heavy rare earth materials under an applied magnetic field of 6 Tesla. Gadolinium is close to a simple ferromagnet and its curve assumes a caret-shaped profile because of the well defined transition or Curie temperature where the magnetic phase changes from paramagnetic to ferromagnetic. In several cases, a material's magnetic phase transition is not so simple. For rare earths materials other than gadolinium, the transition is often marked by additional magnetic phases that produce markedly different ΔT_{ad} vs T profiles as can be seen in Figure 1.3.4.2a (discussed further in section 4.2.1).

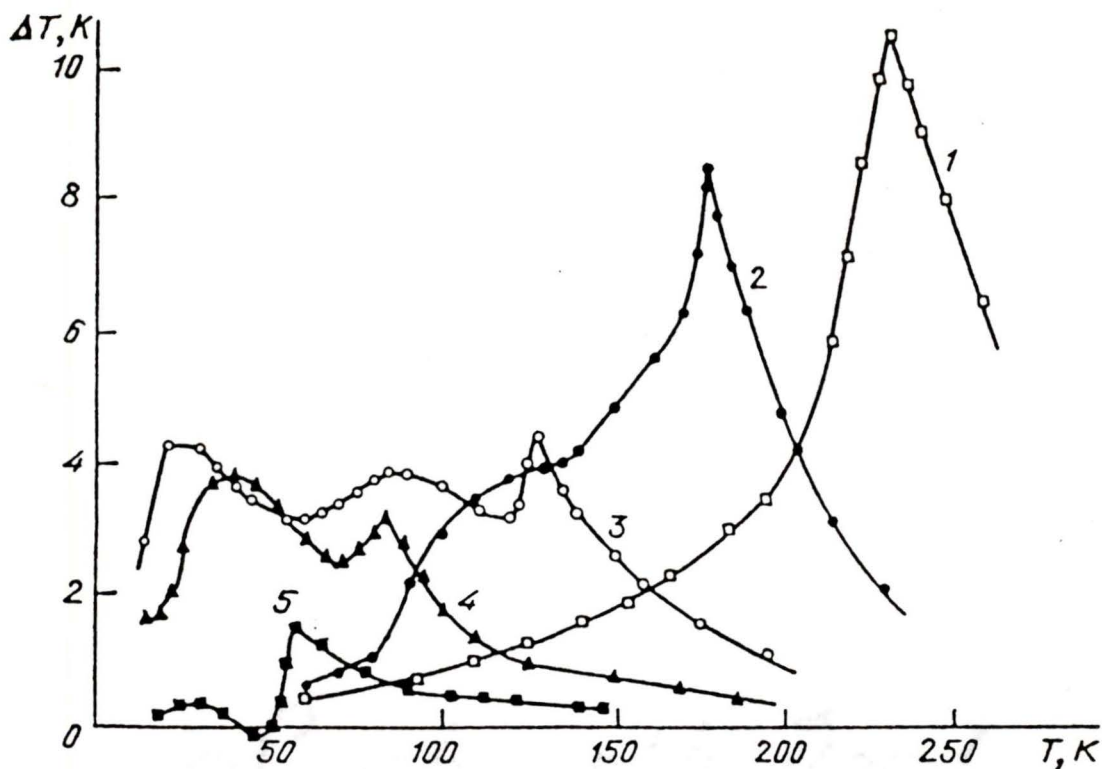


Figure 1.3.4.2a: ΔT_{ad} vs T Curves for (1) Tb, (2) Dy, (3) Ho, (4) Er and (5) Tm in a field $H=60.2$ kOe [16].

1.4 Relevant Prior Work

There has been much prior work into several topics that embody this thesis. The relevant prior work has generally been broken down into the distinct research areas defined above. All new work in these areas presented in this thesis will be highlighted and emphasized.

1.4.1 Selection of Magnetic Materials for the AMRR

There has been considerable research done on the selection of magnetic materials for magnetic refrigeration applications. A large amount of this

work has recently been done by Russian researchers. Kuz'min and Tishin have discussed the refrigerant capacity of several of the heavy rare earth materials and their alloys [17]. Nikitin et al. evaluate the material refrigeration performance by the product of the magnetic entropy change of the material and the regenerator temperature span $((T_h - T_c) \cdot \Delta s_m)$ [18]. The magnitude of this product is referred to as the refrigeration capacity of the material and in the temperature range of interest the Russians use it as the material selection criteria.

Japanese researchers led by Hashimoto et al. have worked extensively on passive magnetic regenerators for low temperature cryocoolers using Carnot cycle paramagnetic refrigerants in the 1 K to 20 K range as well as ordered magnetic materials for active magnetic refrigeration for higher temperatures [19] [20]. They indicate that the characteristic utilized for good AMR materials is the magnetic specific heat and the magnetic entropy change (taken together, this is the equivalent of the MCE). Hashimoto suggests that the guideline for selecting materials should be the population of spins and the total angular momentum (J). If they are large, the material should be promising. Like the Russians, the Japanese employ the conventional wisdom of maximizing the material's available magnetic entropy.

Gschneidner et al. from Ames Labs have also begun extensive work into the development of AMRR magnetic materials [21]. The material selection criteria they use is also to maximize the magnetic entropy and MCE. However, they also recognize the importance of the distribution of the magnetic entropy and the influence of other magnetic phases, the magnetic hysteresis and hardness, and the chemical stability of the material.

Barclay, Cross and Degregoria et al. developed the material selection criteria

one step further by considering the magnetic material in an actual AMRR device and by developing optimal temperature-entropy curves [22]. Their conclusion was that the $\Delta T_{ad,c}$ of the material was proportional to the $\Delta T_{ad,h}$ of the material by the ratio of the absolute end temperatures (T_c/T_h) or the Carnot scaling factor. This criteria was applied throughout the regenerator bed based on the assumption of constant entropy flux from the cold to the hot end. This led to linear ΔT vs T profiles for the ideal material. With these criteria, Schuricht and Zimm examined the effects of using more than one magnetic material layered in a regenerator bed to increase the effective temperature span of the device [23] [24]. Other researchers such as Carpetis, Green et al., and Smith et al. have modelled, designed, and built AMRR devices but basically accept the material selection criteria based on the Curie point and magnetic entropy available [25] [26] [27].

Recently, Reid et al. discussed selection criteria of magnetic materials for AMRRs where the material selection process is more closely linked with the device that the material will operate in [28]. The linear material profile and the Carnot scaling of the required cold end heat exchanger temperature change (based on a given cooling power) are again the basic selection criteria as outlined by Barclay et al. However, real effects of the regenerator and the relation to the convective heat transfer fluid are added to the material profile. The ideal material must be able to pump out the additional entropy generated in the regenerator. Reid et. al also review the effects of mixing materials to generate the ideal magnetic material regenerator ΔT_{ad} vs T profile. The work presented in this thesis generates new theory on the operation of the AMRR and the implications for refrigerant material selection. Although all previous work on maximum magnetic entropy and MCE remain valid, these criteria need to be coupled to the operating properties of the refrigerating device that the material will be operating in. Some prior work attempts to do this, but

the assumptions of work, entropy and heat fluxes have been re-evaluated, and a new theoretical model for the AMRR is put forth.

1.4.2 Preparation of Rare Earth Magnetic Materials

Few papers have been published on the preparation of rare earth materials for characterization processes such as photomicroscopy and scanning electron microscopy. Preparation processes include cutting, mounting, grinding, polishing, and etching. R. Asomoza et al. and Buehler Labs have published some data and methods [29] [30]. All materials discussed in this thesis were prepared in part by reference to prior literature and by empirical experimentation.

1.4.3 Characterization of Rare Earth Magnetic materials

Characterization data for the rare earth materials are scattered among several publications and research papers. Much of the magnetic entropy and MCE data was compiled from Russian research on the MCE properties and magnetic phase structures of heavy rare earth materials and intra-rare earth alloys [31] [32] [33]. More magnetic phase structure and transition point temperature data was collected from Landolt and Boernstein [34]. Physical, mechanical, elastic, and transport properties appear in several different sources with the bulk being published in 'The Handbook on the Physics and Chemistry of Rare Earths' [35].

This thesis compiles a large amount of the scattered characterization data for the heavy rare earth materials. New work in this area presented here include estimations of Curie points and MCEs of potential magnetic refrigerants as well as data on the bulk resistivity of rare earth particle beds.

1.4.4 Analysis of High Performance Regenerators

For the purpose of this review, regenerators have been classified as either passive or active. Passive regenerators act primarily as thermal storage devices whose function is to regenerate a heat transfer fluid. Active regenerators perform all of the functions of the passive regenerators but the regenerative material also functions as the working refrigerant in the cycle.

1.4.4.1 Passive Regenerator Analysis

Passive regenerator design and analysis papers reviewed date back several decades to the classic works of Schumann, and Hausen [36] [37]. In the late forties, Tong and London reported on the heat transfer and flow friction of screen and crossed-rod matrix regenerators [38]. Coppage and London published a summary of design theory for the periodic flow regenerator and Smith et al. discussed aspects for regenerator selection [39] [40]. These works (as well as others) are summarized in the publication of Kays and London's 'Compact Heat Exchangers' [41]. This work analyses regenerators based on friction factors and Colburn J factors (heat transfer coefficients) as a function of Reynold's number. Several heat exchanger configurations are reviewed and the periodic flow regenerator geometries covered are wire screens (using crossed rods) and packed particle beds. Other papers have been published that discuss the performance of both screens and particles as well as perforated plates, spiral wound (parallel plate) geometries, and others [42] [43] [44] [45]. Most prior work deals with the heat transfer and flow friction only when analyzing regenerators or porous media. Some studies have considered longitudinal conduction effects and try to establish correlations for total conduction including eddy diffusivity, fluid, and solid effects [46]. Schmidt and Wilmott discuss several thermal energy models for regenerators

including equations for transient models [47]. Their analysis covers single blow problems, counterflow regenerators, heat storage exchangers, and packed particle beds.

1.4.4.2 Active Regenerator Analysis

There is not much prior work on active regenerator design and analysis. Barclay published an early work describing some mathematical theory in 1983 [48]. The key paper reviewed was a paper on the selection of regenerator geometry for magnetic refrigerator applications published by Barclay and Sarangi [49]. In this analysis, the regenerator performance is calculated by a 2nd law thermodynamic analysis in which the heat transfer, pressure drop, and longitudinal conduction losses are calculated as entropy productions. This leads to a Figure of merit (FOM) efficiency for the regenerator that is a convenient way of expressing multi-parameter optimum design. Four different regenerator geometries were analyzed under different conditions and FOMs were established as aspect ratios and operating frequencies are changed.

This thesis builds on the Sarangi method by including both passive and active design parameters that need to be considered when evaluating high performance AMRRs. Extra losses or entropy production come from eddy currents, finite thermal mass of the regenerative material, and the effect of porosity or fluid entrainment as the material is cycled in and out of high magnetic field regions.

1.4.5 Manufacture of Regenerators From Rare Earth Magnetic Materials

1.4.5.1 Passive Regenerator Manufacture

For two decades, researchers have developed high heat capacity intermetallic rare earth compounds to use as passive regenerators in low temperature cryogenic machines (i.e. Gifford-McMahon refrigerators). Several rare earth intermetallic compounds (in particular Er_3Ni) provide higher heat capacities than the lead that was conventionally used. This feature allowed the materials to retain their regenerative capacity for He gas at colder temperatures [50] [51] [52] [53].

Rare earth intermetallic compounds are extremely brittle and difficult to manufacture into useful regenerator geometries. Small particles tend to fracture and crush during operation creating fine dust. Several atomization techniques have been used to create spherical regenerator particles out of the intermetallics to increase the fracture toughness of the materials. Toshiba and Sumitomo Precision Products produce and sell Er_3Ni particles using a rotating disk centrifugal atomization method. Anderson et al. have been developing centrifugal atomization techniques for rare earth intermetallics over the last few years [54] [55] [56]. Ludeman and Zimm at the Astronautic Corporation of America developed a low velocity drop tower production process and obtained good passive regenerator results with GdNi_2 [57].

1.4.5.2 Active Regenerator Manufacture

Rare earth intermetallic compounds can also be used in active regenerators. Recall that a magnetic material has its largest entropy changes around its Curie or transition point. Therefore, different materials can be more effective

refrigerants at different temperatures. Researchers have used GdNi_2 and GdPd as well as others in the 20 K to 80 K region [58]. The fabrication problems are consistent with those outlined above and most active regenerative media has been made into packed particles. Much less work has been done in regenerator fabrication for operation in the 100 K to 300 K region. In this temperature region, rare earth elements and intra rare earth alloys can be used as magnetic refrigerants. The ductility of these alloys is much greater than intermetallic compounds and allows for more flexibility when manufacturing high performance geometries. Green et al developed a Gd-Tb active regenerator made from a spirally wound rare earth sheet [59]. They used embossed bumps on the ribbon as spacers to create parallel plate flow spaces on a micro scale.

In this thesis, heavy rare earth elements and alloys are fabricated into fine spherical particles and fine wires for screen manufacture. These materials of commercial grade purity have seldom been cost-effectively fabricated into such geometries before. Production methods were adapted/developed to produce low-cost, high quality regenerator media products.

Chapter 2

Selection of Magnetic Materials for the AMRR

To correctly select magnetic materials (working materials or refrigerants) for the AMRR, the thermodynamic requirements must first be evaluated and material selection criteria established. Real materials must then be compared to the selection criteria and all important properties evaluated before the final choices can be made.

2.1 Thermodynamic Requirements

2.1.1 Detailed AMRR Operation

Active magnetic regenerator refrigerators operate under a unique thermodynamic system because of the interaction of two distinct subsystems. These two subsystems are: (1) the regenerative magnetic working materials, and (2) the circulating heat transfer fluid. Fundamentally, when an AMRR operates, these subsystems are linked as follows (see Figure 2.1.1a):

(i) The applied magnetic field does work on the magnetic regenerative material bed generating heat energy; this 'active' heat is then transferred to

the circulating heat transfer fluid (helium) as it physically passes around the working material; at the same time, because the magnetic material is also operating as a regenerator, it is transferring additional 'passive' heat energy to the helium.

(ii) At the hot end of the device, the helium passes through a heat exchanger and rejects heat energy to the environment.

(iii) The helium then re-enters the demagnetized magnetic regenerator bed. The demagnetized material readily absorbs both passive and active heat energy from the helium and cools the gas down so that it can absorb a heat load from the cold source.

(iv) The gas passes through the cooling load exchanger, absorbs the heat from the source and the complete system is ready to repeat the overall cycle.

In a gas compression and expansion regenerative refrigerator, the working material and the heat transfer fluid are the same. In the AMRR, the working material and the heat transfer fluid are separate. This means that the AMRR must undergo an additional process where the magnetic working material transmits the work-generated heat (active heat) to the helium, and the helium consequently communicates with the heat source and sink. This is the basis of the linked subsystems that are characteristic of an AMRR. Each of the AMRR thermodynamic subsystems can be represented on T-s cycle diagrams. The T-s diagram for the helium as it cycles through the refrigerator actually imparts little useful data as it functions only as the heat transfer link between the working/regenerative solid and the heat source/sink.

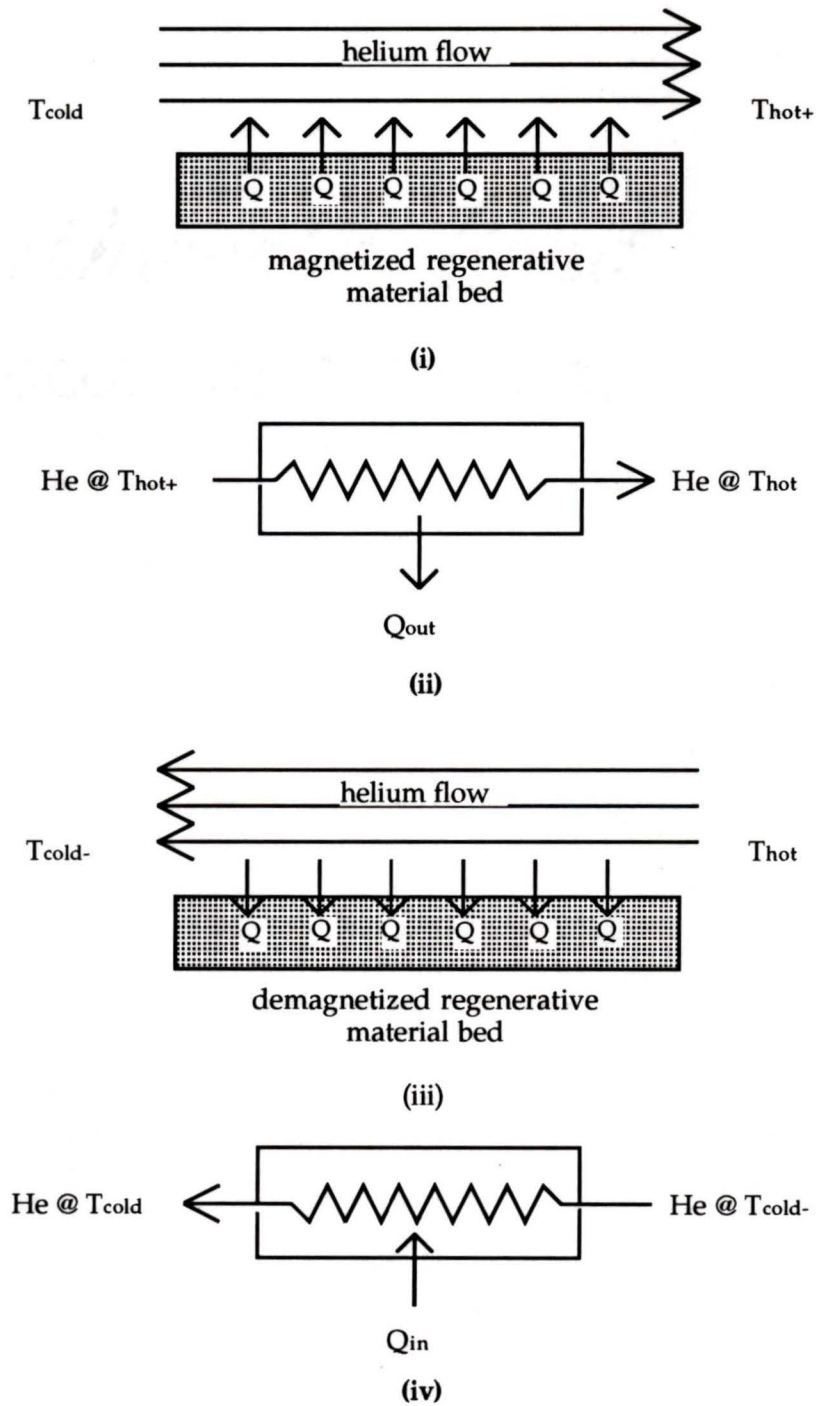


Figure 2.1.1a: Heat flow among the AMRR thermodynamic subsystems.

In the limit of zero pressure drop throughout the helium cycle, the T-s diagram would look like a single positively sloped line segment as the fluid was heated and cooled. The magnetic material, on the other hand, does net magnetic work and undergoes a definite thermodynamic cycle. As the entire AMR bed is cycled in and out of a high magnetic field, each infinitesimal element along the regenerator bed is at a different temperature. This causes each element to undergo a distinct magnetic cycle because the degree of work done will be a function of the absolute temperature of the material segment and its magnetic entropy changes. In the magnetic regenerative bed discussed above, the total work done by the material (and active heat transferred to the helium) is the sum of the work done by each individual, microscopic piece of material along the regenerator bed. This is the total thermodynamic work input for the complete AMRR system.

The most efficient regenerative thermodynamic cycle that the material segments in the AMRR can undergo is a magnetic Ericsson cycle which consists of two isothermal magnetization and demagnetization processes and two isofield heat transfer processes. Under ideal conditions, this cycle will achieve Carnot efficiency. Figure 2.1.1b shows the T-s diagram for a single magnetic material element undergoing a magnetic Ericsson cycle while operating in an AMRR (with active and passive heat flows). During process 1-2, the material is magnetized and isothermally transfers active heat to the helium (not to the next magnetic element). Process 2-3 shows the passive heat transfer as the material is cooled by the helium. The material is demagnetized during process 3-4 and adsorbs active heat back from the helium. Finally, process 4-1 shows the other half of the the passive heat transfer as the helium regenerates (warms) the material.

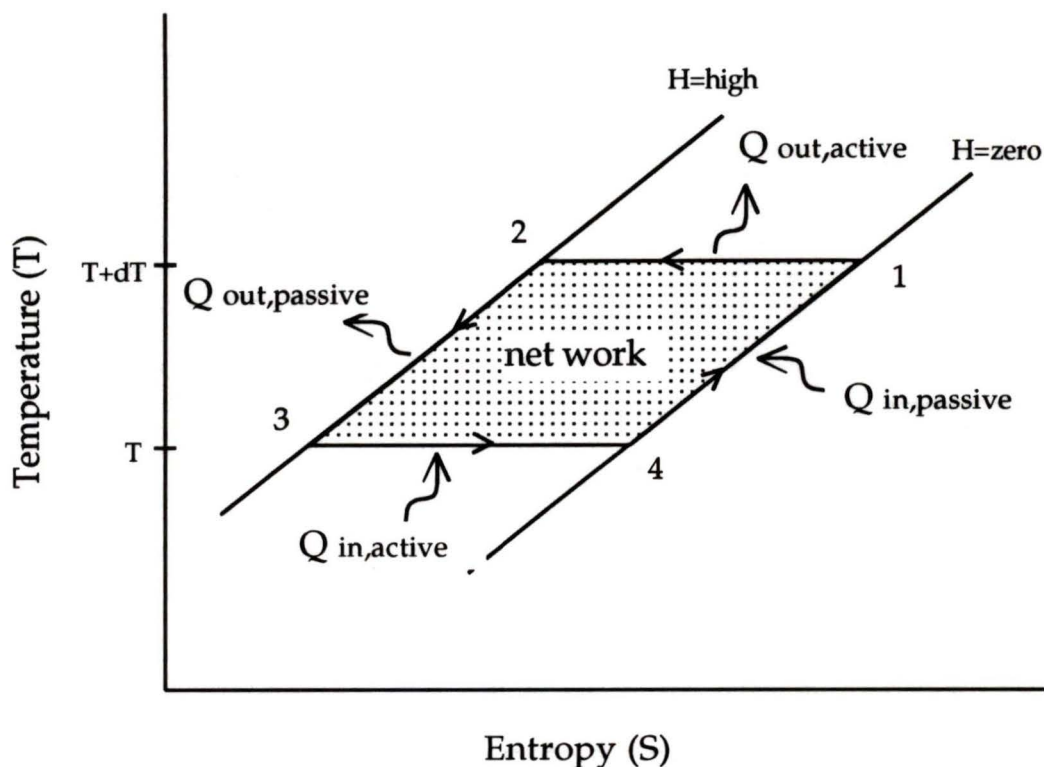


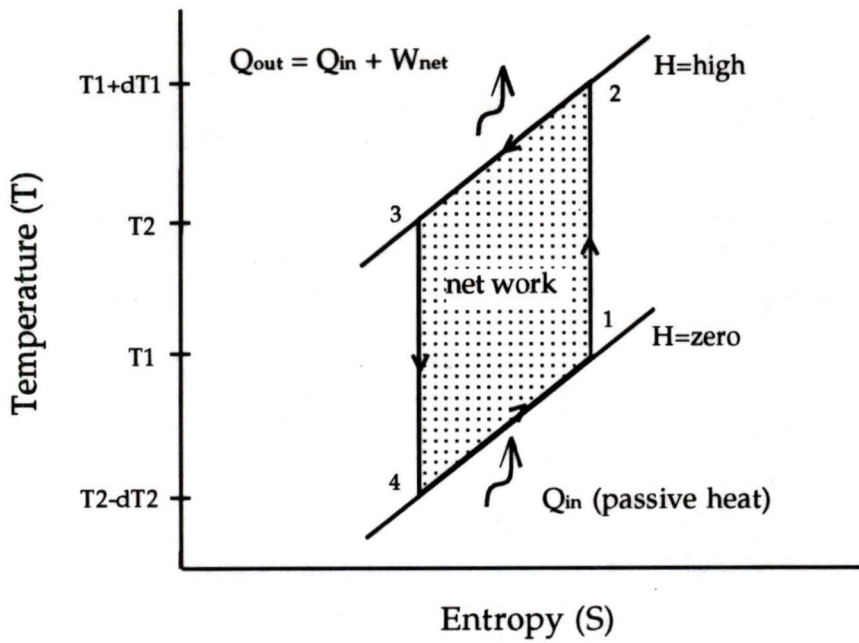
Figure 2.1.1b: T-s diagram for a single material element of an active magnetic regenerator undergoing a magnetic Ericsson cycle.

Recall that the schematic is for an infinitesimally small magnetic element, and although the field lines look parallel, on a macroscopic scale they will not appear that way (the lines must converge at 0 K). In all AMRRs that span large temperature ranges, the magnitude of the regenerative or passive heat transfer will be much greater than the net work or net active heat transfer.

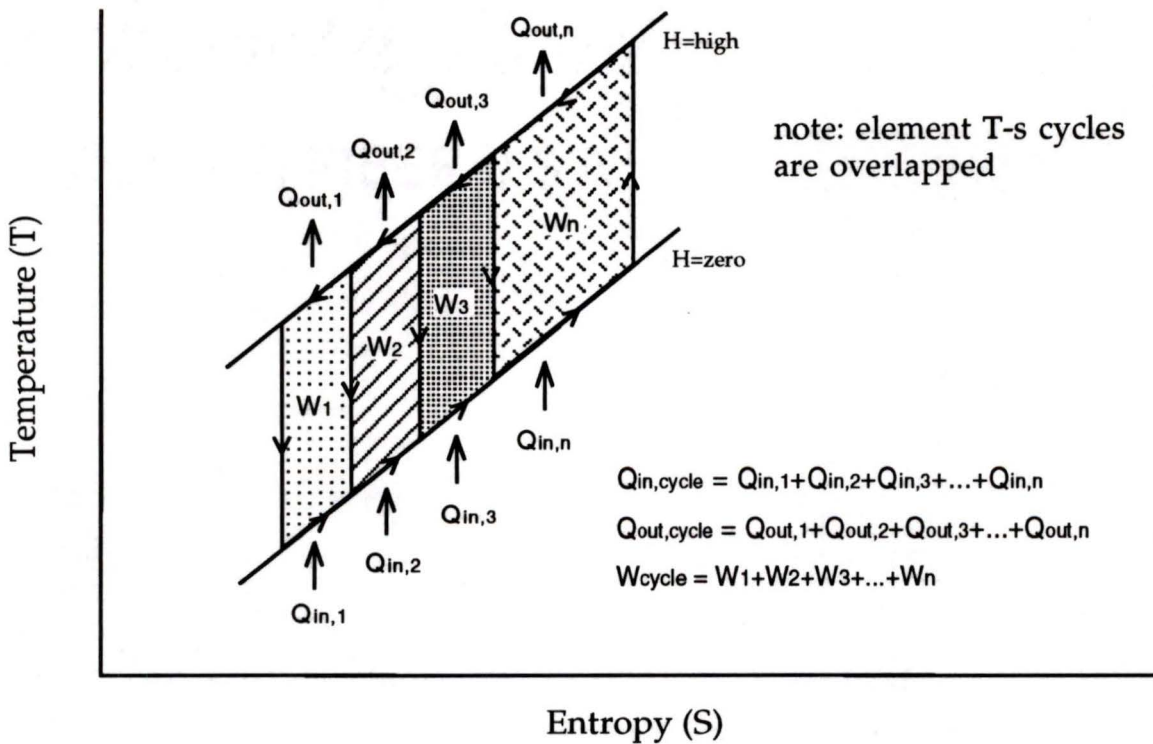
Approximating isothermal heat transfer during the magnetization and demagnetization processes in the AMRR creates complex cycle mechanics. The magnetic field needs to be applied slowly enough while the helium flows through the regenerator. Also, because it is necessary to transfer heat at the cold source and the environment, approximating isothermal heat transfer at these points would require expensive heat exchangers with extremely large

specific surface areas. The device could be greatly simplified by operating the material under a magnetic Brayton cycle by changing the isothermal processes to adiabatic processes. This requires heat transfer to occur across a temperature gradient at the hot and cold end heat exchangers (required for realistic heat exchanger design), and reduces heat transfer to only two of the four material cycle processes. The drawback is that the heat transfer across a temperature gradient will cause the ideal efficiency of a Brayton cycle to be less than that of an Ericsson cycle.

Consider a single element of magnetic working material executing a magnetic Brayton cycle in an AMR. Figure 2.1.1c (i) shows the cycle processes on a temperature-entropy (T-s) diagram. In process 1-2, the material is magnetized adiabatically by some high field. Process 2-3 accounts for all of the heat transfer to the circulating heat transfer fluid. This heat transfer includes the regenerative or passive heat as well as the power generated or active heat. In process 3-4, the material is adiabatically demagnetized and process 4-1 completes the cycle with the material being regenerated by heat transfer from the circulating fluid. The area enclosed by these process lines represents the magnetic power done by this elemental piece of the AMRR. Figure 2.1.1c (ii) shows a series of magnetic elements in the AMRR as they undergo the processes of the cycle. Note that each element's T-s cycle schematic overlaps the next. Each element deposits and picks up heat energy from the circulating fluid and is relatively independent of the other material elements. Again, these figures show both the active heat transfer *and* the large amount of passive heat transfer that is simultaneously occurring. It is assumed in all cycles that the heat transfer fluid mass flow (\dot{m}_f) is balanced between the hot and cold blows [60].



(i)



(ii)

Figure 2.1.1c: (i) Single elemental AMRR material executing brayton cycle. (ii) Series of magnetic elements undergoing unique AMRR cycle.

2.1.2 Material Selection Criteria

When designing a complete AMRR, the fundamental design specification is the cooling power at a given low temperature, \dot{Q}_c . To operate the AMRR, this cooling load needs to be pumped and rejected to the environment as \dot{Q}_h . The energy absorbed and rejected is a product of the helium mass flow, heat capacity and temperature change across the heat exchangers. Even though it is the helium that physically absorbs and rejects the heat, it is the material that drives the gas's hot and cold end temperature gradients. The previous section shows how the fluid and material subsystems are intimately linked and how the magnetic material communicates the cycle power. To achieve a given cooling power specification, there are two definite conditions that the magnetic material in the regenerator must meet (at a given applied magnetic field). These conditions are:

- The material must provide the heat transfer fluid with enough adiabatic temperature change at the cold end to pick up the required heat load and enough adiabatic temperature change at the hot end to deposit that load, the net power input, and entropy generated during the cycle operation to the environment.
- The material must do enough net power to satisfy the thermodynamic requirement of $\dot{Q}_h - \dot{Q}_c = \dot{W}_{\text{cycle}}$, and it must be able to impart that power to the circulating fluid through active heat transfer.

These two conditions constitute the thermodynamically derived selection criteria for the regenerative magnetic material in an AMRR.

2.2 Reversible AMRRs

To better understand the AMRR material selection process based on the above criteria, the selection of an ideal magnetic material for operation in a reversible AMRR will be discussed first. Figure 2.1.1c (i) shows the T-s diagram of an elemental segment from an AMRR. The magnetization and demagnetization processes are essentially reversible. If the heat transfer coefficient between the material element and the circulating fluid is infinitely high, there is no entropy generation during the heat transfer processes. If it is further assumed that the material has infinite thermal mass compared to the fluid, there will be no entropy generation due to thermal energy depletion of the solid (there must be some energy depletion or washing of the solid for the cycle to operate but it is assumed to be infinitesimally small in the reversible case). Finally, it is also assumed that there is no parasitic longitudinal or transverse heat conduction either. For this reversible case, the entropy load is picked up at the cold end by the heat transfer fluid and is shuttled through the regenerator and deposited at the hot end, again by the helium, with no additional entropy loads coming from the regenerative process. The ideal AMR material to accomplish this task must satisfy the above thermodynamic criteria. For the device being built at Cryofuel Systems, the specified cooling power is 700 W. Using the relationship:

$$\dot{m}_f c_p \Delta T_c = \dot{Q}_c \quad (2.1)$$

where $\dot{m}_f = 0.096 \text{ kg/s}$ and $c_p = 5200 \text{ kJ/kgK}$ (for helium), the temperature gradient required in the fluid at the cold end heat exchanger is 1.4 K. With an infinite heat transfer coefficient, the solid and fluid temperatures will track each other exactly, specifying the material adiabatic temperature change at the cold end to also be 1.4 K. The required temperature gradient of the helium at the hot end heat exchanger to reject the cooling load can be calculated from

basic thermodynamic principles. The Brayton efficiency for a reversible cycle is defined as:

$$\begin{aligned}\text{COP}_{\text{Brayton}} &= \frac{\dot{Q}_c}{\dot{W}_{\text{rev}}} = \frac{\dot{Q}_c}{\dot{Q}_h - \dot{Q}_c} \\ \dot{Q}_h &= \dot{Q}_c (1 + 1 / \text{COP}_{\text{Brayton}}) \\ \dot{m}_f c_p \Delta T_h &= \dot{m}_f c_p \Delta T_c (1 + 1 / \text{COP}_{\text{Brayton}}).\end{aligned}$$

With constant specific heats and balanced mass flows,

$$\Delta T_h = \Delta T_c (1 + 1 / \text{COP}_{\text{Brayton}}). \quad (2.2)$$

The reversible Brayton efficiency can also be expressed as:

$$\text{COP}_{\text{Brayton}} = \frac{\bar{T}_c \dot{S}}{\bar{T}_h \dot{S} - \bar{T}_c \dot{S}} = \frac{\bar{T}_c}{\bar{T}_h - \bar{T}_c}. \quad (2.3)$$

In Equation 2.3, the average hot and cold heat transfer temperatures are used. This reflects the non-isothermal heat transfer that occurs in a Brayton cycle. By inserting Equation (2.3) into Equation (2.2),

$$\begin{aligned}\Delta T_h &= \Delta T_c \left(1 + \frac{\bar{T}_h - \bar{T}_c}{\bar{T}_c} \right) \\ \Delta T_h &= \Delta T_c \left(\frac{\bar{T}_h}{\bar{T}_c} \right) \\ \frac{\Delta T_h}{\Delta T_c} &= \frac{\bar{T}_h}{\bar{T}_c}.\end{aligned} \quad (2.4)$$

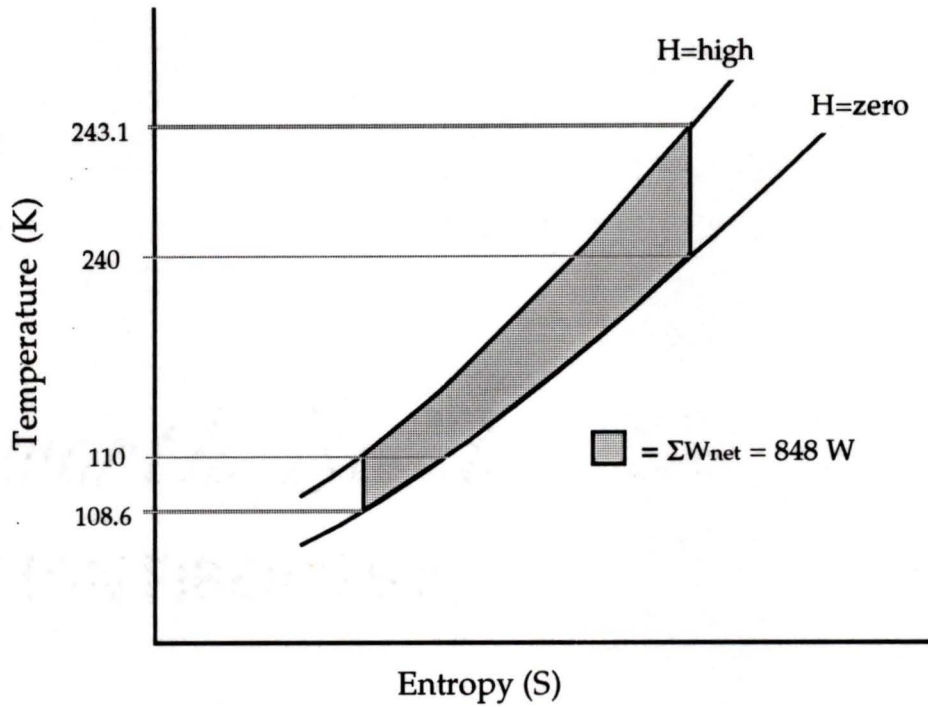
Equation 2.4 specifies that in a reversible case, the temperature gradients required at the hot and cold ends of the device are directly proportional to the average absolute hot and cold temperatures at which the fluid heat transfer takes place (i.e the average temperature at which the helium absorbs heat from the natural gas and at which it rejects heat to the environment). An approximation to the average hot and cold temperatures is:

$$\frac{\bar{T}_h}{\bar{T}_c} \approx \frac{T_h + \Delta T_h / 2}{T_c - \Delta T_c / 2} \quad (2.5)$$

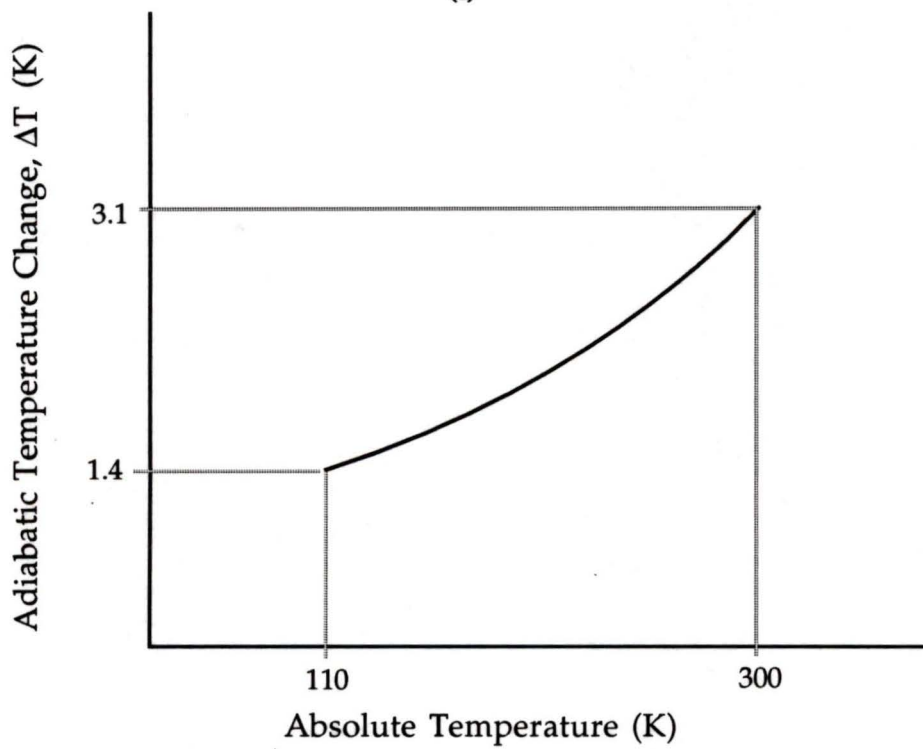
With $\Delta T_c = 1.4$ K and a temperature span of 110 K to 240 K for the device under consideration, the ΔT_h required for the helium will equal 3.1 K under reversible conditions. Recall that the heat transfer fluid and material temperatures are the same in the reversible case and consequently, these hot and cold temperature gradients represent the material's required adiabatic temperature changes at the ends of the active magnetic regenerator. For the reversible case, these boundary adiabatic temperature changes set the first criteria that the ideal material must meet.

The second criteria stipulates that the material must do the minimum required power to operate the cycle. This power will be equal to $\dot{Q}_h - \dot{Q}_c$. Using $\dot{Q}_h = \dot{m}_f c_p \Delta T_h =$, the power required for the reversible prototype is 848 W.

Figure 2.2a (i) shows the envelope of the T-s diagram for a possible single ideal material that satisfies the criteria for the prototype working under reversible conditions (i.e. adiabatic magnetization and demagnetization processes for internal material elements are not shown). Recall that the total net power is not equal to just the two dimensional shaded area.



(i)



(ii)

Figure 2.2a: (i) Envelope of T-s diagram of single material for a reversible AMRR. (ii) ΔT_{ad} vs T profile of the same material.

The shaded area represents the overlapping cycles of each infinitesimal element bounded by the high and zero magnetic field lines. Figure 2.2a (ii) shows the T-s diagram of (i) converted to a ΔT_{ad} vs T diagram. The ΔT_{ad} vs T profile is characteristic of a material that meets the specified criteria, but it is not the only material that will suffice. While the end points of the profile are fixed by the first criteria, the path (for a reversible case) through the temperature span is subject only to the constraint of the material doing the required amount of power. The area under the ΔT vs T profile is representative of the power area on the T-s diagram. This means that the path can be changed as long as the integrated net power of each material element satisfies the basic thermodynamics and boundary conditions (see Figure 2.2b).

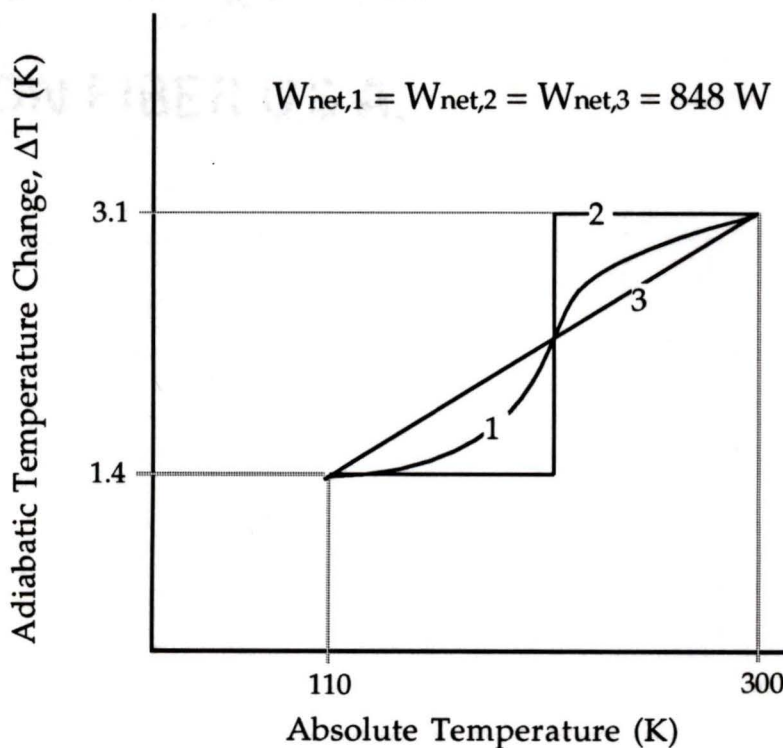


Figure 2.2b: Possible ΔT_{ad} vs T profiles that satisfy reversible AMRR requirements.

To summarize, an ideal magnetic refrigerant for a reversible AMRR must satisfy the net power and ΔT_{ad} boundary conditions outlined previously. These conditions do not specify a unique material, as several different materials could satisfy the criteria. This is a departure from the previous theory that suggested there was a unique material(s) with a specific ΔT_{ad} versus T profile. This uniqueness was a result of the misconception that the cooling load entropy in an AMRR was pumped from one solid element to another creating a constant solid entropy flux. The theory presented here shows that the material elements operate independently and communicate only with the circulating heat transfer fluid. The heat transfer fluid, in turn, communicates with the cold source and the environment. The linked fluid and solid subsystems combine to make up the overall AMRR thermodynamic system.

2.3 Real AMRRs

The purpose of establishing the theory of a reversible AMRR is to establish the magnetic material selection criteria. In a real AMRR cycle with entropy production, the principles behind the reversible selection criteria are still valid, but fluid and solid subsystems links are modified. This section investigates the impact of an entropy producing system on the selection of ideal magnetic refrigerants for a real AMRR. In a real cycle, the entropy producing mechanisms are:

- finite heat transfer coefficient causing heat exchange across a temperature difference (between the solid and fluid):

$$\dot{S}_{ht} = \frac{\dot{Q}_r}{N_{tu} + 1} \left(\frac{1}{\bar{T}_c} - \frac{1}{\bar{T}_h} \right); \quad (2.6a)$$

- longitudinal conduction effects:

$$\dot{S}_{cond} = \frac{\lambda a_c (\bar{T}_h - \bar{T}_c)^2}{L \bar{T}_h \bar{T}_c}; \quad (2.6b)$$

- fluid entrainment in the void of the regenerator as the regenerator cycles in and out of the magnetic field causes heat transfer across the adiabatic temperature span:

$$\dot{S}_{void} = \frac{\dot{Q}_{nf} \Delta T_{ht}}{\bar{T}_{nf}^2}; \quad (2.6c)$$

- pressure drop as the fluid passes through the regenerator and other flow spaces :

$$\dot{S}_{pdrop} = \frac{\dot{V}_f \Delta P}{\bar{T}_h}; \quad (2.6d)$$

- and all other mechanisms such as heat leaks, seal leaks (flow mixing), eddy currents, etc., are \dot{S}_{other} .

Also, in a real AMRR, the material will have a finite thermal mass. This means that the fluid will deplete/replenish thermal energy to/from the solid as it passes over it. We define this to be the "thermal washing" effect. The consequences of these entropy producing mechanisms and finite thermal mass on the material selection criteria are as follows:

- The effects of finite heat transfer coefficient, entrained fluid and thermal

washing will combine to create a difference between the adiabatic temperature changes of the solid and the fluid exit temperature at the hot and cold ends of the regenerator (e.g. ΔT_c is no longer equal to ΔT_{ad}). This means that the material adiabatic temperature changes at these boundaries must be greater to provide the same cooling power. For the cold side (this also applies to the hot side), the available temperature gradient across the cooling load heat exchanger is:

$$\Delta T_c = \Delta T_{ad,c} - \Delta T_{ht} - \Delta T_{void,c} - \Delta T_{wash} / 2. \quad (2.7)$$

The ΔT_{wash} term is divided by 2 to allow averaging over the blow duration.

- A finite heat transfer coefficient means that the fluid temperature will lag the solid temperature. This means that T_{solid} is not equal to T_{fluid} throughout the regenerator. The second material selection criteria states that the material must be able to do the minimum required power and to pass on that power to the fluid in the form of heat transfer. If the heat transfer coefficient is too low, the power done by the material will not be able to adequately communicate with the fluid to satisfy the system requirements.
- Finite thermal mass of the material will require the selection of the material mass to maintain the required ΔT of the fluid at the hot and cold end heat exchangers (i.e. in light of thermal washing effects), as well as to provide the needed passive and active regeneration (discussed in section 2.3.3).

2.3.1 ΔT Boundary Conditions Criteria

Because of the entropy producing mechanisms, Equation (2.4) must be modified to establish the new adiabatic temperature changes at the hot and cold ends of an ideal material for a real cycle. Adding all of the regenerator entropy generation terms yields

$$\dot{S}_{gen} = \dot{S}_{ht} + \dot{S}_{long} + \dot{S}_{void} + \dot{S}_{other}. \quad (2.8)$$

The regenerator 2nd law efficiency will be a ratio of the reversible power to the actual power, or:

$$\eta_{reg} = \frac{\dot{W}_{rev}}{\dot{W}_{act}} = \frac{\dot{Q}_c (\bar{T}_h / \bar{T}_c - 1)}{\dot{Q}_c (\bar{T}_h / \bar{T}_c - 1) + \bar{T}_h \dot{S}_{gen}}. \quad (2.9)$$

The \dot{S}_{pdrop} term is not added to the \dot{S}_{gen} term because the pressure drop entropy produced is paid for in the fluid pump, not in the regenerator. The first line in Equation (2.2) for an AMRR cycle is rewritten as

$$\begin{aligned} \text{COP}_{\text{Brayton, rev}} &= \frac{\dot{Q}_c}{\eta_{reg} \dot{W}_{act}} \\ \text{or } \text{COP}_{\text{Brayton, rev}} \eta_{reg} &= \frac{\dot{Q}_c}{\dot{Q}_h - \dot{Q}_c}. \end{aligned}$$

Again, with constant specific heats this becomes

$$\Delta T_h = \Delta T_c + \Delta T_c \left(\frac{1}{\eta_{reg} \text{COP}_{\text{Brayton, rev}}} \right). \quad (2.10)$$

Substituting Equation (2.3) gives

$$\Delta T_h = \Delta T_c + \Delta T_c \left(\frac{\bar{T}_h - \bar{T}_c}{\bar{T}_c \eta_{\text{reg}}} \right). \quad (2.11)$$

In the reversible case, the material and the fluid temperatures are the same. In the real case, the fluid temperature will lag the solid temperature. Because the fluid picks up and rejects heat and entropy loads in the overall cycle, the fluid temperature undergoes direct thermodynamic scaling. Substituting Equation (2.7) into (2.11) and adding the appropriate subscripts gives:

$$\Delta T_{\text{ad},h} = \Delta T_{\text{ad},c} + \Delta T_c \left(\frac{\bar{T}_h - \bar{T}_c}{\bar{T}_c \eta_{\text{reg}}} \right). \quad (2.12)$$

Equation (2.12) sets the required adiabatic temperature changes at the hot and cold ends for a material operating in a real AMRR.

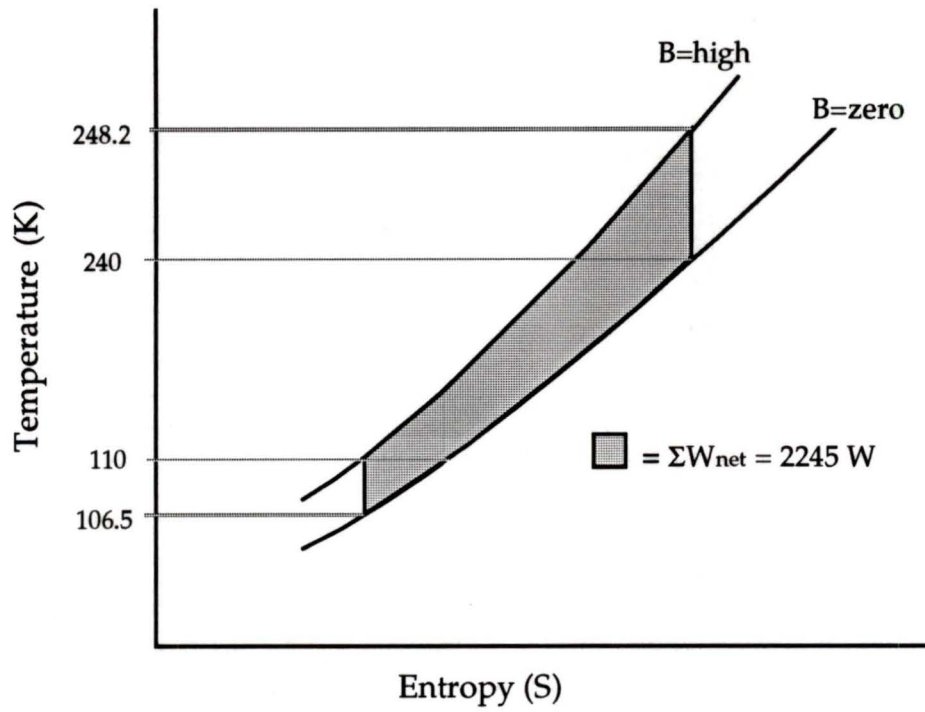
For the prototype refrigerator with 700 W of cooling power, the fluid needs 1.4 K of a temperature gradient across the cold end heat exchanger to pick up the cooling load at 110 K. In the reversible case, this means that the material has to undergo a 1.4 K adiabatic temperature change to accomplish this. In the real case, the material's ΔT_{ad} must be calculated from Equation 2.7. With ΔT_{wash} of the material = 3 K; $\Delta T_{\text{ht}} = 0.5$ K, and $\Delta T_{\text{void},c} = 0.1$ K, the value of $\Delta T_{\text{ad},c}$ is 3.5 K (please see Appendix B for all detailed calculations). From Equation 2.9, the η_{reg} is 0.41. With $\Delta T_c = 1.4$ K, Equation 2.12 gives a $\Delta T_{\text{ad},h} = 8.2$ K. Using Equation 2.7 and applying it to the hot side, the $\Delta T_h = 5.9$ K. Hence, for a material operating in the real prototype, it must undergo an adiabatic temperature change of at least 3.5 K at the cold end (110 K) and 8.2 K at the hot end (240 K) to satisfy the boundary condition criteria.

2.3.2 Work Criteria

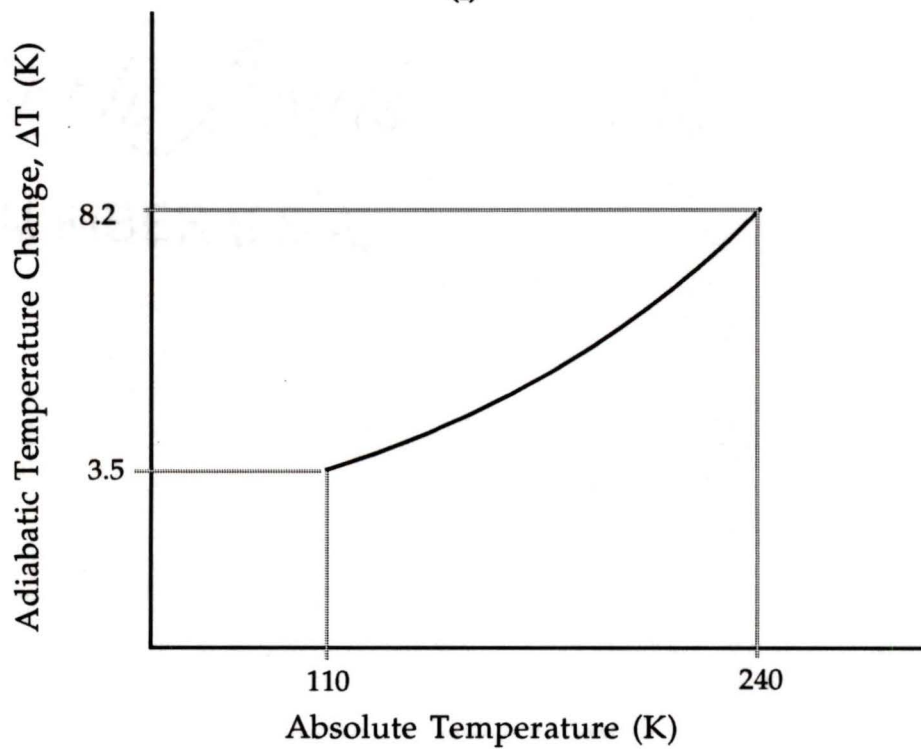
The work criteria states that the material must be able to provide the minimum required thermodynamic power to operate the cycle. For this prototype the power required will equal $\dot{Q}_h - \dot{Q}_c$ or $2945 \text{ W} - 700 \text{ W} = 2245 \text{ W}$ (where $\dot{Q}_h = \dot{m}_f c_p \Delta T_h$). The material must provide this magnetic power at 6T applied field for the cooling specification to be met. To check that the enough magnetic material is used in the regenerator to perform the active power required, the power for a typical material element must be evaluated. The required magnetic mass to do the magnetic power is calculated by:

$$\dot{m}_{s, \text{active}} = \frac{\dot{W}_{\text{req}}}{\bar{T}_{\text{wash}, h} \Delta S_{\text{wash}} - \bar{T}_{\text{wash}, c} \Delta S_{\text{wash}}} \quad (2.13)$$

where $\bar{T}_{\text{wash}, h}$ and $\bar{T}_{\text{wash}, c}$ are the average heat transfer temperatures that the fluid washes the material during the hot and cold blows respectively. ΔS_{wash} is the specific entropy change of the material as its thermal energy is depleted and replenished (refer to Figure 2.1.1c (i)). Care must also be taken to ensure that this mass of material is enough to provide the passive regeneration to allow the helium to span 110 K to 240 K (this will be discussed in the next section). Figure 2.3.2a (i) shows a material that satisfies both the boundary adiabatic temperature change and power criteria for the prototype device. Figure 2.3.2a (ii) shows the ΔT vs T profile for this material. The path from the cold to the hot end on the curve in Figure 2.3.2a (ii) is essentially a measure of how the magnetic power is distributed along the regenerator for a given washing effect. In the reversible case, the details of this power distribution (and path line) was a non-issue because there was no entropy being produced. In the real case, the power distribution along the regenerator is important because certain ΔT_{ad} versus T profiles will generate less entropy.



(i)



(ii)

**Figure 2.3.2a: (i) Envelope of T-s diagram of single material for real AMRR.
(ii) ΔT_{ad} vs T profile of same material.**

2.3.3 ΔT_{ad} versus T Profile (or active work distribution) Considerations

When the heat transfer fluid is being regenerated, the heat transfer has two components, active and passive. The active heat transfer comes from the magnetization and demagnetization of the regenerator material and the passive heat transfer is the normal regenerative function to span a large temperature gap. Figure 2.3.3a shows a typical regenerator temperature profile (T vs regenerator distance or radius in the case of the prototype) for a passive regenerator.

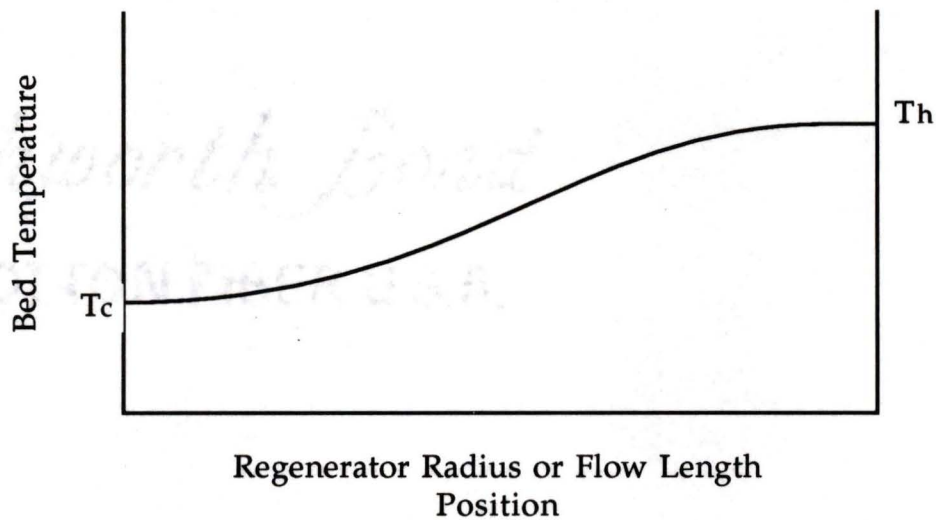


Figure 2.3.3a: Typical passive regenerator temperature vs radius profile.

As long as the combined active and passive temperature profile is positive, the material will transfer power as heat energy to the fluid on the hot blow. If the profile becomes negative, there will be no power transfer to the fluid as well as reverse passive regenerative heat transfer. The material sections undergoing reverse heat transfer during the hot blow represent redundant material and cost in entropy production via the mechanisms discussed above. To prevent this from occurring, ΔT vs T profile of the material must be

chosen so that the T vs regenerator length profile does not go negative after magnetization of the material. Simple differential algebra can determine the maximum negative slope on the ΔT vs T profile to ensure this. If the absolute temperature of the regenerator is a function of the radius (position), and the adiabatic temperature change is a function of the absolute temperature, then the adiabatic temperature change is also a function of the radius. That is, $T = f(r)$, and $\Delta T = g(T) = g(f(r))$. It follows that

$$\begin{aligned}
 T^* &= T + \Delta T = f(r) + g(f(r)) \\
 \frac{dT^*}{dr} &= \frac{df(r)}{dr} + \frac{dg(T)}{dT} \frac{dT}{dr} \\
 &= \frac{dT}{dr} + \frac{dg(T)}{dT} \frac{dT}{dr} \\
 &= \frac{dT}{dr} \left(1 + \frac{dg(T)}{dT} \right) \\
 &= \frac{dT}{dr} \left(1 + \frac{d\Delta T}{dT} \right). \tag{2.14}
 \end{aligned}$$

If the temperature vs radius profile is not to go negative, dT^*/dr must be greater than zero and Equation 2.14 requires that $d\Delta T/dr$ must be greater than -1 (assuming that the passive regenerator profile is already positive, $dT/dr > 0$, as shown in Figure 2.3.3a). These criteria dictate that the material's adiabatic temperature change or MCE cannot decrease by more than one degree per degree of absolute temperature change [61]. All rare earth material elements and alloys being considered for the prototype here have MCE profiles that do not violate this condition.

There are several possible curves that the T vs radius profile can assume while remaining monotonically increasing. Figure 2.3.3b shows several of these profiles.

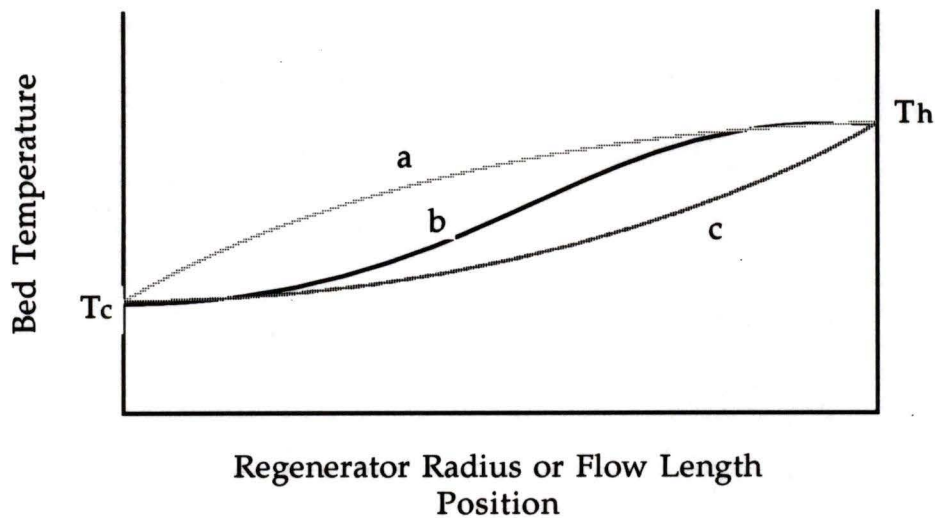


Figure 2.3.3b: Possible monotonically increasing T vs radius profiles.

The entropy producing mechanisms suggest that profile (a) will produce the least entropy [62]. The standard passive profile (b), however, will best represent the real case of the temperature gradient that the regenerator will assume. This T vs r profile is essentially linear except at the ends where longitudinal conduction effects tend to flatten the curve. The active heat generated in the solid because of the magnetic power is only a small percentage of the total heat energy and will have little effect on changing the passive regenerator profile.

2.3.4 Material Mass Optimizing Considerations

The mass of the active magnetic material calculated in Equation (2.13) satisfied the work requirements only. Recall that the magnetic material must also satisfy passive regeneration requirements. For a given material thermal washing effect and heat transfer fluid flow, the amount of magnetic regenerative material required for passive regeneration is calculated from a regenerator balance equation:

$$\dot{m}_f C_p (\bar{T}_h - \bar{T}_c) = \dot{m}_{s, \text{passive}} C_s \Delta T_{\text{wash}} \quad (2.15)$$

The active and passive masses calculated from Equations (2.13) and (2.15) obviously have to be the same in practice. For a given cooling power specification, and given applied field strength, the heat transfer fluid mass flow rate and the washing effects can be selected so that the material mass will be minimized. The effects of these variables are, however, fairly counterbalanced and leave little room for major adjustments. The easiest way to reduce the material mass for a given cooling power is to increase the applied field.

2.4 Real Material Selection

With the thermodynamic criteria, the temperature vs. radius profile considerations, and the refrigerant material mass active and passive relationship known, real materials can be selected that will best operate in the AMRR. Most magnetic materials undergo a MCE when in an applied field. The MCE profile is an adiabatic temperature change versus absolute temperature (ΔT_{ad} vs T) profile for that given material. The MCE can be evaluated against the design parameters and its suitability determined. For the prototype device, there are presently no known single materials that will satisfy the required material's criteria. To get an AMRR that can meet the adiabatic temperature change boundary conditions, several materials must be layered in the regenerator to cover the temperature span.

2.4.1 Ferromagnetic Materials

There are several classes of magnetic materials that can be considered. These

classes are characterized by the magnetic phase changes as the materials go through their transitional temperatures. In general, simple ferromagnets go from paramagnetic to ferromagnetic at the Curie point (see section 1.2.3). A complex ferromagnetic material goes from a paramagnetic phase to some other phase (e.g. some kind of anti-ferromagnetic phase) at a first transition temperature, and then to a ferromagnetic phase at a lower second transition temperature. Dysprosium metal, for example, goes from paramagnetic to helicoidal anti-ferromagnetic at 178 K and then to simple ferromagnetic at 90 K (at zero applied field). At higher field strengths, some of these intermediate phases are destroyed and the material assumes a simple ferromagnetic phase structure [63]. Phase structure will dictate how much and at what temperature the largest entropy changes in the material will occur. Consequently, it also dictates what the MCE or ΔT_{ad} vs T profile for a given material will look like.

For the prototype, the materials considered were heavy rare earth materials and alloys thereof. These materials are primarily simple and complex ferromagnetic systems. This particular group of metals was chosen because they have large magnetic moments, alloy with each other easily (100% solubility), are easily fabricable into regenerator geometries, and are relatively inexpensive.

2.4.2 Boundary ΔT Criteria

The ΔT required in the material at the hot and cold ends was calculated to be 3.5 K and 8.2 K respectively. From the set of heavy rare earth ferromagnetic materials, a single material can not satisfy these boundary conditions. A number of different alloys and elements display the required MCEs at 110 K and 240 K. In the end, dysprosium and an alloy of gadolinium and

dysprosium were chosen because they are the best characterized in literature, and are inexpensive. Dysprosium displays a $\Delta T_{ad,c}$ of ~ 3.5 K in a 6 T field at 110 K and $Gd_{.535}Dy_{.465}$ has a $\Delta T_{ad,h}$ of about 10.0 K at 240 K [64].

2.4.3 Required Work Criteria

To choose materials that will accomplish the required power to make the prototype operate, magnetic refrigerants with the highest magnetic work per unit volume should be selected. This will allow the design to achieve the lowest volume of material. Several different rare earth materials can be selected and layered in the regenerator so that each operates near its transitional temperature and provides the greatest power. However, in an effort to simplify the design, four materials were chosen. The materials consist of gadolinium and dysprosium in either elemental or alloyed form. Table 2.4.3a shows the materials chosen, the magnetic phase transitional temperature, the covered temperature span, and regenerator position. The mass of magnetic material required to satisfy the thermodynamic work criteria can be determined from an analysis of the T-s diagram of a typical element from the chosen rare earths (as outlined above). It should be noted that this will give only an approximate solution to the working mass. The assumed washing effect is 3 K and the average adiabatic temperature change of the materials is 5.6 K. It is further assumed that the element position in the regenerator is chosen so that the change in entropy due to the 3 K washing will be representative of all the selected materials (note that the entropy change/unit volume will be essentially the same for these heavy rare earths). The Δs_{wash} for 3 K temperature change is 4.95 J/kgK. With $\Delta T_{ad,ave} = 5.6$ K, the work represented is 27.7 J/kg. The required power is 2245 W, so the $\dot{m}_{s,active} = 81.0$ kg/s. At 5 Hz operating frequency, 16.2 kgs of material are required to satisfy the active power criteria.

Table 2.4.3a: Chosen Magnetic Materials for the AMRR Prototype

Refrigerant Material	Reference Name	Transition Temperature (K)	Operating Temperature Span (K)	Radial Width in Regenerator (mm)
Gd _{.535} Dy _{.465}	GdDy1	240	225 - 240	5.8
Gd _{.360} Dy _{.640}	GdDy2	219	211 - 225	5.3
Gd _{.184} Dy _{.816}	GdDy3	199	192 - 211	7.5
Dy	-	178	110 - 192	32.4

2.4.4 Transient Start-up Concerns

The AMRR will start to cool from the hot end of the regenerator (the opposite end of a conventional regenerative gas cycle). The magnetic material on the hot end (GdDy1) will do almost all of the magnetic work in the beginning. As the regenerator cools to the magnetic phase transition temperature of each successive magnetic material, those materials will do more work until the device reaches its steady state temperature profile. Because of the "hand-off" nature of the transient behaviour of the AMRR, magnetic materials layered in the regenerator must be chosen so that there are no temperature spans where no magnetic work is being done. If a successive magnetic refrigerant is completely paramagnetic after the previous material has cooled the device to its lowest temperature, the temperature profile development will stall and the device will not start up.

2.4.5 Selected Material Mass Optimization

With $\dot{m}_{s,active}$ calculated, $\dot{m}_{s,passive}$ can be calculated and compared. Using Equation 2.15, $\dot{m}_{s,passive}$ is 125 kg/s and with 5 Hz operation, the total passive heat transfer mass is 25 kgs. In actual operation, the regenerative and active

material masses will be the same. The optimization objective is to minimize the required material to operate the device to reduce superconducting magnet and material costs. Parameters that can be varied to minimize the material mass are cooling power, field strength, helium mass flow rate, wheel frequency (material mass flow rate) and material selection. If the cooling power is specified, the wheel frequency is fixed, and the materials have been selected by availability and cost, the remaining variables are helium mass flow rate and field strength. The above calculated passive material mass requirement is greater than the calculated active mass requirement (the greater of the calculated masses sets the minimum mass requirement). In this case, the helium mass flow rate can be decreased to minimize the overall material requirement. As the helium mass flow is decreased, the passive mass decreases while the active mass requirement increases (as the washing effect decreases). The desired cooling power might be maintained because the decreased mass flow will, in part, trade off with an increased ΔT_c due to the reduced cold end washing effect. A detailed optimization analysis needs to be done to determine the best selection of the helium mass flow rate because this variable also affects pressure drop and heat transfer coefficient. In general, the helium mass flow variable is strongly linked to several other variables and leaves little room for optimization. The easiest way to reduce required material mass is to increase the applied field. This has the effect of increasing the adiabatic temperature change of all the regenerative material (including the hot and cold ends). This allows the washing effect to be increased for the same cooling power. All other parameters being equal, this will result in an overall decrease in required material mass. Figure 2.4.4a shows the adiabatic temperature change profiles (MCEs) of each material superimposed over one another and the actual ΔT vs T profile for the combined material.

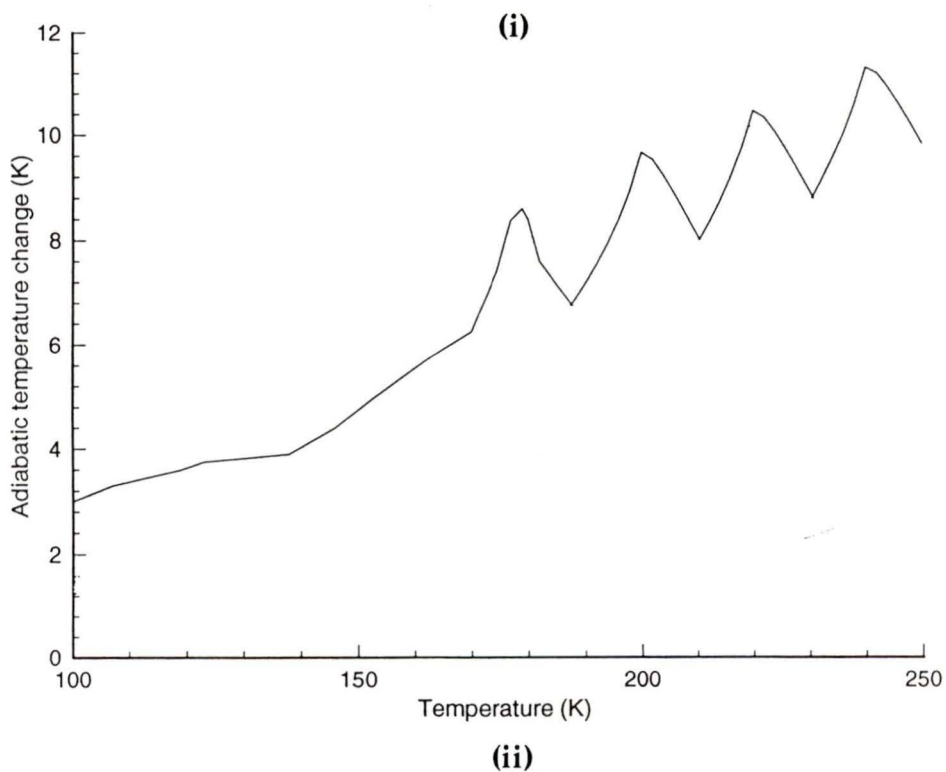
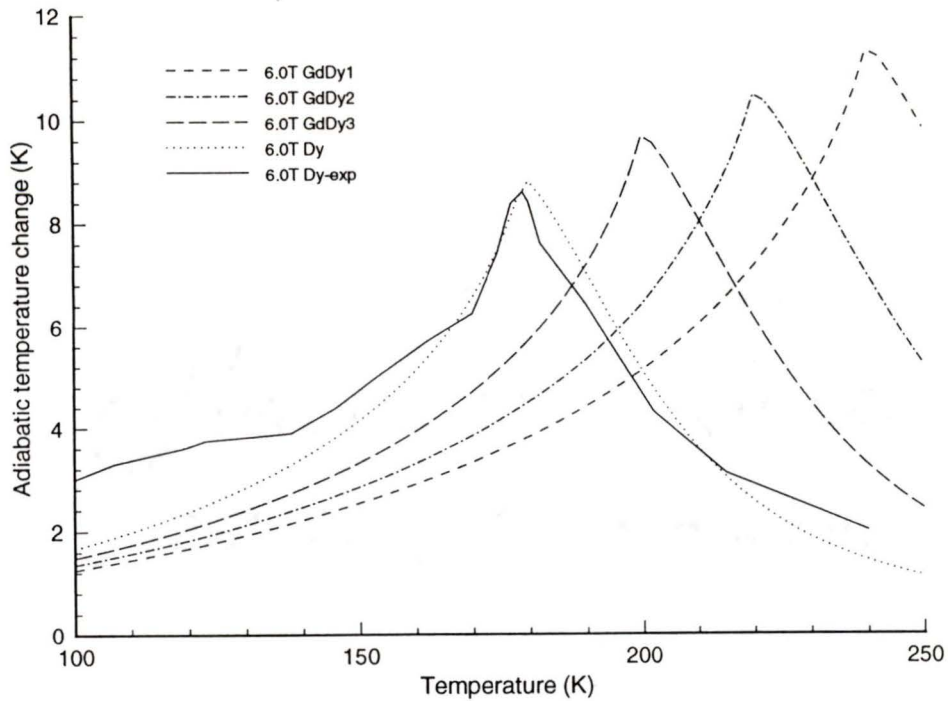


Figure 2.4.4a: (i) Superimposed adiabatic temperature change profiles of the selected materials over the operating temperature range with 6 Tesla applied field (Dy-exp is a measured experimental value [65]). (ii) Resulting composite adiabatic temperature change profile after cropping.

2.4.6 Other Material Properties

So far, the requirements for a good magnetic refrigerant have included high magnetic work/unit volume and proper ΔT s at the hot and cold boundaries of the AMR. At this stage in the selection process, other desirable properties include:

- high densities - This allows the AMRR to be volumetrically small. Because the regenerator is rotated through a superconducting high field magnet, the smaller the regenerator, the smaller the magnet. Consequently, the design will be more cost effective.
- low magnetic hysteresis - The magnetic materials used must be magnetically soft to prevent any hysteretic effect that would reduce the effective magnetic work. Most rare earth materials are magnetically soft near their transition temperatures where they are preferentially used.
- oxide forming - When the materials form small oxide layers on the surface, this helps to electrically insulate the finely divided pieces of material in the regenerator and reduces the eddy current heating. Eddy current heating occurs when small electrical eddy currents are formed when the magnetic material is cycled in and out of a magnetic field. The currents cause parasitic heating that increases with increasing field frequency, field strength, and material volume.
- formable - Magnetic refrigerants need to be formable with high toughness to be made into various regenerator geometries with minimum fabrication effort.

- inexpensive - Because large amounts of magnetic material need to be used in the AMRR, it is important that they are relatively inexpensive. Table 2.3a shows the cost/kg for several of the heavy rare earth materials [66].

Table 2.3a: Quoted Prices for some Heavy Rare Earth Materials

Rare Earth Material	Cost/kg (U.S. \$)
Gadolinium	255.00
Terbium	840.00
Dysprosium	265.00
Erbium	570.00

Note: Specified purity is 99.9%

Gadolinium and dysprosium were partly chosen because they are the most inexpensive of the heavy rare earth materials.

Chapter 3

Preparation of Magnetic Materials

The rare earth group of elements presents several viable candidate materials that can meet the selection criteria as outlined in the previous section. The four materials chosen were selected based on the MCE and overall characterization that is available in the literature. Several other materials appear to have excellent potential as magnetic refrigerants in the desired temperature range, but because of a lack of published MCE data, it is impossible to quantitatively characterize and select these materials. It was necessary to prepare several of these materials so that MCE characterization could be done and their suitability examined.

3.1 Selected Alloys

In addition to the alloys listed in Table 2.4.3a, several other rare earth alloys have been prepared to assess their suitability. Appendix C shows all the selected alloys that were prepared by Cryofuel Systems, their suspected phase transition points, and their magnetic phase diagrams (as well as other promising identified refrigerants).

3.2 Commercial Grade Rare Earth Materials

All rare earth materials used in our research have been commercially purchased as 99.9% pure by weight (except erbium which was 99% pure). This percentage means that the metal will contain 99.9% rare earths by weight. The actual purity of the specific metal may be as low as 99%. Materials used for pure science research on rare earth materials can approach purities of 99.999% of the target element and cost substantially more. Because any commercial application of magnetic refrigeration will ultimately be successful on economic considerations, all samples used for characterization and regenerator fabrication were commercial grade. Table 3.2a shows the chemical breakdown for a typical purchased ingot of dysprosium [67].

Table 3.2a: Chemical Analysis of 99.9% Pure Dysprosium Ingot

Element	% pure by weight	parts per million (PPM)
Rare Earth Metal	99.9 min	-
Dysprosium	99.0 min	-
Gadolinium	-	2 max
Terbium	-	100 max
Holmium	-	510 max
Erbium	-	5 max
Yttrium	-	5 max
Iron	-	50 max
Silicon	-	50 max
Calcium	-	50 max
Magnesium	-	30 max
Aluminum	-	110 max
Molybdenum	-	100 max
Carbon	-	120 max
Oxygen	-	620 max
Hydrogen	-	200 max

3.3 Alloy Preparation

The samples were prepared by arc melting the materials to form the desired alloy specimen. Pieces of these specimens were mounted in epoxy, ground and polished for microscopic inspection. Sample preparation of rare earth materials cannot be generalized because of the various characteristics of these metals [68]. The rare earths of interest were mostly heavy rare earths (gadolinium through Ytterbium) and the procedures used and developed are for these relatively slowly oxidizing materials.

3.3.1 Arc Melting

All alloy melting was done in a Buehler arc melter located at Royal Roads Military College in Victoria, B.C.. The arc melter was thoroughly cleaned with steel wool, acetone and cloth. Each alloy sample was placed in a specially designed copper hearth to allow six samples of approximately 100 grams each to be processed at once. The hearth and bell jar were water cooled during the melting operation. When the system was properly purged using argon gas, each sample was melted using a pedal controlled electric arc until the charge pooled in the centre of the holder. Each sample was turned over and melted a total of four times and the quick cooling rate of the water cooled hearth helped to ensure the homogeneity of the final alloy.

3.3.2 Sample Mounting and Polishing

Each sample was mounted in an epoxy resin which sets at room temperature in about 5 minutes. After the mould was removed the samples were ground and polished using a Buehler Minimet polishing machine. Several polishing methods are illustrated in the literature but it took some trial and error to

achieve a suitable polishing sequence for our equipment [69]. In general, polishing is done at low wheel speeds and with very light pressure in several steps. Water can be used for the heavier rare earths as the corrosion problem is not so severe. Table 3.3a shows the general grinding and polishing sequences that were used [70].

Table 3.3a: Grinding and Polishing Sequence for Heavy Rare Earth Alloys

	Surface	Lubricant Extender	Abrasive	Time (min:sec)	Force	Speed Setting (RPM)
Planar Grinding Stage	SiC paper	water	240, 400, & 600 grit	2:00 per abrasive	5 lbs	120
Sample Integrity Stage	Metcloth	Metadi Fluid®	6 μm diamond suspension	5:00	5 lbs	120
	Metcloth	Metadi Fluid®	3 μm diamond suspension	5:00	7 lbs	120
	Metcloth	Metadi Fluid®	1 μm diamond suspension	5:00	7 lbs	120
Final Polishing Stage	Microcloth®	Distilled Water	Micropolish®	0:45	5 lbs	120

The result was a near mirror finish that was suitable for etching.

3.3.3 Etching

Many of the rare earth metals and alloys are rather reactive and can have their structures revealed by normal oxidation. For the heavier rare earths etchants were used to prepare the samples for photomicroscopy. Possible

etchants ranged from acetic acid and peroxide mixtures to heat tinting in air. The easiest method that produced satisfactory results was a heat tint etch. This was accomplished by placing the samples in air at 200 °C for one half hour.

3.4 Sample Verification

With the samples prepared, two forms of microscopy were used to verify the sample phase structure: photomicroscopy and scanning electron microscopy. The intra-rare earth alloys are, for most cases, 100% soluble in each other and should display a single phase structure. Figure 3.4a shows the phase diagram for the Dy-Gd system [71].

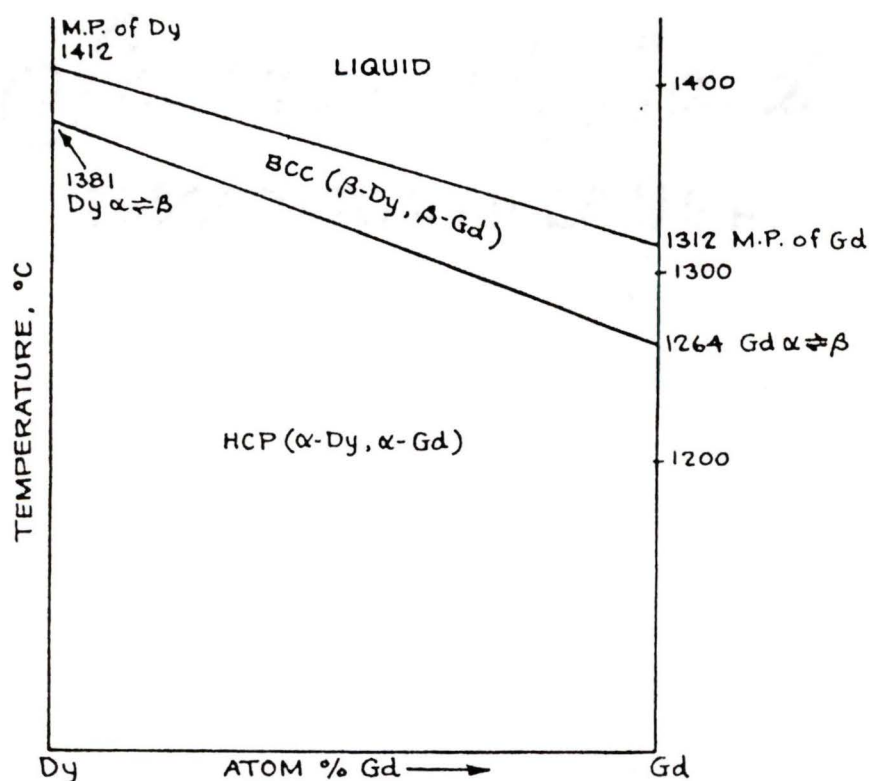


Figure 3.4a: Phase diagram of the Dy-Gd system (schematic only, not to scale)

The above figure shows continuous solubility between high temperature BCC forms and between low temperature HCP forms of Gd and Dy. The low temperature solubility phenomena exists among most binary alloys of the heavy rare earth materials.

3.4.1 Photomicroscopy

Photomicroscopy was essentially used to help verify the uniform phase structure of the alloys and to check for high level contamination. Samples were scanned and photographed using a Nikon inverted microscope (Epiphot-TME). The microscope enables brightfield, darkfield, and chromatic microscopy and photography up to 1000X magnification. Most samples prepared and viewed showed a uniform morphology with no noticeable contamination. A couple of samples showed distinct copper contamination from the arc melter hearth. This was probably caused when the arc was struck on the hearth itself. A secondary phase structure could only come from a large contaminant, but it would be very difficult to differentiate among actual phase structures using this visual method.

3.4.2 Scanning Electron Microscopy (SEM)

To explicitly verify the sample's composition, a scanning electron microscope with an energy dispersion X-ray analyzer (EDXA) was used. This SEM is located at the Defence Research Establishment Pacific (DREP) in Victoria. The SEM was calibrated with 99.9% pure rare earth samples. The EDXA measures relative compositions of samples by counting the x-rays emitted by the atoms of the elements found in the test piece. The x-rays are emitted as the sample is bombarded with electrons. Initial SEM results confirmed the expected composition of all samples tested to be within an acceptable tolerance.

Chapter 4

Characterization of Selected Magnetic Materials

As each material is considered for use as a refrigerant in the AMRR, it must be completely characterized to determine not only its important properties outlined in section 2, but to also determine all important properties necessary for evaluation as a useful passive regenerative material. This requires a compilation of all physical, transport, elastic, mechanical and magnetic properties as a function of temperature. In this section, data on most of the heavy rare earth materials are compiled. For intra-rare earth alloys, most of the properties can be estimated by mole-weighted averaging according to the alloy composition.

4.1 Physical Properties

The physical properties of the candidate materials are essential for a fundamental understanding of the refrigerants. Table 4.1a shows the physical properties of the all the rare earth elements [72].

Table 4.1a: Room temperature physical properties of the heavy rare earth metals and their melting and boiling points; fcc = face-centred cubic, hcp = hexagonal close-packed.

Rare earth metal	Z	Crystal Structure	Lattice constants (Å)		Metallic radius (Å)	Density (g/cm ³)	Melting point (°C)	Boiling point (°C)
			a ₀	c ₀				
Gd	64	hcp	3.6336	5.7810	1.8013	7.900	1313	3273
Tb	65	hcp	3.6055	5.6966	1.7833	8.229	1356	3230
Dy	66	hcp	3.5915	5.6501	1.7740	8.550	1412	2567
Ho	67	hcp	3.5778	5.6178	1.7661	8.795	1474	2700
Er	68	hcp	3.5592	5.5850	1.7566	9.066	1529	2868
Tm	69	hcp	3.5375	5.5540	1.7462	9.321	1545	1950
Yb	70	fcc†	5.4848	-	1.9392	6.965	819	1196

† low temperature form is hcp

4.1.1 Oxide Layer Formation

The oxide forming characteristics of the materials are important when considering their function as regenerators. The oxide layer formed on the refrigerant will help to act as an electrical insulator to help reduce the effects of parasitic eddy current heating. However, the oxide layers formed should not be so great as to reduce the amount of magnetic material concentration in the regenerator or inhibit heat transfer from the material to the heat transport fluid. Acceptable and effective oxide layers range will be a few microns thick at most. The heavy rare earths are relatively slow oxidizers. When exposed to air they will form an oxide layer of about the prescribed thickness before they reach a quasi-equilibrium [73]. Because the magnetic materials will operate in a helium environment, it is conceivable that the oxide layer could be controlled with heat treatments to get the optimum thickness.

4.2 Magnetic Properties

As outlined in the theory section 2, the MCE and the magnetic work/unit volume in a given applied field are the most important parameters that need to be obtained. The magnetic properties of the potential materials are crucial to predicting these parameters. Table 4.2a shows selected magnetic properties for the rare earths [74].

Table 4.2a: Selected magnetic properties of the heavy rare earth metals. S = total spin of 4f electrons, L = orbital angular momentum, J = total orbital angular momentum, T_N = Néel temperature, T_C = Curie temperature

Rare earth metal	S	L	J = L±S	Lande g value	Saturation magnetic moment in Bohr magnetons/atom		G factor	T_N	T_C
					g	observed			
Gd	7/2	0	7/2	2	7.0	7.63	15.8	-	293.4
Tb	3	3	6	3/2	9.0	9.34	10.5	230.0	219.5
Dy	5/2	5	15/2	4/3	10.0	10.33	7.1	179.0	89.0
Ho	2	6	8	5/4	10.0	10.34	4.5	132.0	20.0
Er	3/2	6	15/2	6/5	9.0	9.1	2.6	85.0	20.0
Tm	1	5	6	7/6	7.0	7.14	1.2	58.0	32.0
Yb	1/2	3	7/2	8/7	4.0	-	0.32	-	-

In section 2.2.1, it was explained that the magnetic work per unit volume is a function of the adiabatic temperature change (or MCE) of the material and the washing effect that occurs during operation. In general, the heavy rare earths and alloys considered here will have approximately the same thermal masses (i.e. density * heat capacity) and consequently they will have approximately the same washing effects (for a given helium flow rate). For screening purposes, the magnetic work becomes essentially a sole function of the MCE.

4.2.1 Magnetocaloric Effect

The MCE of a given material, according to Equation 1.1, is a function of the absolute temperature, dM/dT and heat capacity at a constant field, and the magnetic field applied. The change in magnetization with field is a direct measure of the magnetic entropy liberated:

$$\Delta S_M = \mu_o \int_{H_1}^{H_2} \left(\frac{\delta m}{\delta T} \right)_H dH \quad (4.1)$$

Substituting Equation 4.1 into 1.1 and ignoring the dependency of T/c_H on field:

$$\Delta T_{ad} \approx \frac{T}{C_H} \Delta S_M \quad (4.2)$$

The scaling of the adiabatic temperature change with the T/c_H term is shown for dysprosium in Figure 4.2.1a.

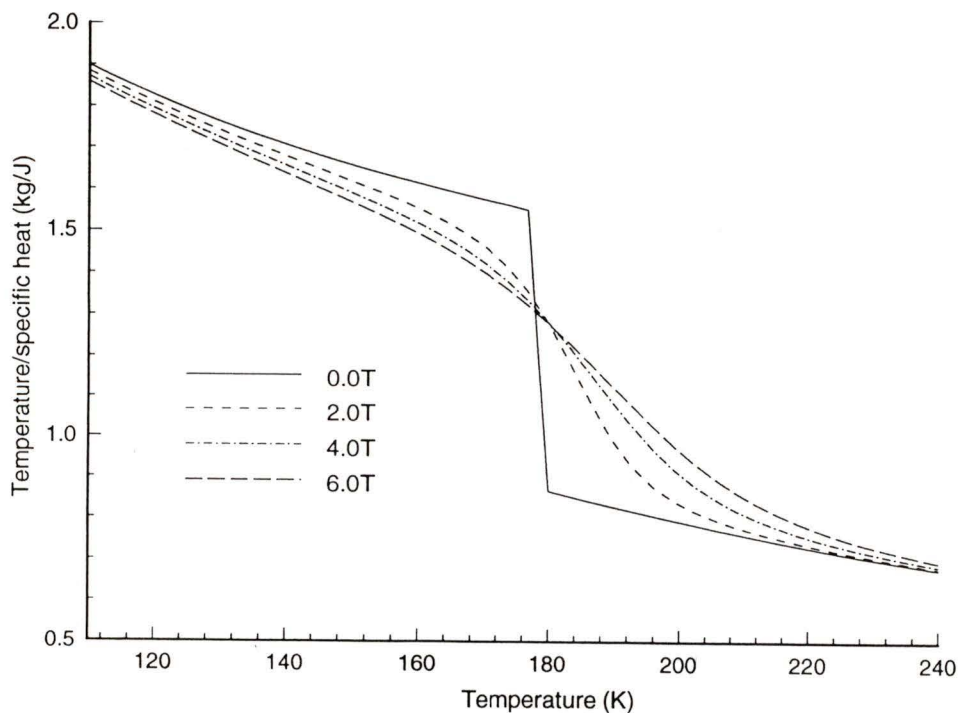


Figure 4.2.1a: T/c_H vs absolute temperature and field for dysprosium.

Figure 4.2.1a shows that the T/c_H term changes very little with field across the temperature range of interest except at the magnetic phase transition point. In the immediate vicinity of this point, the approximation of Equation 4.2 will be more inaccurate. Elsewhere, it gives a good estimate of the adiabatic temperature change.

The main defining factor for the adiabatic temperature change is the magnetic entropy change with applied field. The maximum theoretical magnetic entropy change for a given material under applied fields large enough for magnetic saturation is calculated by:

$$S_M^{\max} = R \ln(2J+1) \quad (4.3)$$

The applied fields in real devices will be much less than those required for magnetic saturation (6 Tesla compared to ~50 Tesla), however, the total angular momentum (J) is a good indication of a materials potential ΔT_{ad} . The higher the J -value, the higher the possibility of larger magnetic entropy changes. Unfortunately, using the magnetic moment to screen a material's potential MCE profile would only help if all the materials were ferromagnetic. In materials with complex phase structures, the magnetic entropy is not changed in a concentrated temperature region around the Curie point, but can be spread across a large temperature range. A certain critical field is required to destroy antiferromagnetic intermediate phases. Table 4.2.1a shows the magnetic structure of the heavy rare earths, the critical fields, and the maximum MCE from experimental data [75]. Referring back to Figure 1.3.4.2a, the MCE as a function of absolute temperature for ferromagnetic gadolinium and other mixed phase heavy rare earths from terbium to thulium is shown.

Table 4.2.1a: Magnetic structures of heavy rare earth metals (FM denotes ferromagnetism, HFM is helicoidal ferromagnetism, and HAFM is helicoidal antiferromagnetism) the maximum critical field for destruction of the antiferromagnetic order $(H_{cr})_{max}$, and the magnitude of the MCE at the temperature $\theta_2(T_c)$.

RE metal	Magnetic structure		$(H_{cr})_{max}$ Oe	$\Delta T_{ad,max}$ K
Gd	FM, $T < T_c = 293$ K		-	14 K H=70 kOe
Tb	FM, $T < T_c = 219$ K	HAFM, $\theta_1 < T < \theta_2 = 230$ K	200	10.5 K H=60 kOe
Dy	FM, $T < \theta_1 = 85$ K	HAFM, $\theta_1 < T < \theta_2 = 178$ K	11000	8.3 K H=60 kOe
Ho	HFM, $T < \theta_1 = 20$ K	HAFM, $\theta_1 < T < \theta_2 = 133$ K	18000	4.5 K H=60 kOe
Er	HFM, $T < \theta_1 = 20$ K	cycloidal structure, $\theta_1 < T < \theta_1' = 53$ K	18000	3.2 K H=60 kOe
		sinusoidal structure, $\theta_1 < T < \theta_2 = 85$ K		
Tm	Fm, $T < \theta_1 = 20$ K	sinusoidal structure, $\theta_1 < T < \theta_2 = 60$ K	29000	1.5 K H=60 kOe

One can quickly see the effect of the magnetic phase structure. Gadolinium, although not shown, has the highest MCE of the heavy rare earths and the classic ferromagnetic caret-like profile [76]. Even though Gd does not have the largest magnetic moment most of the entropy change occurs at one temperature region because of its sharp ferromagnetic phase transition point. In contrast, holmium and erbium have phase structures that reduce the useful magnetic entropy and cause it to be distributed over a wide range of temperatures (this also affects the magnetic portion of the heat capacity).

Fortunately, because of large amounts of research done to experimentally determine the MCEs of the rare earths the job of characterization for the elements and the alloys is simplified. Figure 2.4.4a shows the MCE for the selected materials for the AMRR prototype. The dysprosium and gadolinium profiles were taken from the literature [77] [78], and the MCEs for the Dy-Gd

alloys were interpolated. CFS has developed a molecular field model that was calibrated using the experimental values for dysprosium and gadolinium, then used to create the Dy-Gd alloy ΔT_{ad} versus T profiles. Because the alloys are 100% soluble in each other, most properties will be close to a proportional mixture of the two parent alloys. This proportionality will apply to the MCE and to the primary magnetic transition points. Figure 4.2.1b shows the magnetic ordering temperatures for Gd-Dy alloys [79].

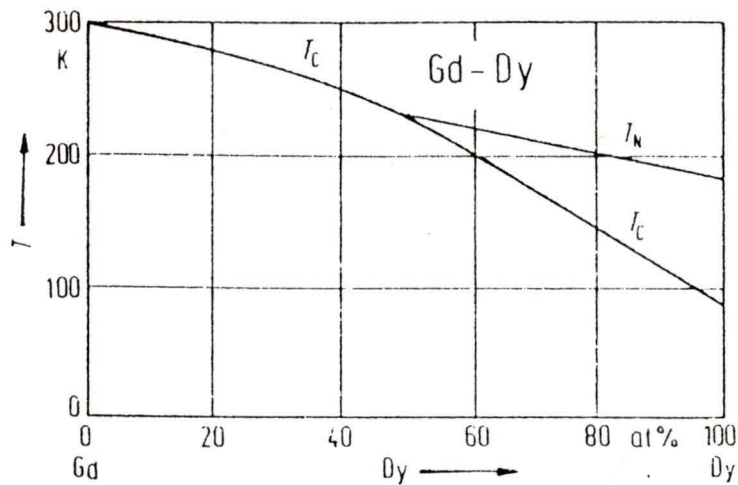


Figure 4.2.1b: Magnetic ordering temperatures for Gd-Dy alloys.

The Université du Québec á Trois-Rivières (UQTR) in Quebec is setting up a 9 Tesla magnetometer that can take magnetization measurements in the temperature range of 4 K - 350 K. Samples of all materials that will be used in the prototype have been sent there to undergo characterization after which the data will be transformed into adiabatic temperature change profiles to confirm the data in Figure 2.4.4a. Presently, UQTR is still awaiting proper installation of their 9T magnetometer [80].

4.2.2 Magnetic Hysteresis

When magnetic materials are magnetized and demagnetized at temperatures away from their magnetic phase transition temperatures, they become increasingly magnetically hard. For adequate operation in the AMRR, all materials must be magnetically soft to remain reversible and prevent parasitic losses. Figure 4.2.2a shows the hysteresis curve for a typical ferromagnetic material near its ordering temperature. All materials in the prototype device will be operating reasonably close to their ordering temperatures except for dysprosium. UQTR will be evaluating the hysteresis of dysprosium at 110 K to assess how magnetically soft the material is at that point.

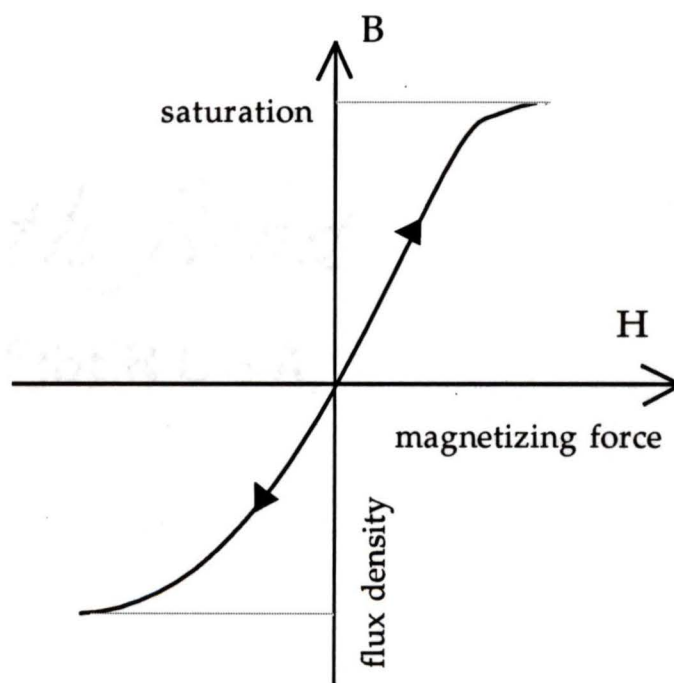


Figure 4.2.2a: Magnetic hysteresis curve for a typical ferromagnetic material operating near its ordering temperature.

4.3 Transport Properties

There are several transport properties that need to be known when selecting materials for the AMRR. The most important of these properties are shown in Table 4.3a for heavy rare earth metals at room temperature [81].

Table 4.3a: Transport properties of some of the rare earth metals (@ 20 °C)

Rare Earth Metal	Electrical Resistivity ($\mu\Omega\text{cm}$)	Coefficient of Thermal Expansion ($\text{K}^{-1} \times 10^6$)	Specific Heat (J/kg K)	Thermal Conductivity (W/mK)
Gd	134	6.4	230	10.5
Tb	116	7.0	183	11.1
Dy	91	8.6	173	10.7
Ho	94	9.5	165	16.2
Er	86	9.2	168	14.5

It is important to characterize many of these properties as a function of temperature. Figure 4.3a shows the electrical resistivity as a function of temperature [82] and Figure 4.3b shows the heat capacity as a function of temperature and field for selected rare earth metals [83].

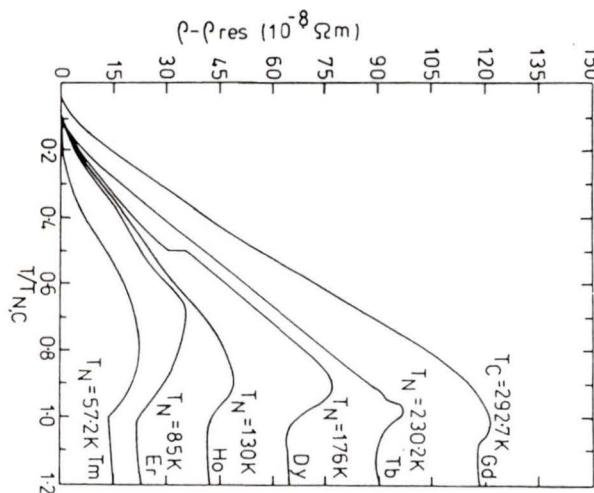
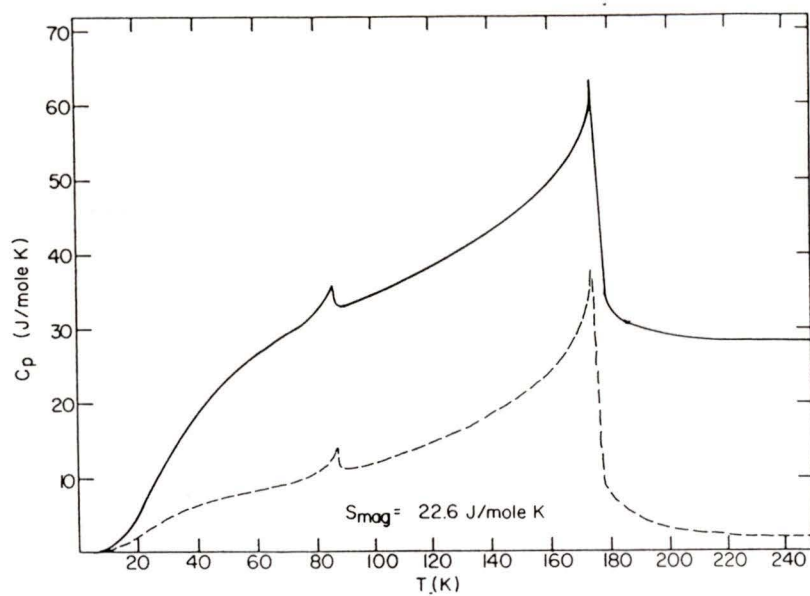
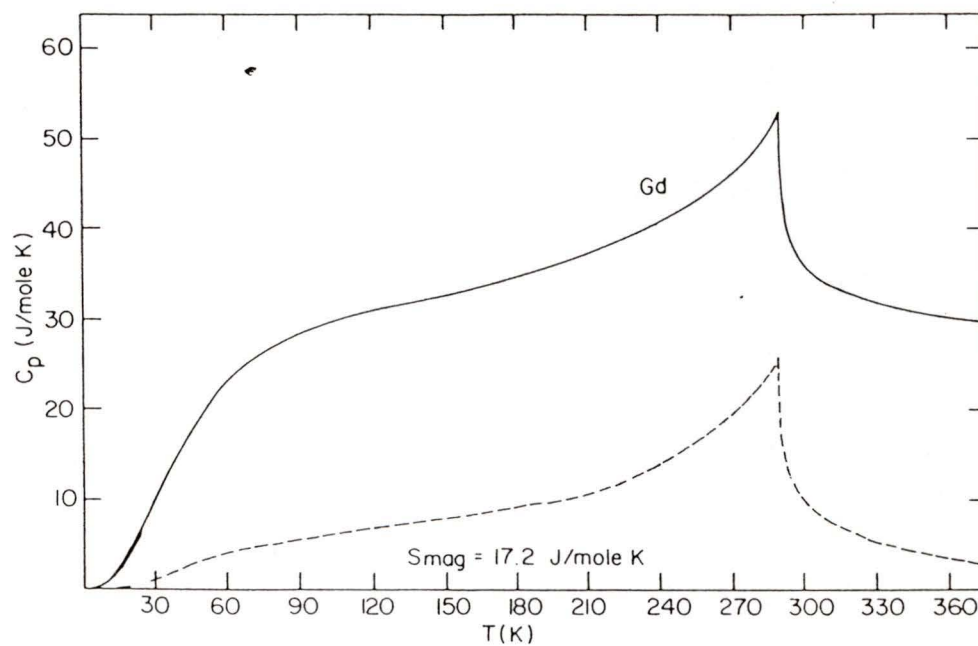


Figure 4.3a: C-Axis electrical resistivity of some heavy rare earth metals as a function of temperature.



(i)



(ii)

Figure 4.3b: Specific heat (i) of dysprosium and (ii) gadolinium as a function of temperature. The dashed curve is the magnetic contribution.

4.4 Mechanical Properties

The AMRR will cycle through a 6 Tesla field at approximately 5 Hz. This will cause large mechanical loading forces and some fatigue effects. It is important to consider mechanical properties of the refrigerants to ensure that they can withstand the loading effects. Table 4.4a shows the most important of the mechanical properties considered and their values for several rare earth materials at room temperature [84].

Table 4.4a: Room temperature mechanical properties of several heavy rare earth metals*.

Rare Earth Metal	0.2% O.Y. Strength in Tension (MPa)	Ultimate Tensile Strength (MPa)	Ultimate Comp. Strength (MPa)	0.2% O.Y. Strength in Comp. (MPa)	Hardness (Brinell, kg/mm ²)
Gd	179	193	N/A	N/A	55-70
Tb	N/A	N/A	696	N/A	90-120
Dy	228	248	510	126	55-105
Ho	221	262	500	N/A	50-125
Er	292	292	764	140	60-95

* polycrystalline metals used in as-cast condition except where noted

The strength and ductility for gadolinium and dysprosium as a function of temperature can be found in Volume 1 of the *Handbook on the Physics and Chemistry of Rare Earths* [85]. In the 100 K to 240 K temperature range, the properties are fairly constant except for the uniform elongation of Gd, which decreases markedly.

Other important mechanical properties include impact and fatigue properties. Data on these properties are sketchy at best. The most recent published impact data were published around 1960 by Love [86]. As cast specimens

having a standard V-notch were tested with a 100 inch-pound capacity machine that had a striking velocity of 11.3 ft/s. Table 4.4b shows his results. There was no impurity analysis available.

Table 4.4b: Impact properties of heavy rare earths (foot-pounds)*

Rare Earth Metal	Temperature = 300 K	Temperature = 477 K
Gd	1.3, 1.3	N/A
Tb	3.1, 3.3	N/A
Dy	1.5, 1.8	2.4, 2.3, 2.0, 2.3, 2.4, 2.1
Ho	6.9, 7.4	N/A
Er	1.3, 1.1	1.4, 1.8, 1.7, 2.4, 2.1, 2.0

* sets of two or more numbers indicate the values of individual tests

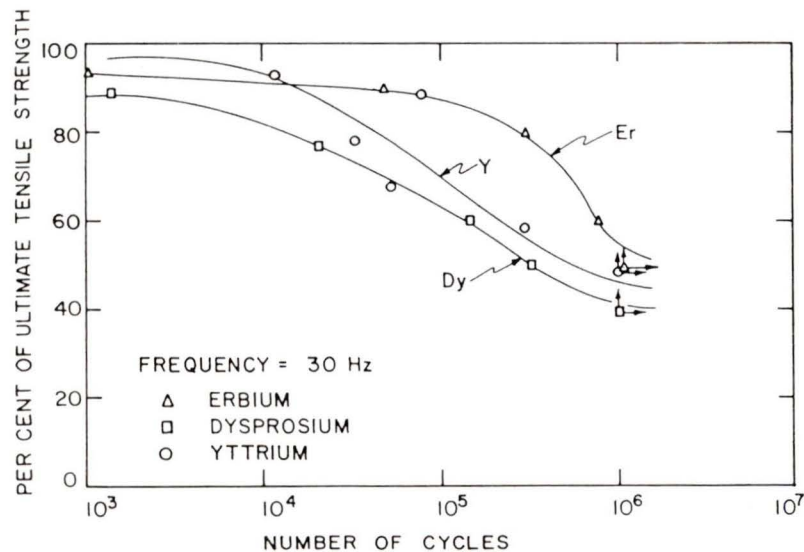


Figure 4.4a: Room temperature tension-tension fatigue life curves for yttrium, dysprosium, and erbium with maximum tensile stress give in terms of the fraction of respective ultimate tensile strengths.

Love also did some fatigue tests on erbium dysprosium and yttrium. They were based on a smooth bar tension-tension test at 30 Hz where the lower stress was always 10% of the upper stress. Figure 4.4a shows the results in

percent of ultimate tensile strength for each metal [87].

4.5 Elastic Properties

The magnetic materials need to be manufactured into regenerator geometries of very finely subdivided shapes to obtain proper heat transfer characteristics. This means that the materials will have to be formed into different, and sometimes intricate, shapes. The elastic properties will give a good indication of the formability of the materials. Table 4.5a shows important elastic properties for several heavy rare earth metals at room temperature [88].

Table 4.5a: Elastic properties of some heavy rare earth metals at room temperature

Rare Earth Metal	Young's Modulus, E (GPa)	Shear Modulus, G (GPa)	Bulk Modulus, K (GPa)	Uniform elongation, annealed cond. (%)	Poisson's Ratio
Gd	56.1	22.3	38.5	37	0.257
Tb	57.5	22.8	40.0	N/A	0.261
Dy	63.0	25.3	41.2	30	0.245
Ho	67.1	26.7	45.8	N/A	0.255
Er	73.3	29.6	46.5	11.5	0.238

Again, the moduli elastic properties of gadolinium and dysprosium as a function of temperature can be found in Volume 1 of the *Handbook on the Physics and Chemistry of Rare Earths* [89].

In general, the properties of the heavy rare earth materials are somewhat similar to other, better known, hexagonal closed packed (HCP) materials such as titanium. These materials have also been compared with iron in terms of their formability characteristics.

Chapter 5

Manufacture of High Performance Active Magnetic Regenerator Media

Once the AMRR materials are selected (as shown in Table 2.4.3a for the prototype), they must be manufactured into highly effective regenerator geometries.

5.1 Selection of Regenerator Geometries

During the operation of the AMRR, the entropy producing mechanisms discussed in Section 2 are largely a function of the regenerator geometry for a given flow rate. Because the adiabatic temperature change associated with an AMRR is much smaller than that of a conventional regenerative gas cycle (approximately 25% the ΔT_{ad} of gas systems), the magnetic system is that much more sensitive to the entropy produced in the regenerator. The regenerator geometry selection will accordingly have a large impact on the overall performance of the refrigerator.

5.1.1 Discussion of Important Regenerator Design Parameters

The important entropy producing mechanisms are:

- solid-fluid heat transfer, \dot{S}_{ht} - The temperature difference between the magnetic solid and the heat transfer fluid directly diminishes the full effect of the material's adiabatic temperature change and will be a major entropy source. This can be minimized by increasing the number of heat transfer units (N_{tu}) of the regenerator. The N_{tu} of a regenerator is evaluated by:

$$N_{tu} = \frac{ha_s}{\dot{m}_f c_{p,f}} \quad (5.1)$$

Equation 5.1 indicates that a high N_{tu} will require a high heat transfer coefficient and regenerator surface area (for a given helium mass flow and heat capacity). The heat transfer coefficient is evaluated from fluid properties and the regenerator configuration [90].

$$h = \frac{c_p \mu}{Pr^{2/3}} \frac{1}{2d_h} (St Pr^{2/3}) Re \quad (5.2)$$

The heat transfer coefficient always varies as the negative power of the hydraulic diameter of the passage through the regenerator, and the hydraulic diameter is defined as:

$$d_h = \frac{4V_T}{a_s} \quad (5.3)$$

The N_{tu} will therefore increase with all regenerator geometries as the regenerator surface area (a_s) increases. To differentiate among geometries, correlations or experimental values must be obtained to determine how the Stanton number varies with the Reynold's number.

- pressure drop, \dot{S}_{pdrop} - Pressure drop through the regenerator matrix causes pumping power dissipation and entropy production. The pressure drop through the regenerator will be a function of the friction factor calculated for a given geometry. The friction factor is defined on the basis of an equivalent shear force in the flow direction per unit of area. It is a combination of viscous shear (skin friction) and pressure force (drag coefficient). Analytically, the friction factor is defined as [91]:

$$f = \frac{\rho \tau_0}{G^2 / 2g_c} \quad (5.4)$$

Each geometrical configuration of the regenerator will have correlated values for the friction factor usually as a function of the Reynold's number. Once the friction factor is calculated, the pressure drop is found from:

$$\Delta P = \frac{\rho v^2 L f}{2d_h} \quad (5.5)$$

where v is the velocity of the fluid in the regenerator. It can be seen immediately that pressure drop reduction and N_{tu} maximization are in direct conflict because of the opposite dependencies with the hydraulic diameter and mass flow rate. Also, the regenerator aspect ratio needs to be considered (i.e. longer regenerators have larger pressure drops).

Often, the regenerator design process ends when some kind of compromise between heat transfer and pressure drop is reached (mass flow's squared dependency with the pressure drop helps design objectives to be met). Kays and London have several plots of compact regenerative heat exchanger surfaces of the friction factor (f) and $StPr^{2/3}$ versus Reynold's number and present graphs showing heat transfer per unit of friction power expended. They are also careful to stress that there are other variable that must be taken

into account for good regenerator design. With the AMRR, this is especially true because of its compactness, magnetic nature, and cycle mechanics. Other important entropy producing variables are:

- longitudinal conduction, \dot{S}_{long} - Longitudinal conduction in regenerators can be a large source of parasitic heat loss and entropy production. There are essentially two forms of longitudinal conduction: solid conduction and fluid conduction (with eddy diffusivity). Solid conduction occurs by heat transfer through the solid matrix in the regenerator from the hot to cold end. Fluid conduction is the parasitic energy loss that occurs through heat conduction in the heat transfer fluid itself (usually very small). Eddy diffusivity is also effective fluid conduction that occurs when the fluid mixes during the flow through the regenerator and forms small recirculation eddies. This is actually a convective process that can result in parasitic losses much greater than the combined conduction losses. It is also the least characterized process. Conduction (and convection) losses are critical in the AMRR prototype device. The regenerator will span 130 K across the length of 5 cms. Total conduction effects can be estimated with proper experimental correlations for the given regenerator geometry. In terms of regenerator geometry, longitudinal conduction effects dictate the degree of solid thermal contact allowed and directly affects aspect ratio concerns (unfortunately in the opposite way as pressure drop considerations).
- fluid entrainment, \dot{S}_{void} - Entropy is created when heat transfer fluid entrained in the void spaces of the regenerator are cycled in and out of the magnetized regions. When the regenerator is magnetized and demagnetized, the solid undergoes rapid temperature changes due to the adiabatic temperature change. This creates entropy as heat flows across the

fluid/solid temperature difference. The entrained fluid also causes dilution (washing) of the material's MCE. In terms of the regenerator geometry, the fluid entrainment is a function of the porosity. Particles, for example, have a void porosity of about 40%. Standard screens, on the other hand, have porosities of approximately 70-80%.

- eddy current heating, \dot{S}_{ec} - Eddy current heating occurs when conductive materials are subjected to fluctuating magnetic fields. Small current loops or eddies are established in the material by the induced electromagnetic forces (emfs) and parasitic heating is created. If large currents are created, the parasitic heat load can be devastating as frequency increases. Eddy current heating is a function of the square of the rate of the magnetic field change (dB/dt), the resistivity of the material, the volume of the material, and the projected surface area of the regenerator material normal to the magnetic field lines. This affects the regenerator geometry design by requiring that configurations be selected with aspect ratios such that the projected surface areas and uninsulated volumes are very small. This means choosing finely divided materials in at least two dimensions and/or finely insulated materials.

The above entropy producing mechanisms provide major design considerations when selecting regenerator geometries. Minimizing the overall entropy production is a good way to guide the design process. It is painfully apparent that several of the mechanisms provide design considerations that are in direct conflict with one another. Several operation compromises are necessary to achieve the lowest entropy production or highest figure of merit (FOM). Another and equally important design concern is cost and manufacturability. It is one thing to conceptualize a geometry that best satisfies the above constraints, and yet another to be able to

manufacture it at an economical manner.

5.1.2 Selection of Potential AMR Geometries

There are several potential regenerator geometries that could be used in the AMRR. Figure 5.1.2a shows six regenerator configurations that were studied.

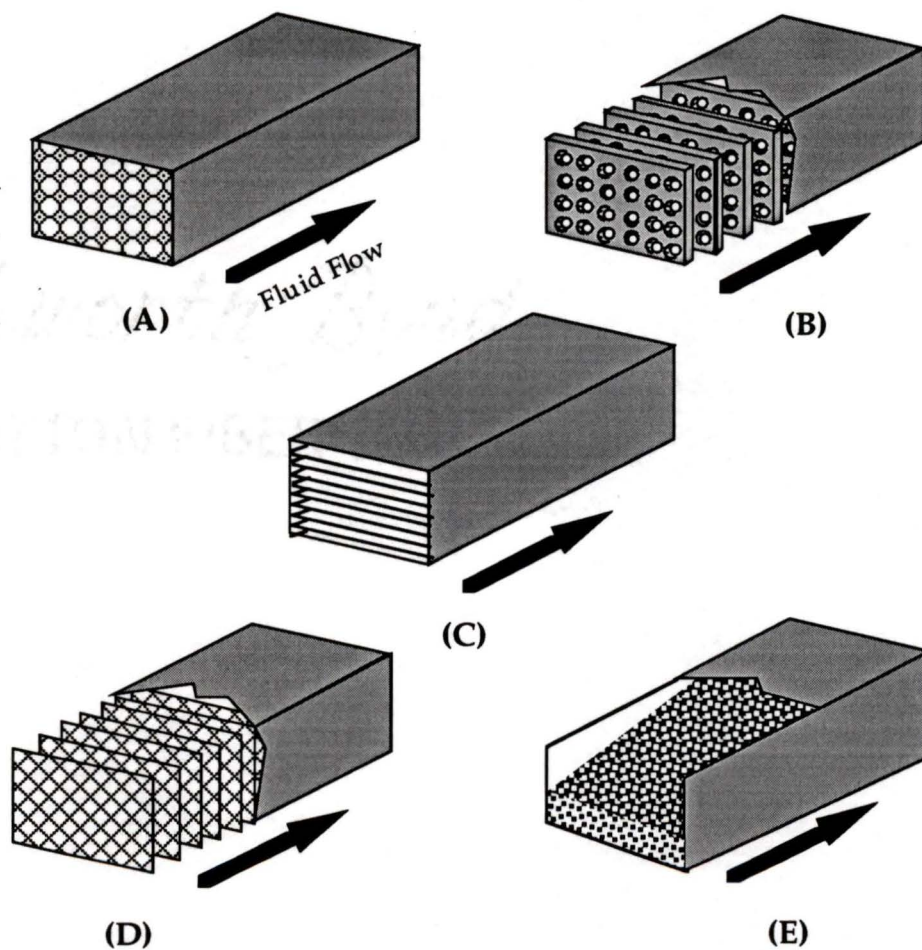


Figure 5.1.2a: Possible regenerator geometries: (A) solid block with longitudinal holes, (B) stack of perforated plates perpendicular to the fluid flow, (C) stack of solid plates parallel to the fluid flow, (D) stack of wire screens (or crossed rods) perpendicular to the fluid flow, (E) packed bed of spherical particles.

After a preliminary study into the expected performance of the above regenerator geometries based on the entropy producing mechanisms as outlined in section 5.1.1, several of the configurations were rejected. Those rejected included:

- block with longitudinal holes - Eddy current generation and longitudinal conduction would be excessive with such a geometry. Surface areas will also be low leading to a lower N_{tu} .
- parallel plate geometry - Same concerns as above. However, with advanced manufacturing techniques (ones that can use fine ribbons with small insulating spacers), designs with larger surface areas with lower pressure drop can be realized [92]. Ultimately, this geometry was not considered further because of the potential manufacturing difficulties and costs. However, it should not be ruled out in future work.
- perforated plate geometry - Preliminary analysis shows that a perforated plate geometry is a good one. Although eddy current generation might be higher because of the flat surface of one dimension, there would be small longitudinal conduction effects, high heat transfer, tunable porosities, and acceptable pressure drops. Again, because of the intricacies of the design and the potential high cost, this geometry was also relegated to future work.

The remaining geometries, packed particles, wire screens, and cross rods were chosen for in-depth analysis. There are several variations on each of these geometries:

- packed particles - Particles can be loose packed, pressure packed or sintered into a monolithic block. For this study, they are considered to be pressure

packed (under about 1.1 MPa or 150 psig) with an overall porosity of about 40%.

- wire screens - Wire screens could be woven in many different ways that will affect their regenerative performance. They could be woven with different horizontal and vertical meshes and/or with different diameter wires. The cost for custom weaving, however, is very high and in most cases vendors were not even tooled to do such a job. The screens could be woven in a standard fashion and pressed to decrease porosities. This also causes a large increase in contact area between adjacent screens increasing the longitudinal conduction and eddy current paths. The screens considered here are all single mesh screens of a constant diameter wire with standard porosities ranging from 55 to 80%.
- crossed rods - Crossed rods are essentially wire screens without the weaving angle. Theoretically, the porosity of crossed rod regenerators would be much more tunable than screens. Barring the significant manufacturing difficulties, crossed rods could have the same porosities as particle beds (i.e. 40%). Crossed rods could be configured in a right angle stack or random angle stack with constant spacing or could be randomly stacked with random spacing as in a mat geometry. Crossed rod results are not presented here because the correlations used for heat transfer and friction factors are not valid under 55% porosities, and in the higher porosity ranges, they behave very similar to wire screens [93].

5.1.3 In-depth Parametric Analysis of Chosen AMR Geometries

Wire screens and particle regenerator performances were analyzed using a Fortran computer program developed for this thesis (program is listed in

Appendix D). The program simulates a passive, a one-dimensional, steady-state regenerator operation. A true rotary AMRR will be two dimensional and have all active magnetic parameters included [94]. The passive steady state performance was analyzed under AMRR prototype conditions to determine the important passive regenerator qualities of the different designs. The geometries were compared by using the regenerator design parameters outlined in section 5.1.1. The entropy produced or generated because of pressure drop, imperfect heat transfer, and fluid entrainment was calculated and an overall figure of merit for each configuration was established. The figure of merit is defined as the ideal power required over the actual power required or:

$$\text{FOM} = \frac{\dot{Q}_c \left(\frac{T_h}{T_c} - 1 \right)}{\dot{Q}_c \left(\frac{T_h}{T_c} - 1 \right) + T_h \dot{S}_{\text{gen}}}. \quad (5.6)$$

The entropy generated because of longitudinal conduction was not factored in because reliable correlations for the eddy diffusivity component for very fine wire screens could not be found. This effect will be estimated by empirical testing that is currently taking place (see section 6.3 for further longitudinal conduction considerations). Also, entropy effects caused by eddy current heating were not factored in because they were calculated to be very small in these geometries (see section 6.2). The assumptions used in the analysis are:

- all design specifications represent operating conditions (see prototype design specifications in section 1.3.3);
- constant average fluid and material properties;
- correlated expressions for the heat transfer coefficient and the pressure drop

(see Appendix D);

- constant thermal washing of the solid under each geometry, and
- field ramp up and down regions together equal to one sixth of the circumference length along the regenerator wheel.

The heat transfer and pressure drop correlations have been taken from well documented literature sources [95] [96] [97]. Although entropy created due to viscous dissipation or pressure drop is paid for in pumping power, pressure drop entropy was included in this FOM analysis as a means of including it in the parametric comparison. To perform a fair comparison of the geometries in terms of fluid entrainment entropy, the thermal washing of the solid was assumed to be constant. Screens can be twice as porous as particle beds which leads to a lower effective density. Consequently, the thermal energy depletion by the heat transfer fluid for the screens will be greater. This has the effect of reducing the adiabatic temperature change of the fluid and leads to lower cooling powers. Because the regenerator volume is fixed, a constant thermal washing effect for geometries with different porosities can be achieved by changing the rotational frequency of the regenerator bed. Therefore, if one geometry has one half of the effective density of another, the bed frequency is doubled. This naturally affects the entropy produced by the fluid entrained as the regenerator is cycled in and out of the high field region. Figure 5.1.3a shows the theoretical FOM for both particle beds and screens while operating under the AMRR prototype conditions. The figure shows three lines of constant porosity for wire screen regenerators. The symbols on each line represent the screen mesh size at that point.

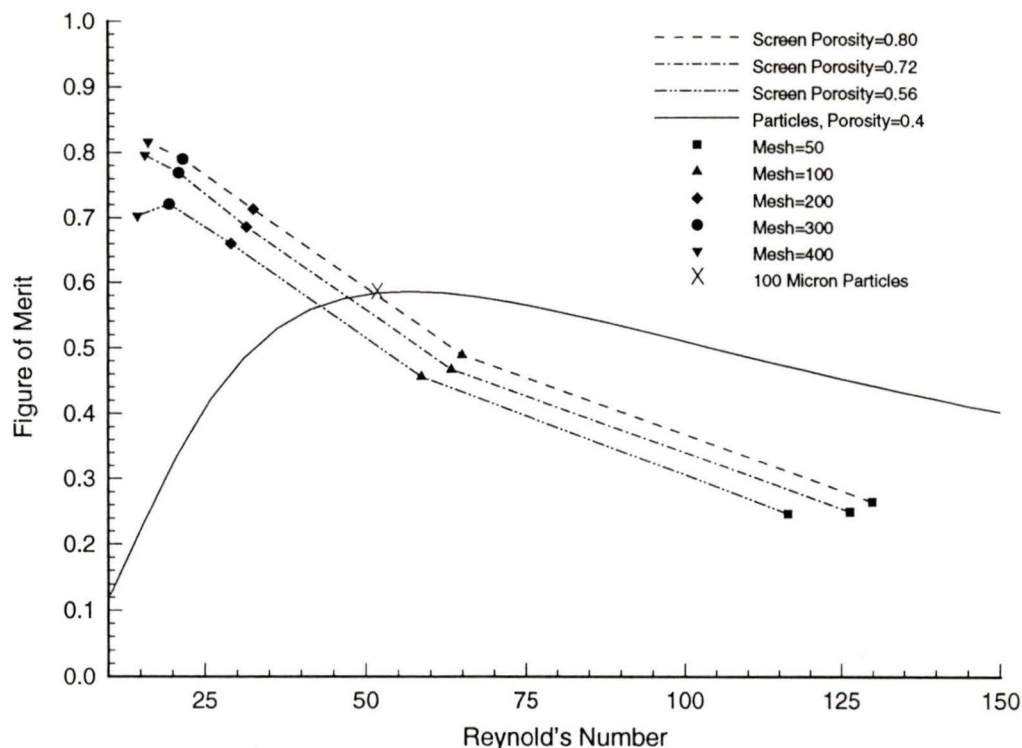


Figure 5.1.3a: FOM of particle and wire screen regenerator geometries for prototype AMRR flow conditions.

The wire diameters in the screens were varied to get the different porosities. These curves cover a 50 to 400 screen mesh range while incorporating wires with diameters ranging anywhere from 15 to 150 μm . The packed particle beds represented include particle sizes from 20 to 300 μm . The 100 μm packed particle bed performance is marked on the particle curve. Figure 5.1.3a yields interesting results. With 150 mesh wire screens having the porosities indicated, the screen performance will be about the same as 100 μm particles. Any higher meshes will result in a significant improvement in performance. For the operating conditions and ranges analyzed, increasing the screen porosity also resulted in higher FOMs. Again, in light of this analysis, particles were still chosen because of ease and low cost of manufacture.

However, because of the high potential of magnetic screen regenerators, rare earth wire screen manufacturing research was initiated (see section 5.3).

5.2 Manufacture of Particles From Magnetic Materials

It proved difficult to find manufacturing techniques to produce 100 μm diameter particles and 150-25 diameter μm wire from rare earth materials at a reasonable cost. Heavy rare earth particles have already been produced by various companies but the cost is unacceptably high, and no companies contacted had produced rare earth fine wire. Accordingly, CFS contracted several companies across North America to produce these regenerator media.

5.2.1 Spherical Particles

Atomization processes are necessary to produce spherical particles in the 100 μm range. The atomization method is defined as the reduction of a liquid into a fine spray. To ensure minimal contamination, all atomization processes must occur in inert environments. Two atomization methods were investigated: gas atomization, and centrifugal atomization.

5.2.1.1 Gas Atomization

Gas atomization for the production of the rare earth material particles was the first technology considered. In this process, liquid metal is poured into a reservoir (a tundish) which supplies a uniform and controlled flow of molten metal to the nozzle. The nozzle controls the shape and size of the metal stream which is then disintegrated as it passes through directed, high velocity atomizing gas streams (see Figure 5.2.1.1a) [98]. This atomization technique is used extensively in the production of metal powders.

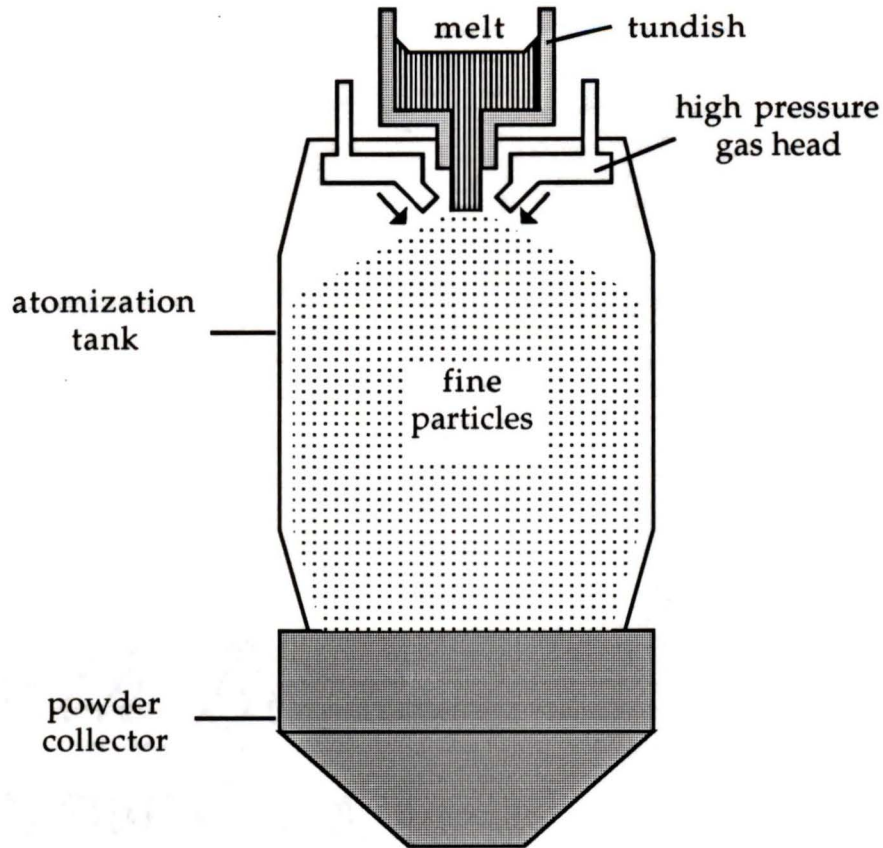


Figure 5.2.1.1a: Schematic of gas atomization apparatus

The particle size and shape is a function of the liquid surface tension, gas jet velocity and nozzle size, metal stream, cooling rates, and others. In general, gas atomization produces sphere-like particles with several smaller satellites in a log-normal distribution (when atomized at a constant pressure). In other words, the particle size distributions form nearly straight lines when plotted on a log-probability paper [99]. This means that the yield in a particular particle diameter range is unacceptably low (about 10 to 15% for 80 to 120 microns). Also, all gas atomization companies contacted were reluctant to try heavy rare earth metal in their process. Concerns ranged from complete unfamiliarity with the lanthanide metals to that of excessively small particles

spontaneously combusting.

5.2.1.2 Centrifugal Atomization

Centrifugal atomization uses centrifugal force to cause molten metal to disintegrate into droplets. There are two kinds of centrifugal atomization: single stage and two stage. In a single stage process, the material is melted and atomized in one step. In the two stage process, the material is melted and then atomized by the melt coming in contact with an imposed centrifugal force. Table 5.2.1.2a shows common centrifugal atomization processes [100].

Table 5.2.1.2a: Common centrifugal atomization processes for the production of metal powders.

Type of Atomization	Process*	Melting	Atomization
one-step	rotating electrode (REP)	consumable electrode/electric arc	electron rotation
	plasma rotating electrode (PREP)	consumable electrode/plasma arc	electron rotation
	laser rotating electrode (LREP)	consumable electrode/laser beam	electron rotation
two-step	rapid solidification rate (RSR)	crucible/induction melting	metal poured from crucible onto ceramic rotating disk
	consumable electrode/electric arc (CSC)	consumable electrode/electric arc	electrode drip-melted into water-cooled rotating cup
	consumable electrode/electron beam (EBRD)	consumable electrode/electron beam	electrode drip-melted into water-cooled rotating cup

Centrifugal atomization techniques can produce particles with a significant yield in the desired particle diameter range (30 to 50% for particles with diameters of 100 ± 20 microns). The particle diameter is determined by the balance between the centrifugal force inducing atomization and the surface

tension force of the liquid resisting disintegration. The centrifugal force is given by:

$$F_c = (\rho \pi d_{\text{drop}}^3 / 6) (\omega^2 D_{\text{at}} / 2) \quad (5.7)$$

where d is the droplet diameter, D is the atomizer diameter, and ω is the angular velocity of the atomizer. The surface tension force is given by:

$$F_{\text{st}} = \gamma \pi d_{\text{part}} \quad (5.8)$$

where γ is the surface tension of the liquid. When $F_c = F_{\text{st}}$, then the diameter of the particle is:

$$d_{\text{part}} = 3.46 (1/\omega) \sqrt{1/D_{\text{at}}} \sqrt{\gamma/\rho} \quad (5.9)$$

During the atomization process, all variables are fixed and the yield in a particular size distribution should be very high in the ideal case. In fact, the particle diameter could be controlled by changing only the frequency of the atomizer. In actual practice, the material homogeneity is never perfect and the yield is less than expected.

CFS worked closely with the material preparation department at AMES Laboratories in AMES, Iowa to investigate the possibility of two-step rapid solidification rate (RSR) centrifugal atomization. This process involves melting the material in a crucible with an induction furnace and then using positive pressure to squeeze the melt through an opening and down onto a rapidly spinning ceramic disk. The melt is atomized when it strikes the spinning disk and the particles are flung into a cooling stream of inert gas or a

rotating oil quench bath (see Figure 5.2.1.2a [101]).

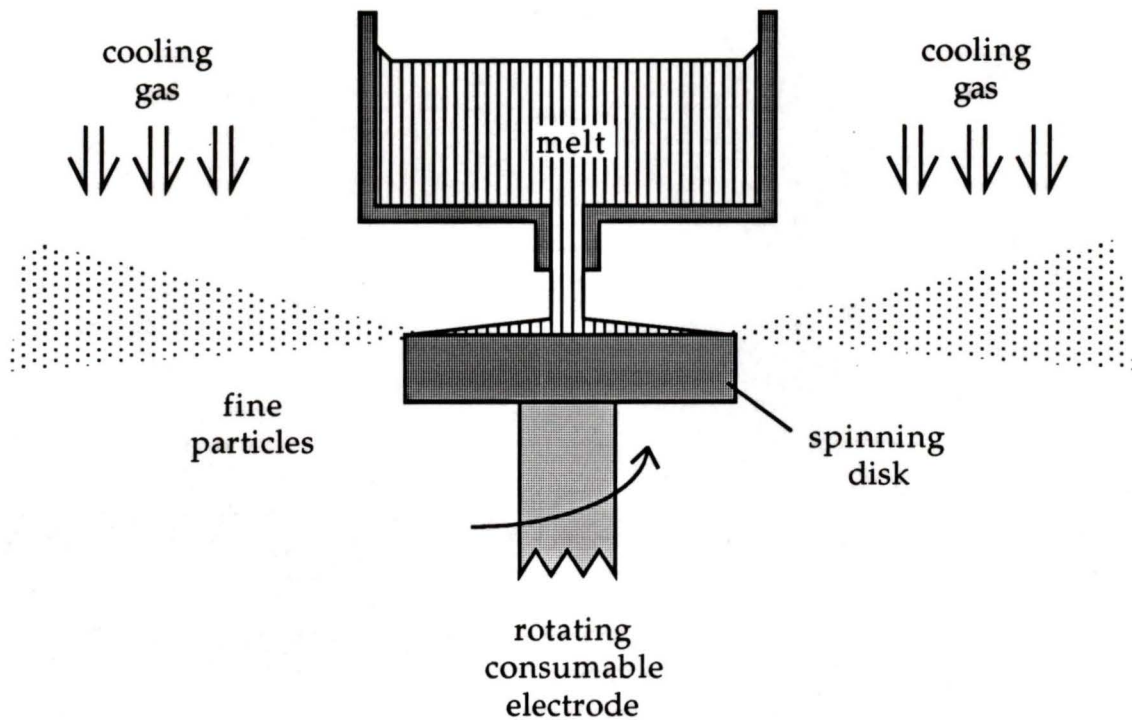


Figure 5.2.1.2a: Two-step RSR atomization process.

Unfortunately, the AMES apparatus could not process the material in the several kilogram range without extensive labour costs [102]. Also, there was a significant problem with the deterioration of the ceramic atomizing disk with high melting point rare earth materials. Other companies who use two-step atomization processes, such as Pratt & Whitney and Toshiba, charged excessive rates for rare earth particle production.

One-step atomization processes were also closely investigated. One-step processes melt and atomize materials in a single step and can achieve as good yields and sphericity as two-step centrifugal processes. However, atomization of alloyed materials with soft melting points using this process can cause the

production of non-homogenous powders. There is no opportunity for superheating as there is in two-step processes to completely melt the alloy and circumvent this problem. Nuclear Metals Inc. is a company that patented and specializes in one-step rotating electrode process atomization. Figure 5.2.1.2b shows a schematic of the REP single stage atomization [103].

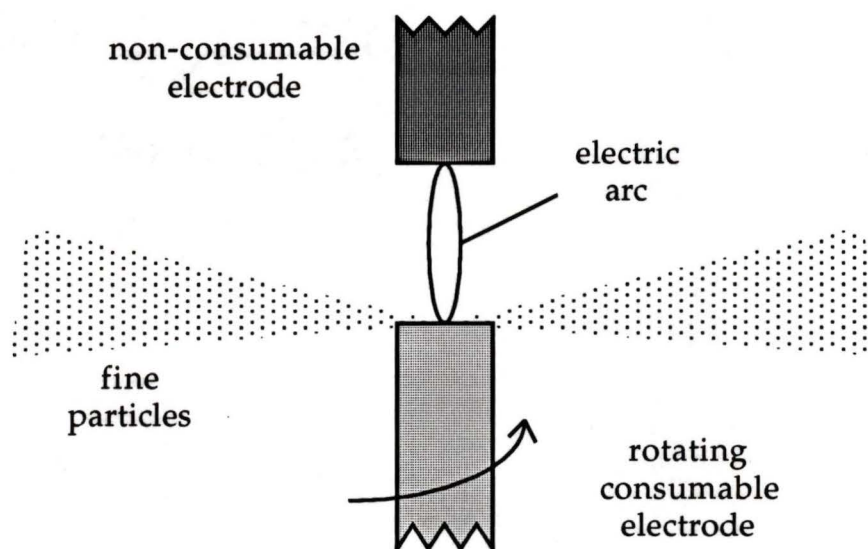


Figure 5.2.1.2b: Single-step REP atomization process.

Nuclear Metals Inc. had never atomized heavy rare earth metals and was willing to try to atomize dysprosium metal as a test (they have worked with neodymium) using their plasma rotating electron method. CFS requested two separate runs with one centred at 100 microns and the other at 300 microns. The acceptable range for each was 125-75 microns and 350-250 microns. Figure 5.2.1.2c shows a photograph of Nuclear Metals' PREP device [104].

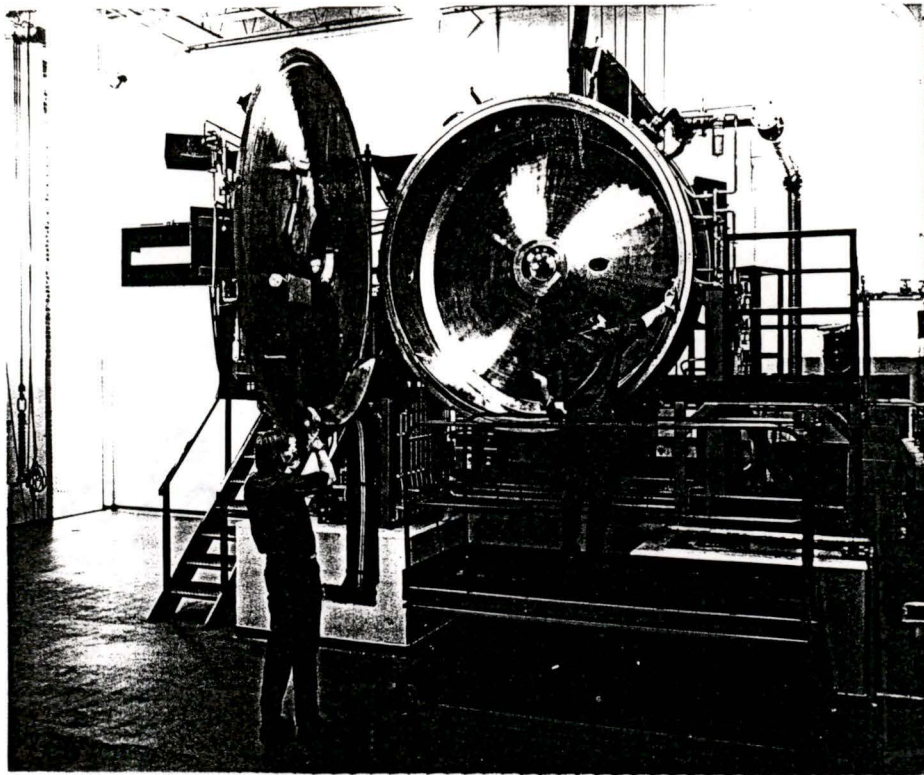


Figure 5.2.1.2c: Nuclear Metals REP and PREP apparatus.

Table 5.2.1.2b shows the particles distribution and weights produced by Nuclear Metals from two Dy electrodes with a total mass of 14.4 kgs.

Table 5.2.1.2b: Particle distribution and masses of Dy PREP trial run.

Particle Size Range (mesh (microns))	Total Mass (kg)
+ 45 (+ 365)	0.82
45 - 60 (365 - 250)	1.88
60 - 120 (250 - 125)	2.49
120 - 200 (125 - 75)	2.26
200 - (75 -)	0.71
sweepings	0.45

For the target ranges, the particles produced had an average yield of 48%. When the electrode stub-ends (material clamped in the chuck) are factored in, the total average yield is 29%. This is still double the yield that could be expected from a standard industrial gas atomization process. Figure 5.2.1.2d shows a scanned electron micrograph (SEM) of the yield 80-120 micron particles. The particles are of high quality, are solid throughout and have minimal satelliting.

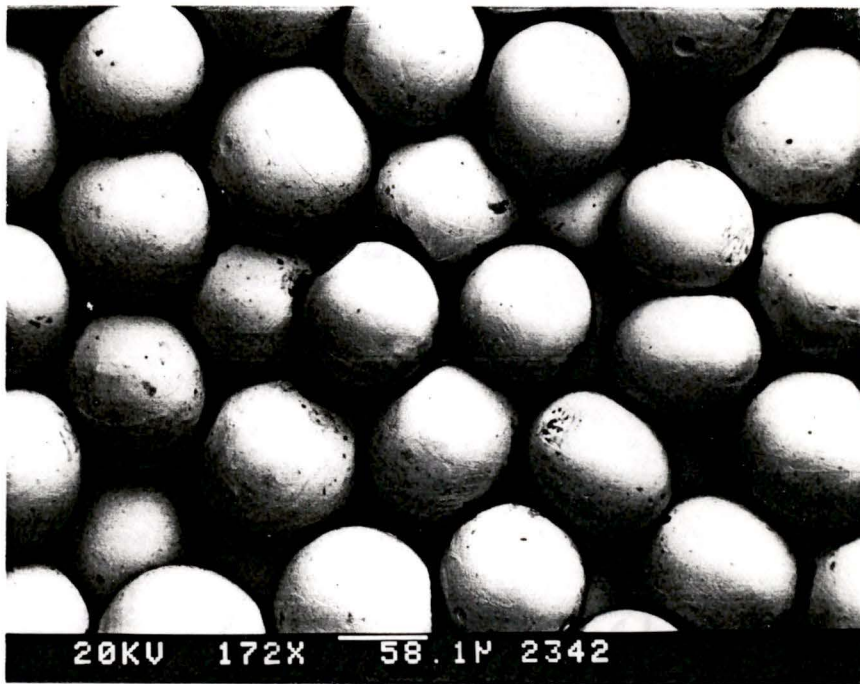


Figure 5.2.1.2d: SEM of ~100 micron dysprosium particles produced using single-step REP atomization process.

There is still some concern about the homogeneity of rare earth alloy particles using this technique but it has so far produced acceptable product at a reasonable cost. The cost for atomization of about 4 kgs of yield particles (based on a 30% yield rate) was US\$5000. This was considerably less than the other companies using two-step centrifugal atomization methods.

5.2.2 Irregular-shaped Particles

Spherical particles used as packed particle regenerator media are excellent for many reasons. There is only point contact between the particles which helps reduce longitudinal conduction and eddy current heating. Also, the bed density and settling variables are more closely controlled. However, as outlined above, the manufacture of spherical particles is still rather expensive. An interesting alternative is irregular-shaped or crushed particle beds. Several hundreds of grams of ~100 micron equivalent diameter crushed dysprosium particles were made in CFS labs. These particles were made by turning a dysprosium bar on a lathe into wire ribbons approximately 100 by 100 microns. These ribbons work hardened during the turning process and were then crushed manually in a mortar and pestle. Liquid nitrogen was used to lower the dysprosium below its ductile to brittle transformation temperature to facilitate the crushing process. Several problems were recorded:

- when turning the dysprosium bar, it was difficult to set the feed and rotating frequency to get a square 100 micron ribbon (normal dial shop lathe was used),
- an inert gas jet focused on the work piece was required during the turning operation to prevent the dysprosium from combusting,
- the manual crushing method was time consuming and labour intensive and often produced shards of high aspect ratios that made it through the sieving process.

High quality ribbons cut on an NC machine and an inert ball mill (or other reducing device) are required to mass produce target crush particles using this method. This method was not tried.

5.3 Manufacture of Wire From Magnetic Materials

To get wire screens of with the high heat transfer coefficients and N_{tu} necessary to get highly effective regenerators, the screens need to be of a high mesh size (typically 100 mesh or higher). This means that the magnetic materials need to be drawn to under 100 micron diameters (for a standard 400 mesh screen, the wire diameter is about 25 microns). The heavy rare earth materials had never been drawn to such small diameters and several wire manufacturing companies even insisted that it could not be done because of the physical properties of the material. CFS formed a three way collaboration among CFS, AMES [105] and Supercon Inc. [106]. Supercon is a company that specializes in the manufacture of superconducting wire. AMES served primarily as a material technical advisor.

5.3.1 Experimental Method and Results

Figure 5.3.1a shows a schematic of the billet used to set up the rare earth material for the drawing effort [107]. The dysprosium core, the niobium diffusion barrier, and the copper can were hot extruded through the billet and co-deformed as expected. The copper can around the dysprosium is essential to prevent oxidation of the rare earth metal as periodic annealing heat treatments are performed to recover the material's ductility during the drawing process. The niobium shield acts as a barrier to prevent diffusion between the dysprosium and the copper during annealing process. After the composite material was hot extruded, it was annealed and made ready for the die drawing processes.

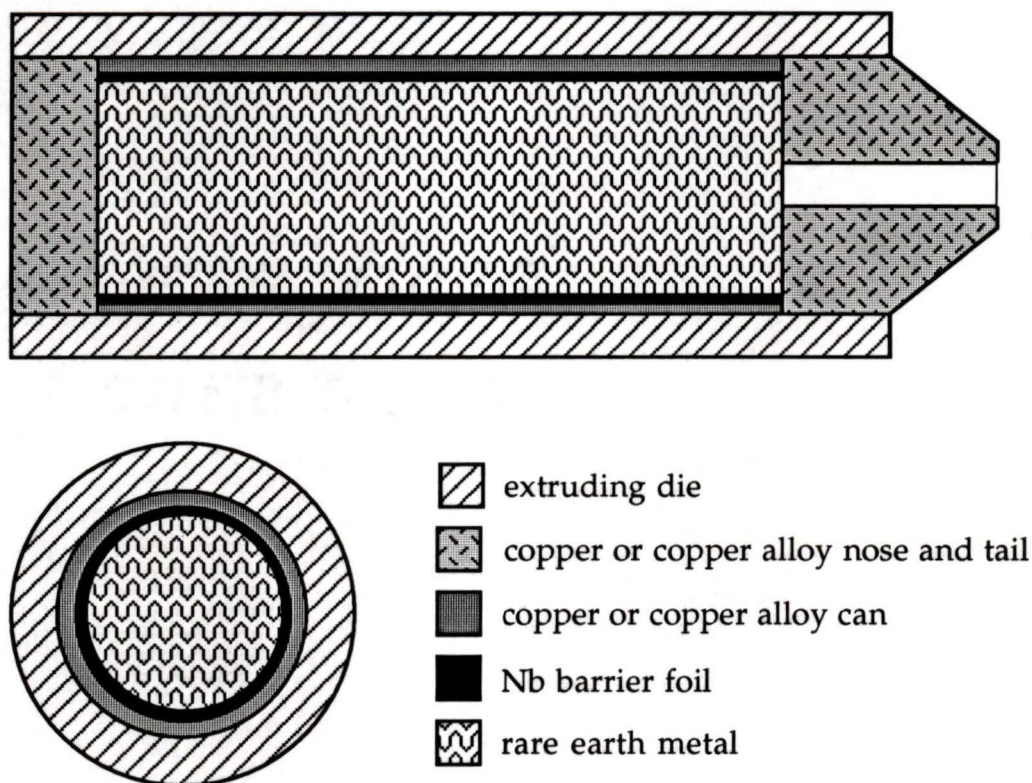


Figure 5.3.1a: Schematic of billet used to hot extrude dysprosium.

Supercon performed the drawing process on a trial and error basis until it discovered the optimum annealing schedule that allowed the material to be drawn to fine diameters with minimal breakage. Out of 750 grams of dysprosium starting material, Table 5.3.1a shows the wire samples delivered.

Table 5.3.1a: Diameter, length and description of wire samples delivered.

Wire Diameter (microns)	Sample Length (feet)	Description
250	misc.	Dy + Nb etched from 325 μm composite
332	650	As-drawn composite (Dy core of 250 μm)
208	2780	As-drawn composite (Dy core of 150 μm)
114	~20	As-drawn composite (Dy core of 98 μm)
98	~5	Dy + Nb etched from 114 μm composite
76	~20	As-drawn composite (Dy core of 66 μm)

Figure 5.3.1b shows a micrograph of the cross section of the composite material at a diameter of 365 microns [108].

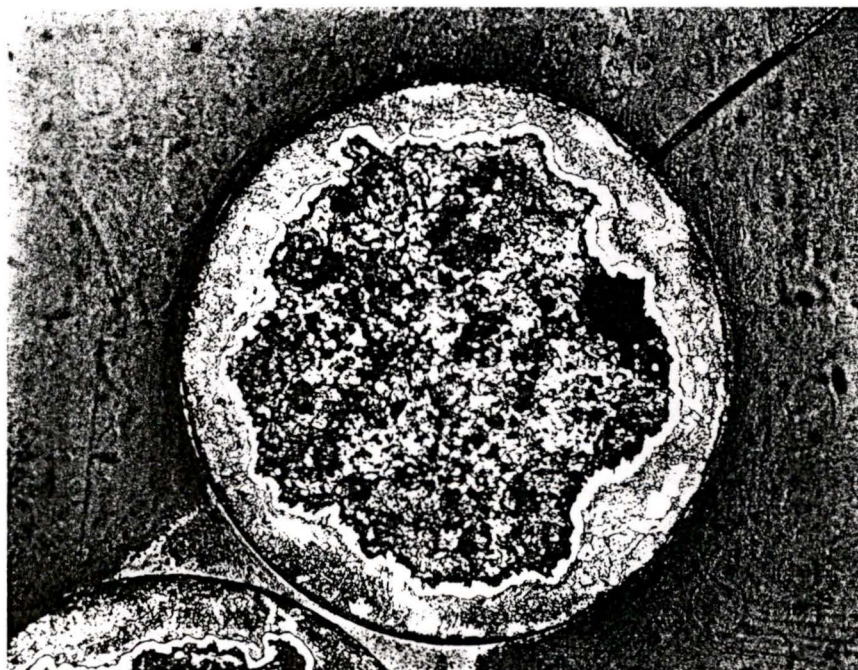


Figure 5.3.1b: 200X micrograph of cross section of the material composite showing the Dy core, Nb barrier, and the Cu jacket.

The irregular shape of the Dy core and the Nb barrier is the result of drawing the as-cast dysprosium. The result was that the barrier was stretched very thin in some sections (sub-micron level) and failed when the copper jacket was etched off. In most cases, etching the copper off will be necessary to prevent dilution of the magnetic material in the regenerator. Ideally, when the copper is removed, the Nb serves to protect the Dy from the etching agent (nitric acid and water) and also acts as a oxidation barrier for the finished wire. The irregular cross section can be prevented by treating the as-cast dysprosium to break down the grain structure size before the drawing process commences. The conclusions gathered as a result of this drawing trial are as follows [109].

- commercial grade Dy has sufficient ductility and purity to allow fabrication into fine, long length wires;
- the billet processing technique completely protects the Dy from any impurity contamination during thermal and mechanical processing; the final Dy wire has the same chemistry and properties as the billet starting material; the ductility of the Dy does not degrade during the multiple anneals required for processing into fine wire; the Nb barrier is not magnetic and provides long term protection of the rare earth metal core from oxidation and corrosion;
- the Dy starting material should be treated to remove the as-cast microstructure;
- the Nb barrier fails completely at approximately 1 micron in average thickness, and in the event of an irregular Dy core shape, the Nb barrier develops thin spots at larger Nb thicknesses which fail locally upon etching, and
- the Nb barrier thickness at the etching stage should be ~2 microns or more, and the volume % of Nb barrier in the final etched wire will be a function of the wire diameter.

In general, the Dy drawing experiment was very successful. It has proved that these heavy rare earth materials can be drawn down to fine wire diameters. Smaller diameters (on order of 50-25 microns) can probably be achieved if the material's as-cast grain structure is treated and the Nb barrier is sized to prevent Dy disintegration upon final etching.

5.3.2 Wire Screens

Once the magnetic materials are drawn to fine wires, they can be woven into wire screens. The largest material constraint when weaving screens is caused by the crimping process. When screens are woven, the wire is crimped to give the screen strength and integrity. The higher the mesh, the more severe the crimp. The wire material must be ductile enough to undergo the crimping process without breaking. Properly annealed heavy rare earth wire should possess sufficient ductility. Most high mesh (100+) wire screens are not fabricated in North America. Much of it is imported from Asia and Europe. There are a few custom screen weavers in the United States, but the set-up charges for using different materials and creating high mesh products run from \$US5,000-10,000. Consequently, the wires have not yet been woven into screens.

The wires could also be used to create cross rod and wire matt geometries. These geometries were considered in section 5.1.2.

5.4 Manufacturing Cost Considerations in Selecting Regenerator Geometries

From the discussion above, the cost and complexity considerations when selecting regenerator geometries are considerable. If a product is going to be economically viable, it must lend itself to large-scale production at minimal

cost. In the case of the AMRR, the magnetic material alone is already a significant cost. The cost to convert that material to a highly effective regenerator geometry should be reduced as much as possible. This was one of the main driving forces leading CFS to choose particle and screens as initial regenerator geometries to study. Both geometries are conceptually simple and are relatively easy to fabricate.

Based on the performance analysis and the cost factors, CFS choose particles as its first regenerator geometry to use in the prototype AMRR.

Chapter 6

Testing Regenerator Geometries

6.1 Identifying Parameters to Test

Ideally, the fabricated active magnetic regenerator beds should be tested in an AMRR test device where all of the fluid flow, magnetic, thermodynamic and structural aspects can be compared. Unfortunately, CFS does not have a magnetic test apparatus yet available. This means that the regenerator beds cannot be tested under applied magnetic field conditions. The issue is to choose important regenerator properties for that can be tested without an AMRR device. These parameters should be critical to the AMRR operation but at the same time remain relatively uncharacterized. Two important of such variables are overall longitudinal conduction (including eddy diffusivity effects), and the regenerator eddy current generation. Packed particle beds were the only regenerator geometry tested. CFS is building a pulse-tube refrigerator regenerator testing device [110]. This apparatus will be useful for testing regenerators that will be used in a pressure pulse system, but it is unclear whether it will be able to adequately simulate AMRR flow conditions. For each test, an apparatus was designed and built that will provide specific data to assess the parameter for AMRR operation.

6.2 Regenerator Eddy Current Generation

Eddy current heating in the AMRR will be a function of the magnitude of the applied field, the projected surface area of the regenerator material normal to the magnetic field lines, the cycle frequency, and the resistivity of the material. All variables are known except for the bulk resistivity of the regenerator bed itself. Calculations have shown that to get the parasitic heating caused by eddy current generation to a negligible value, the regenerator resistivity should be greater than the mΩcm range [111].

6.2.1 Methodology and Test Apparatus

To test the regenerator beds for bulk resistivity, a current is passed through the bed, the voltage drop recorded and the resistance calculated using $R=V/I$. The resistivity can then be determined by:

$$\kappa_{\text{bed}} = \frac{RA_{\text{contact}}}{L_{\text{bed}}} \quad (6.1)$$

where κ_{bed} is the regenerator resistivity, A_{contact} is the contact area between layers of particles, and L_{bed} is the regenerator bed test length. The particle regenerators were tested by setting up a dielectric particle container in which the rotating electrode manufactured dysprosium particles were loaded to a predetermined bed length of one cm. A well cleaned copper plate was placed on both sides of the particle bed to conduct the current to the ohmmeter. The particle bed was loaded incrementally to a maximum pressure of about 20 MPa (3000 psi) by an Ingstrom material testing machine. At each load setting, the bed deformation was measured to account for the true bed length and the regenerator resistance was recorded. Figure 6.2.1a shows a schematic of the test apparatus that was built and used to do the resistance measurements.

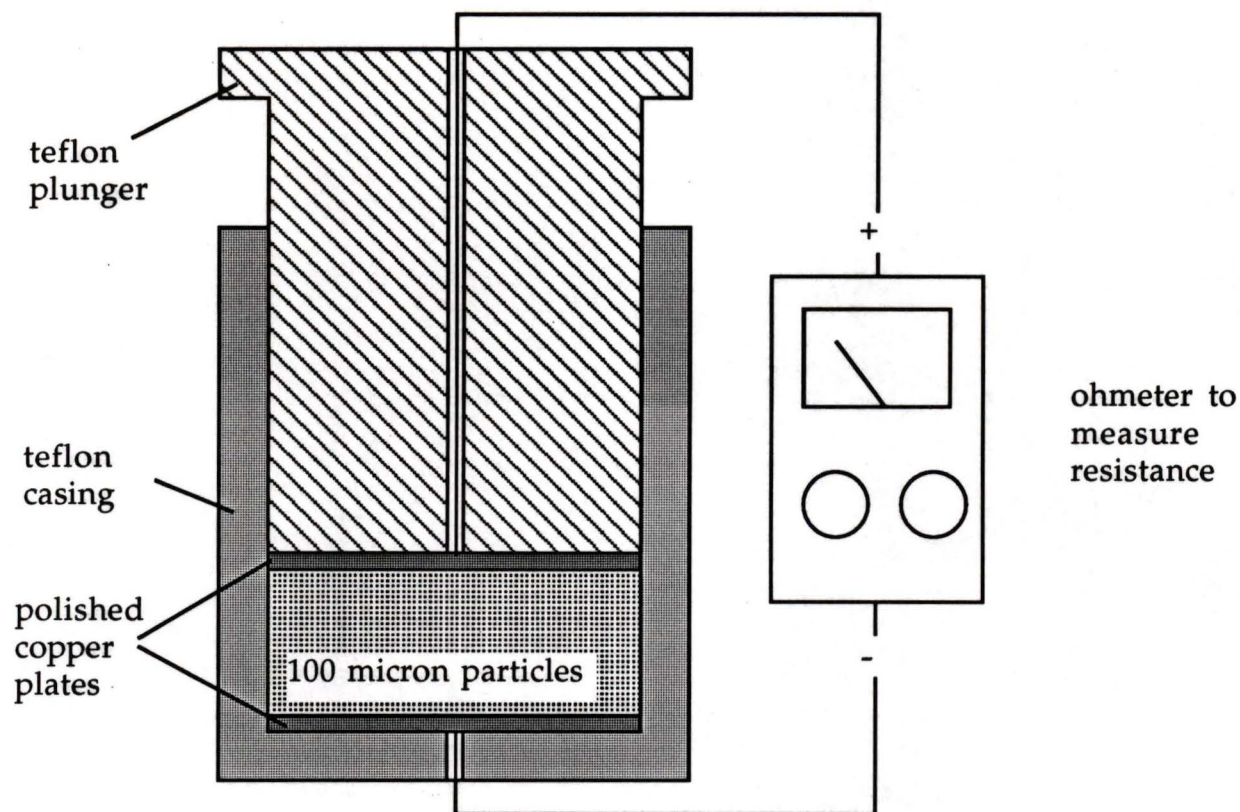


Figure 6.2.1a: Schematic of regenerator resistance testing device.

6.2.3 Results

Figure 6.2.3a shows a graph of the resistivity of the tested particle bed versus the applied copper end-plate pressure.

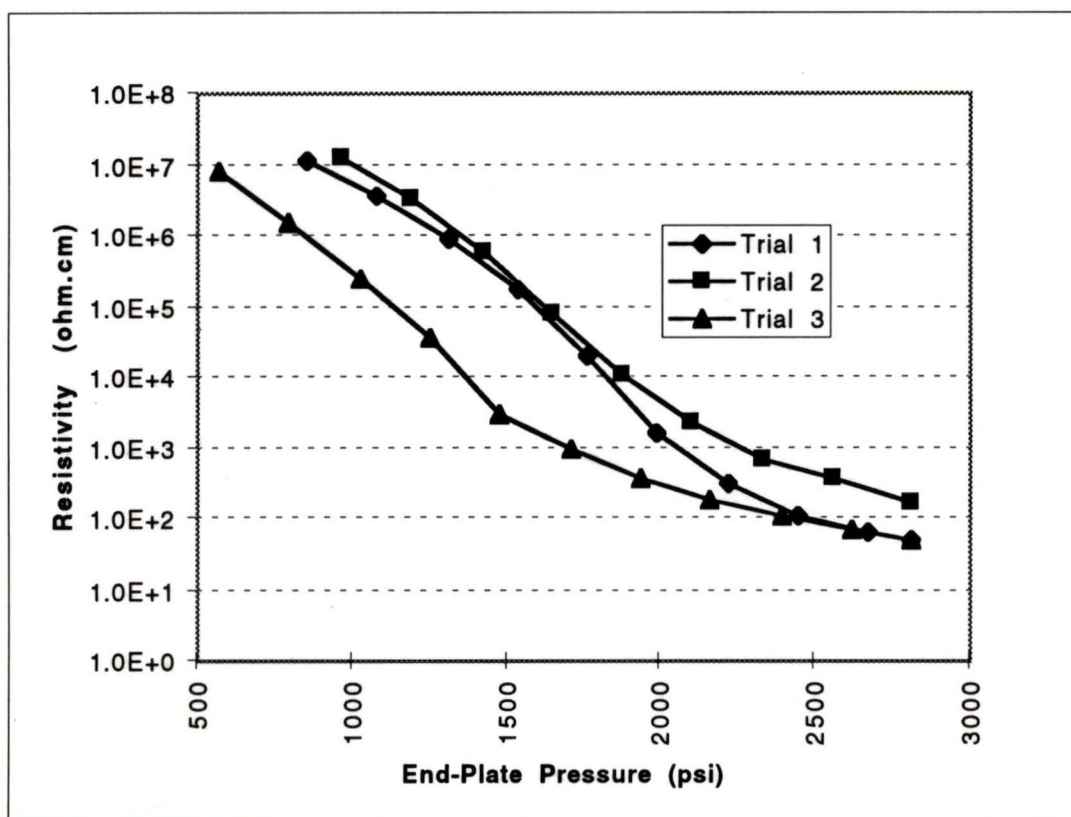


Figure 6.2.3a: Resistivity vs. plate pressure for 100 micron diameter dysprosium particle bed.

The graph shows the results for three different trials. In all cases the particle charge consisted of 100 micron diameter dysprosium particles with a bed length of one centimetre. The graph results show a decrease in the bed resistivity with applied pressure. This is expected because the contact area between the adjacent layers of particles is increased with increasing load. At higher pressures, the resistivity change with pressure begins to decrease. This is caused by the larger loads required to deform the particles when the contact surface area is greater. When the load is first applied to the end-plate, the pressure on the particles is extremely high because of the point contact area. This results in large contact area changes for relatively small load increments. As the overall contact area increases, the incremental pressure required to increase this contact area by the same amount becomes greater.

Solid dysprosium has a measured resistivity of about $91 \mu\Omega\text{cm}$. At the highest pressures applied during the tests, the 100 micron diameter dysprosium particles showed a resistivity greater than $10 \Omega\text{cm}$. This is four orders of magnitude greater than the $\text{m}\Omega\text{cm}$ range identified as the lower limit of resistivity before eddy current generation causes a significant parasitic loss in the AMRR. In the prototype device, the plate pressure will be a nominal 1.1 MPa (150 psi) and the bed length will be approximately 5 cms. This suggests that the actual resistivity of the particles will be several orders of magnitude greater than the highest values obtained during the testing ($\sim 10^7 \Omega\text{cm}$). The negligible electrical conductance of the dysprosium particle beds arises from the point contact (reduced contact area) and the insulating effect of the oxide layer that forms around the particles. In any case, the experimental data indicates that parasitic losses due to eddy current generation in the regenerator bed will be negligible.

6.3 Effective Longitudinal Conductivity Tests

Longitudinal conduction along the regenerator bed can occur via three mechanisms: fluid to fluid conduction, solid conduction, and eddy diffusivity (excluding the regenerator shell). As mentioned previously, eddy diffusivity is actually a convection processes that occurs when the fluid forms small recirculation eddies. From the above mentioned mechanisms, eddy diffusion is the least characterized and shows the largest scatter in the literature. A test apparatus has been manufactured that will enable the determination of the effective N_{tu} of a given regenerator bed under AMRR flow operating conditions. The N_{tu} is estimated graphically and will include the heat transfer coefficient effects as well as all longitudinal conduction effects. Because the correlations for the heat transfer coefficient for packed particle

beds have been well explored and generally accepted, the effective N_{tu} measurements from the test device will allow the overall effective longitudinal conduction values to be backed out.

The test device was fabricated, but because of time constraints, the actual N_{tu} experiments were not completed.

6.3.1 Methodology and Test Apparatus

To evaluate the effective N_{tu} of a regenerator bed, the heat transfer fluid of a constant temperature (different than the material) is passed through the bed and the regenerator bed's transient temperature response is recorded. This data can be collected and displayed in a temperature versus time curve for specific points along the regenerator bed. Figure 6.3.1a shows an example of such curves for a high temperature blow.

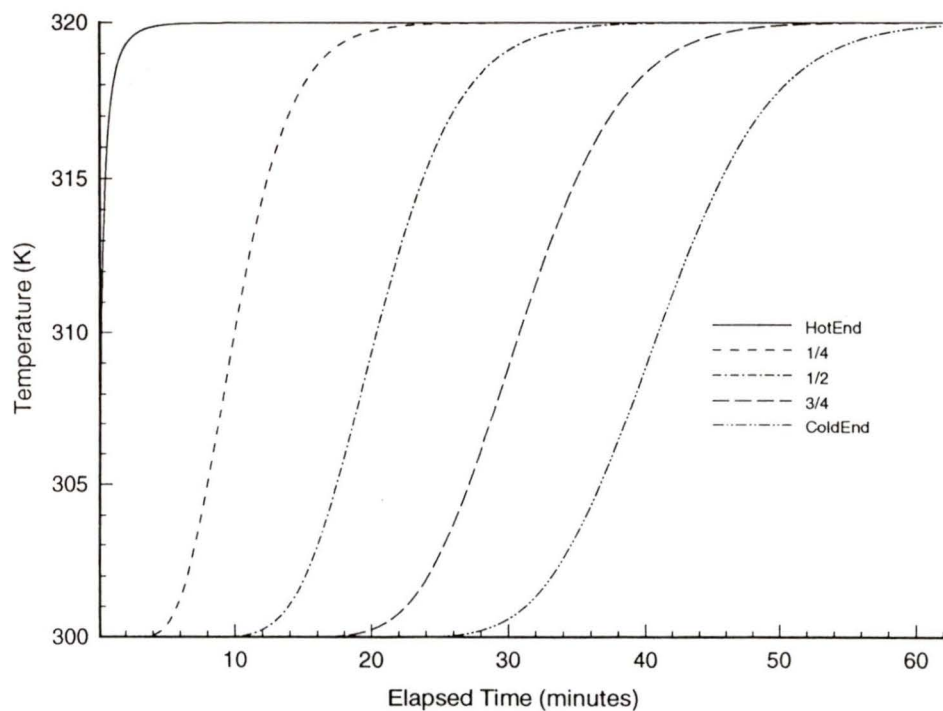


Figure 6.3.1a: Example of possible temperature vs. time profiles for selected points along a test regenerator bed.

The bed's N_{tu} can be estimated by the slope of the curves in the figure. The magnitude the slope indicates the regenerator's ability to provide the heat transfer fluid at the required temperature for a given amount of time before the heat exchanger's capacity is reached. For the example in Figure 6.3.1a, if the slope of the profile is very steep, the regenerator will provide a 300 K exit temperature for a long period of time. If, on the other hand, the slope is gradual, the regenerative function of the bed is lost very quickly.

Figure 6.3.1b shows a schematic of the test device that was built to experimentally obtain the temperature versus time profiles for any given regenerator device.

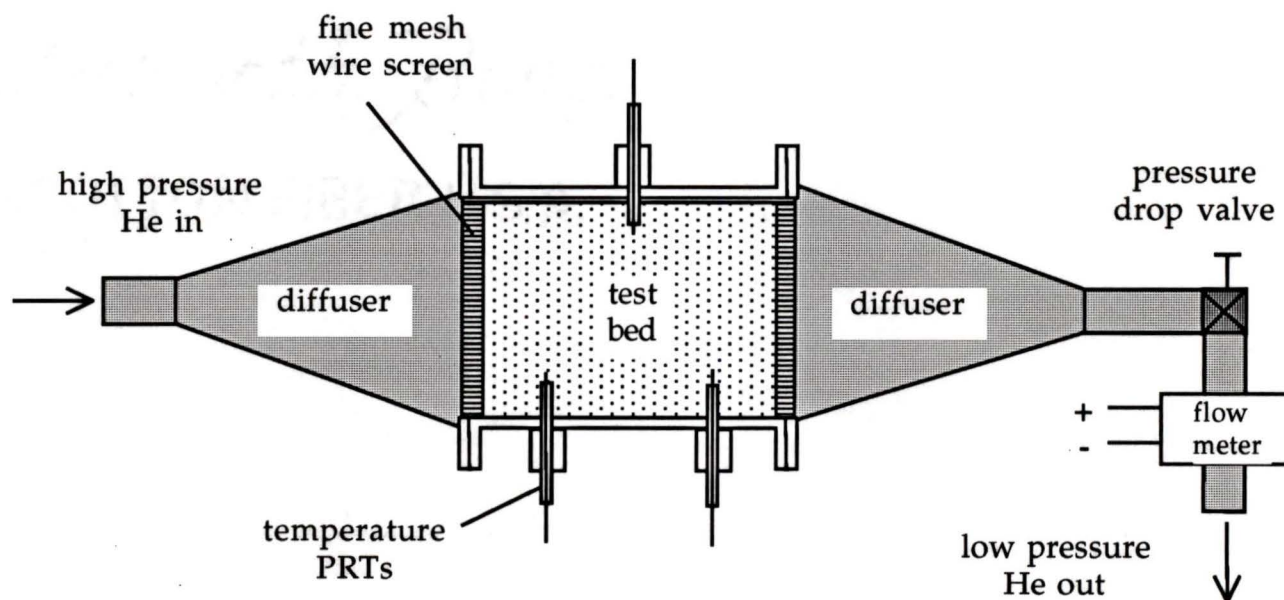


Figure 6.3.1b: Schematic of device used to obtain temperature/time profiles for regenerator beds.

Because the purpose of the device is to evaluate operating conditions of the actual AMRR prototype, the test device was designed to take 50 bar helium gas at the mass flow rate of 0.096 kg/s. The walls of the regenerator bed

container are thin wall titanium to reduce wall conduction effects. PRTs will record the temperatures of the gas entering and exiting the device as well as at three point along the bed as a function of time (there will also be an opportunity to measure pressure drop by using a differential pressure transducers). The mass flow rate of the gas will be measured downstream after it is throttled to a lower pressure.

6.3.2 Computer Simulation

The temperature versus time profiles obtained from the test device do not provide enough information on their own to get numerical estimates of the effective longitudinal conduction. These profiles are a function of both the heat transfer coefficient and conduction effects. To get a reasonable estimate, a one dimensional, transient computer simulation program has been developed that will be used to benchmark the results from the experiments (the code is also found in Appendix D). The simulation program consists of a finite difference model that produces temperature versus time profiles exactly like those obtained from the test device (Figure 6.3.1a was generated using this simulation program) [112]. In the program, the heat transfer coefficient is evaluated using accepted correlations as well as the solid to solid and fluid to fluid longitudinal conduction. The value for the eddy diffusivity convection term is left as a variable. This variable is manipulated until the resulting temperature versus time profile matches the one obtained by experimental means. This procedure will give a rough estimate of the eddy diffusivity effects, and consequently, of the overall effective N_{tu} of the tested regenerator bed.

At this point, the simulation program has been written and the test device manufactured. No experimental tests have been performed.

Chapter 7

Conclusions and Future Work

7.1 Conclusions

At the heart of an active magnetic regenerative refrigerator is the regenerator itself. This crucial piece of equipment provides the means for spanning the large temperatures in the device and also provides the thermodynamic power required to achieve cooling powers at low temperatures. The regenerator is composed of magnetic materials (refrigerants). The correct selection of the materials is essential to the thermodynamic performance of the AMRR. In addition, these materials must be manufactured into a form that provides excellent passive and active heat transfer while minimizing entropy production. With this in mind, the following conclusions can be made.

- An AMRR is a complex thermodynamic system that is composed of a circulating heat transport fluid and magnetic material subsystem that are inordinately inter-linked.
- The thermodynamic criteria for the selection of magnetic refrigerants for an AMRR are: (1) the material must have the required adiabatic temperature changes at the hot and cold boundaries (in a given applied field) to allow the fluid to pick up the specified cooling load and to deposit

that load, plus the net power and any entropy generated, to the environment, and (2) the material must be able to transfer the required amount of net power to the heat transfer fluid to operate the overall cycle. In the case of the AMRR prototype, $\Delta T_{ad,c} = 3.5$ K, $\Delta T_{ad,h} = 8.2$ K and the net power is 2245 W.

- The magnetic material in the AMRR functions as the passive regenerative material as well as the working refrigerants and the material mass must be selected to reflect this.
- For the large temperature span required in the prototype (110 K to 240 K), several magnetic materials need to be layered in the regenerator to meet the thermodynamic criteria as well as to allow the AMRR to self start. The regenerator materials chosen to be layered in the prototype are $Gd_{.535}Dy_{.465}$, $Gd_{.360}Dy_{.640}$, $Gd_{.184}Dy_{.816}$, and elemental Dy.
- For heavy rare earth materials, a good AMRR selection screening property is the material's magnetic entropy change per unit volume as a function of field and temperature (leads to ΔT_{ad} vs T profiles). Heavy rare earth metals and alloys thereof exhibit high $\Delta s_m/m^3$ properties in the prototype's operational temperature range and also have good formability characteristics.
- The rotating electrode centrifugal atomization method produces high quality spherical 100 μm dysprosium particles with an average yield of 29% (± 20 μm). This method should be extendable to other rare earth elements and intra-rare earth alloys.

- Irregular shaped rare earth particles can be inexpensively manufactured by crushing work hardened cuttings from a lathe. This method is time consuming and requires automation to be feasible for large-scale production. This method may have promise for very low cost particle production.
- Fine dysprosium wire can be drawn from commercial grade metal. The Dy core was drawn to a minimum of 66 μm and smaller diameters could be reached if the as-cast grain structure is broken down before the drawing process.
- An excellent AMRR regenerator configuration will have minimal fluid pressure drops, low longitudinal conduction, low eddy current generation, high heat transfer coefficient, low porosity, be structurally robust and easily manufacturable at low cost. Wire screen and packed particle bed geometries offer the best compromise among the conflicting design variables for the design conditions of the prototype AMRR.
- For the prototype application, certain wire screen regenerators have greater figures of merit than particle bed regenerators. In terms of manufacturability and cost, packed beds are currently more attractive.
- The total estimated entropy generated by the prototype's $\sim 100 \mu\text{m}$ particle regenerator is 5.96 W/K (excluding pressure drop losses) and the FOM is 36.6%
- The bulk resistivity of $\sim 100 \mu\text{m}$ heavy rare earth particles will be several orders of magnitude larger than the pure metals. In particular, Dy particles packed into a regenerator of the prototype's specifications, will exhibit a

bulk resistivity of at least 13 orders of magnitude greater than pure Dy metal. This will effectively make any entropy production by eddy currents insignificant.

7.2 Future Work

The work completed in this thesis essentially lays the groundwork for the development of magnetic refrigerants for an AMRR. Because of time and scope constraints, there remain several areas where additional research and testing are required to completely characterize good refrigerants. The following lists identifies areas that require further work.

- A detailed optimization analysis for minimum refrigerant mass requirements is needed to ensure that excess magnetic material is not being used and driving the magnet system costs higher. The active regenerator mass also requires in-depth analysis to get a more accurate value to facilitate this process.
- The prepared magnetic refrigerants require empirical testing to confirm their magnetic properties. Heat capacity, magnetization, and hysteresis behaviour as a function of applied field and temperature are required.
- There are several other identified magnetic materials that have good potential to become effective AMRR refrigerants in the temperature range of interest. These materials need to be completely analyzed and characterized to assess their suitability. Also, a complete search of the available magnetic materials including other rare earth alloys, intermetallics, amorphous materials, and nanocomposites needs to be continually performed to add new possible refrigerants to the list.

- The regenerator manufacturing methods for packed particle beds and wire screen regenerator geometries are incomplete. More research is required to determine the ultimate drawability of the rare earth materials into fine wires. Screen manufacture also needs to be performed. Particle production runs using the rotating electrode method have to be done on the chosen alloys and other manufacturing methods such as vacuum atomization can be looked at. Crushed particles hold promise for inexpensive particle production. Methods of producing large quantities need to be developed.
- Manufacturing methods for perforated plate and parallel plate regenerator geometries needs to be developed. Analysis shows that these geometries could have excellent regenerator characteristics for use in the AMRR.
- Complete regenerator testing in an active magnetic test device will be essential for each magnetic regenerator manufactured. The prototype AMRR will be used for this purpose and should be ready at the end of 1995. In the meantime, the regenerator's effective N_{tu} (including all longitudinal conduction effects) requires characterization in the passive test apparatus that has been designed, built, and introduced in this thesis.

The magnetic refrigerant development work has been passed on to a different research engineer/graduate student at CFS and the above identified areas will receive suitable attention.

Chapter 8

References

- 1 J. A. Barclay, J. de Grasse, H-H. Rogner, "Hydrogen for transportation; what can we learn from natural gas?" , presented at the 6th Canadian Hydrogen Workshop, Victoria, B. C., February 1994.
2. *The Clean Fuels Report*, J. E. Sinor Consultants Inc., 6, No. 4, Sept, 1994.
3. David G. Howell (Ed.), *The Future of Energy Gases*, U.S. Geological Survey Professional Paper 1570, Washington: U.S. Government Printing Office, (1993): 613.
4. *NGV News*, Pasha Publications, 3, No. 12, Dec. 1994.
5. *The Clean Fuels Report*, J. E. Sinor Consultants Inc., 6, No. 3, June 1994.
6. *The Clean Fuels Report*, 6, No. 3, *ibid*.
7. S-7 bill in Canadian senate.
8. *Cryofuel Systems Inc. Business Plan, Vol II*, CFS Inc., Federal Way, WA, 1995.
9. J. A. Barclay and F. C. Prenger Jr., "Magnetic refrigeration apparatus with heat pipes", US patent No. 4,642,994. 1987.
10. J. A. Barclay and S. Sarangi, "Selection of regenerator geometry for magnetic liquefaction", *Cryogenic Process Equipment*, 1984.
11. C. R. Cross, J. A. Barclay, A. J. DeGregoria, S. R. Jaeger, J. W. Johnson, "Optimal temperature - entropy curves for magnetic refrigeration",

Astronautics Technology Centre, Madison, WI.

12. J. L. Smith, Jr, Y. Iwasa and F. J. Cogswell, "Material and cycle considerations for regenerative magnetic refrigeration", *Advances in Cryogenic Engineering*, 35, (1990): 1157-1164.
13. T. Hashimoto, T. Numasawa, M. Shino, T. Okada "Magnetic refrigeration in the temperature range from 10 K to room temperature: the ferromagnetic refrigerants", *Cryogenics*, (November 1981): 647-653.
14. Private communication with Dr. Jeff Hall, Cryofuels Systems Group, August 1994.
15. A. H. Morrish, *The Principles of Magnetism*, New York: John Wiley & Sons, 1965.
16. A. S. Andreenko, K. P. Belov, S. A. Nikitin, and A. M. Tishin, "Magnetocaloric effects in rare earth magnetic materials", *Soviet Physics Usp.*, 32 (8), August 1989.
17. M. D. Kuz'min and A. M. Tishin, "Magnetocaloric effect Part 2: magnetocaloric effect in heavy rare earth metals and their alloys and application to magnetic refrigeration", Physics Dept., Moscow State University, 1992.
18. S. A. Nikitin, A. M. Tishin, P. I. Leontev "Magnetocaloric effect and refrigerant capacity of Tb-Dy alloys", *Phys. Stat. Sol.*, 113, (1989): K117.
19. T. Hashimoto, T. Numasawa, M. Shino, T. Okada, "Magnetic refrigeration in the temperature range from 10 K to room temperature: the ferromagnetic refrigerants", *ibid.*
20. T. Hashimoto and Takasu, "Recent progress in magnetic materials and their application", Proceedings of the 18th International Congress of Refrigeration, 1, (1991): 314-321.
21. K. A. Gschneidner, H. Takeya, J. O. Moorman, V. K. Percharsky, S. K. Malik, and C. B. Zimm, "New magnetic refrigeration materials for the liquefaction of hydrogen", CEC/ICMC, 1993.
22. J. A. Barclay and S. Sarangi, *ibid.*

23. C. B. Zimm, E. M. Ludeman, M. C. Severson, and T. A. Henning, "Materials for regenerative magnetic cooling spanning 20 K to 80 K", *Advances in Cryogenic Engineering*, 37, Part B, (1992): 883-890.
24. S. R. Schuricht, A. J. DeGregoria, and C. B. Zimm, "The effects of a layered bed on active magnetic regenerator performance", International Cryocooler Conference, 1992.
25. C. Carpetis, "An assessment of the efficiency and refrigeration power of magnetic refrigerators with ferromagnetic refrigerants", CEC/ICMC, 1993.
26. G. Green and J. Chafe, "A gadolinium-terbium active regenerator", *Advances in Cryogenic Engineering*, 35, (1990): 1165, 1174.
27. J. L. Smith and Y. Iwasa, "Material and cycle considerations for regenerative magnetic refrigeration", *Advances in Cryogenic Engineering*, 35, (1990): 1157-1164.
28. C. E. Reid, J. A. Barclay, J. L. Hall, and S. Sarangi, "Selection of magnetic materials for an active magnetic regenerative refrigerator", *Journal of Alloys and Compounds*, (1994): 366-371.
29. R. Asomoza, A. Fert, and R. Reich, "Gadolinium-heavy rare earth alloys: preparation, metallographic study and extraordinary hall effect", *Journal of the Less-Common Metals*, 90, (1983): 177-201.
30. Buehler Dialog: Microstructural Analysis Reference Manual, Buehler Ltd. Lake Bluff, IL.
31. A. S. Andreenko, K. P. Belov, S. A. Nikitin, and A. M. Tishin, *ibid.*
32. A. M. Tishin, "Magnetocaloric effect in strong magnetic fields", *Cryogenics*, 30, (1989): 127-135.
33. S. A. Nikitin, A. S. Andreyenko, A. M. Tishin, A. M. Arkharov, and A. A. Zherdev, "The magnetocaloric effect in rare earth alloys Gd-Ho and Gd-Er", *Fiz. Metal. Metalloved.*, 59, No. 2, (1985): 327-331.
34. *Landolt and Boernstein*, New Series III/19d1, Kawano and Achiwa, pp. 190ff.
35. Gschneidner and Eyring (Eds.), *Handbook on the Physics and Chemistry of Rare Earths*, 1, 1978.

36. T. E. W. Schumann and V. Voss , "Heat flow through granulated material", *Fuel*, 13, 1934: 249-256.
37. Hausen, "Survey of heat transfer theories in regenerators", *Z. fur Angw. Math und Mech.* II, 1931: 105-114.
38. L. S. Tong and A. L. London, "Heat transfer and flow-friction characteristics of woven screen and crossed-rod matrixes", Presented at Annual Meeting of ASME, 1956.
39. J. E. Coppage and Al L. London, "The periodic-flow regenerator - a summary of design theory", Presented at annual meeting of ASME, 1952.
40. J. L. Smith, "Some aspects of the selection of regenerators", *Cryogenics*, (1965): 306-314.
41. M. Kays and A. L. London, *Compact Heat Exchangers*, 3rd Ed., 1984.
42. C. Shull, K. V. Ravikumar, and T. H. K. Frederking, "Hydrodynamic characterization of perforated plate flow passages and of similar plate systems", CEC, 1993.
43. W. Rawlins and K. Timmerhaus, "Measurement of the performance of a spiral wound polyamide regenerator in a pulse tube regenerator", *Advances in Cryogenic Engineering*, 37, Part B, (1992): 947-953.
44. W. A. Steyert, "Heat transfer and flow friction in fine porous media", Submitted for publication.
45. G. Venkatarathnam and S. Sarangi, "Heat transfer and flow friction correlations in perforated plate matrix heat exchangers", *Cryogenics*, 30, (1990): 313-317.
46. M. Kaviany, *Principles of Heat Transfer in Porous Media*, New York, NY: Springer - Verlag, 1991.
47. F. W. Schmidt and A. J. Wilmott, *Thermal Energy Storage and Regeneration*, Washington, D.C.: Hemisphere, 1981.
48. J. A. Barclay, "The Theory of an Active Magnetic Regenerative Refrigerator", Published in NASA-CP-2287, 1983.
49. J. A. Barclay and S. Sarangi, *ibid.*

50. R. Li, T. Hashimoto, M. Sahashi and Y. Tohkai, "A new regenerator material $\text{Er}(\text{Ni}_{1-x}\text{Co}_x)_2$ with specific heat in the range from 4.2 K and 15 K", *Proc. 12th Int. Cryog. Eng. Conf.*, (1988): 423.
51. M. Sahashi, Y. Tokai, T. Kuriyama and H. Nakagome, *Advances in Cryogenic Engineering*, 35, (1990): 1175.
52. J. Chafe, G. Green and R. C. Riedy, "Neodymium regenerator test results in a standard Gifford McMahon refrigerator", *Proc. 7th Int. Cryocooler Conf.*, Santa Fe, NM, (1992): 605.
53. K. Bushow, J. F. Olijhoek, A. R. Miedema, "Extremely large heat capacities between 4 and 10 K", *Cryogenics*, 15, 1975.
54. I. E. Anderson, M. G. Osborne, H. Takeya and K. A. Gschneidner, Jr., "Gas atomized Er_3Ni powder for cryocooler applications", *Proc. 7th Int. Cryocooler Conf.*, Santa Fe, NM, (1992): 1120.
55. M. G. Osborne, I. E. Anderson, K. A. Gschneidner, Jr., J. Gailloux and T. W. Ellis, "Centrifugal atomization of neodymium and Er_3Ni regenerator particulate", *Proc. Cryogenic Engineering Conf.*, Albuquerque, NM, 1993; to be published in *Advances in Cryogenic Engineering* (1994).
56. E. L. Hershberg, I. E. Anderson, M. F. Hundley and J. L. Smith, "The heat capacity characteristics of Er_3Ni below 20 K", *Proc. Cryogenic Engineering Conf.*, Albuquerque, NM, 1993; to be published in *Advances in Cryogenic Engineering* (1994).
57. E. Ludeman and C. Zimm, "Production of spherical powders of rare earth intermetallic compounds for use in cryocooler regenerators", CEC, 1991.
58. C. B. Zimm, E. M. Ludeman, M. C. Severson, and T. A. Henning, *ibid.*
59. G. Green, J. Chafe, J. Stevens, J. Humphrey, "A gadolinium-terbium active regenerator", *Advances in Cryogenic Engineering*, 35, (1990): 1165-1174.
60. DeGregoria, C. B. Zimm, D. J. Janda, R. A. Lubasz, G. Jastrab, J. W. Johnson, and E. M. Luderman, "Active magnetic regenerator method and apparatus", U.S. Patent # 5,249,424, (1993).
61. J. Hall, C. E. Reid, I. Spearing, J. A. Barclay, "Thermodynamic considerations for the design of active magnetic regenerative refrigerators"; to be published at CEC, 1995.

62. J. Hall, C. E. Reid, I. Spearing, J. A. Barclay, *ibid.*
63. A. M. Tishin, "Magnetocaloric effect in strong magnetic fields", *Cryogenics*, 30, 1990.
64. Molecular field model program, Cryofuel Systems Group, University of Victoria, 1995.
65. S. M. Benford, "The magnetocaloric effect in dysprosium", *Journal of Applied Physics*, 50(3), (1979): 1868-1870.
66. Rare earth metal price quotation from David Zhang at CRE Products Inc., October 1993.
67. Dysprosium quality report, Jiangxi Provincial Rare Earth Research Institute, NanChang China, June 1993.
68. B. Bousfield, *Surface Preparation and Microscopy of Materials*, Chichester: John Wiley & Sons, 1992.
69. R. Asomoza, A. Fert, and R. Reich, *ibid.*
70. Buehler Dialog Method, *ibid.*
71. *Journal of the Less Common Metals*, 31, (1979): 1.
72. *Handbook on the Physics and Chemistry of Rare Earths*, 1, *ibid.*, pg. 186.
73. Private communication with Dr. Tim Ellis, Material Research Centre, AMES, November 1994.
74. Wohlfarth (Ed.), *Ferromagnetic Materials*, 1, Amsterdam: North-Holland Publishing, 1980.
75. A. S. Andreenko, K. P. Belov, S. A. Nikitin, and A. M. Tishin, *ibid.*
76. A. S. Andreenko, K. P. Belov, S. A. Nikitin, and A. M. Tishin, *ibid.*
77. A. S. Andreenko, K. P. Belov, S. A. Nikitin, and A. M. Tishin, *ibid.*
78. S. M. Benford, *ibid.*
79. *Landolt and Boernstein*, *ibid.*, pg. 238.

80. Private communication with Prof T. Bose, Director Hydrogen Research Institute, April, 1995.
81. Goodfellow Inc., Catalog 1994/95, Berwyn, Pa.
82. *Handbook on the Physics and Chemistry of Rare Earths*, 1, ibid, pg. 471.
83. *Ferromagnetic Materials*, 1, ibid, pp. 219, 228.
84. Goodfellow Inc., ibid.
85. *Handbook on the Physics and Chemistry of Rare Earths*, 1, ibid, pg. 637.
86. *Handbook on the Physics and Chemistry of Rare Earths*, 1, ibid, pg. 647.
87. *Handbook on the Physics and Chemistry of Rare Earths*, 1, ibid, pg. 648.
88. *Handbook on the Physics and Chemistry of Rare Earths*, 1, ibid, pg. 680.
89. *Handbook on the Physics and Chemistry of Rare Earths*, 1, ibid, pp. 678, 686.
90. W. M. Kays and A. L. London, *Compact Heat Exchangers*, ibid, pg. 4.
91. W. M. Kays and A. L. London, *Compact Heat Exchangers*, ibid, pg. 9.
92. G. Green and J. Chafe, ibid.
93. L. S. Tong and A. L. London, ibid.
94. I. Spearing, *A Numerical Model for a Rotary Active Magnetic Regenerative Refrigerator*, MSc Thesis, University of Victoria, 1995.
95. L. S. Tong and A. L. London, ibid.
96. J. A. Barclay and S. Sarangi, ibid.
97. Timmerhaus and Flynn, *Cryogenic Process Engineering*, New York: Plenum Press, 1989.
98. American Society for Metals, *Metals Handbook* (9th ed.), Z, (1984): 26.

99. American Society for Metals, *Metals Handbook*, *ibid.*, pg. 32.
100. K. S. Funke, *Development of a centrifugal atomization process for the production of large spherical metal powders*, MSc Thesis, Iowa State University, (1991): 3.
101. K. S. Funke, *ibid*, pg.4.
102. M. G. Osborne, I. E. Anderson, K. A. Gschneidner, Jr., J. Gailloux and T. W. Ellis, *ibid*.
103. K. S. Funke, *ibid*, pg.4.
104. Nuclear Metals Inc., Concord, Mass.
105. Private communication with Dr. Tim Ellis, Material Research Centre, AMES, March 1994.
106. Private communication with Dr. Jeffrey Seuntjens, Supercon Inc., March 1994.
107. J. Seuntjens, "Technical report to Cryofuel Systems (Job 2567)", Supercon Inc., July 1994.
108. J. Seuntjens, "Technical report", *ibid*.
109. J. Seuntjens, "Technical report", *ibid*.
110. K. Kratschmar, *A Pulse Tube Regenerator Test Device*, MASc Thesis, University of Victoria, not yet written.
111. Private conversation with Dr. Jeff Hall, Cryofuels System Group, August 1994.
112. S. V. Patankar, *Numerical Heat Transfer and Fluid Flow*, New York: Hemisphere Publishing, 1981.
113. J. A. Barclay and S. Sarangi, *ibid*.
114. *Landolt and Boernstein*, *ibid*.
115. *Landolt and Boernstein*, *ibid*.

Appendix A

Evaluation of the Adiabatic Temperature Change of Magnetic Materials

There are several ways to evaluate the adiabatic temperature change of magnetic materials ranging from direct temperature measurements during adiabatic applied field changes to magnetic property measurements with data manipulation.

A.1 Direct Measurement

The easiest conceivable method is to directly measure the adiabatic temperature change of the sample at a given absolute temperature as the applied field is changed. Setting up an apparatus to perform this kind of measurement is not trivial and there are very few (if any) magnetometer systems arranged to record the ΔT_{ad} .

A.2 Measurement of Specific Heat and Magnetization Data

The adiabatic temperature change of a sample can be calculated from equation 1.1 (rewritten here as Equation A.1):

$$\Delta T_{\text{ad}} = \mu_0 \int_{H_1}^{H_2} \left[\frac{T}{C_H} \left(\frac{\delta m}{\delta T} \right)_H \right] dH. \quad (\text{A.1})$$

With the magnetization and heat capacity known as a function of temperature and field, equation A.1 will provide an excellent approximation to the adiabatic temperature change. To maximize the accuracy, the absolute temperature should also be integrated as the applied field changes.

A.3 Measurement of Specific Heat Data

If the specific heat is measured as a function of temperature and applied field, the magnetic entropy change can be calculated. The entropy at zero applied field is:

$$s_0 = \int_0^T \frac{C_0}{T} dT = s_0(T). \quad (\text{A.2})$$

The entropy at some applied field is:

$$s_H = \int_0^T \frac{C_H}{T} dT = s_H(T, H). \quad (\text{A.3})$$

The specific magnetic entropy change (Δs_m) is $s_H - s_0$. With Δs_m known, the adiabatic temperature can be calculated from Equation 4.2, rewritten here as:

$$\Delta T_{\text{ad}} = \frac{T}{C_H} \Delta s_m. \quad (\text{A.4})$$

Using equation A.4 will provide only an approximation because it ignores the dependency of T/c_H on applied field.

A.4 Measurement of Magnetization Data

If the magnetization data is measured as a function of temperature and applied field, the specific magnetic entropy change can be calculated directly from Equation 4.1, rewritten here as Equation A.5:

$$\Delta S_M = \mu_o \int_{H_1}^{H_2} \left(\frac{\delta m}{\delta T} \right)_H dH. \quad (\text{A.5})$$

With Δs_m calculated, ΔT_{ad} can be found from Equation A.4 (with the same approximating considerations as above).

Appendix B

Calculations of Boundary ΔT_{ad} for a Real AMRR

B.1 Calculating $\Delta T_{ad,c}$

To calculate the $\Delta T_{ad,c}$ for the real AMRR case, Equation 2.7 is rewritten as

$$\Delta T_{ad,c} = \Delta T_c + \Delta T_{ht} + \Delta T_{void} + \Delta T_{wash} / 2. \quad (\text{B.1})$$

ΔT_c is evaluated from Equation 2.1 and is equal to 1.4 K. To calculate ΔT_{ht} , use the regenerator heat balance equation,

$$\dot{m}_f c_p (T_h - T_c) = h a_s \Delta T_{ht} \quad (\text{B.2})$$

where: $h = 3000 \text{ W/m}^2\text{K}$ (@ 175 K);
 $a_s = 43.2 \text{ m}^2$ (24,000 m^2/m^3);
 $T_h = 240 \text{ K}$;
 $T_c = 110 \text{ K}$ and,
 $c_p = 5200 \text{ J/kg.K}$ (@ 175 K).

With these values, $\Delta T_{ht} = 0.5$ K.

To get the value of $\Delta T_{void,c}$, the ratio of the fluid to fluid to total thermal mass in the no-flow region is required. The thermal mass of the solid in the no-flow region is

$$C_s = \rho_s V_{nf} (1 - \alpha) c_s \quad (\text{B.3})$$

where: $\rho_s = 8550$ kg/m³;
 $V_{nf} = V_{reg}/4 = 4.5 \times 10^{-4}$ m³;
 $c_s = 173$ J/kg.K (@ 175 K) and,
 $\alpha = 0.4$.

Again, using these values, $C_s = 400.3$ J/K. The thermal mass of the fluid in the no-flow region is

$$C_f = \rho_f V_{nf} \alpha c_p \quad (\text{B.4})$$

where: $\rho_f = 13.9$ kg/m³ (@ 175 K);
 $V_{nf} = V_{reg}/4 = 4.5 \times 10^{-4}$ m³;
 $c_p = 5200$ J/kg.K (@ 175 K) and,
 $\alpha = 0.4$.

The thermal mass of the fluid is 13.0 J/K. The ratio of the thermal mass of the fluid to the total thermal mass in the no-flow region is $C_f / (C_f + C_s) = 0.0314$. The $\Delta T_{void,c}$ is dependent on the $\Delta T_{ad,c}$ of the material as the applied field is changed, i.e. $\Delta T_{void,c} = 0.0314 \Delta T_{ad,c}$.

To calculate the ΔT_{wash} the regenerator balance equation is used again but in a slightly different form:

$$\dot{m}_f C_p (T_h - T_c) = \dot{m}_s C_s \Delta T_{\text{wash}} \quad (\text{B.5})$$

and $\dot{m}_s = 125 \text{ kg/s}$.

From this, $\Delta T_{\text{wash}} = 3 \text{ K}$. In Equation B.1, the ΔT_{wash} term is divided by 2 to get the average washing effect during the entire blow. If all the above ΔT terms are substituted into Equation B.1, the value of $\Delta T_{\text{ad,c}}$ is 3.5 K.

B.2 Calculating $\Delta T_{\text{ad,h}}$

To evaluate $\Delta T_{\text{ad,h}}$ equation 2.12 is required. An approximation will be used in this calculation by allowing $\bar{T}_h = T_h$ and $\bar{T}_c = T_c$. This simplifies the equation by eliminating recursive variables. Also, a modification must be made to reflect the change in the value of $\Delta T_{\text{void,c}}$ to $\Delta T_{\text{void,h}}$. Equation 2.12 is rewritten as:

$$\Delta T_{\text{ad,h}} = \Delta T_{\text{ad,c}} - 0.0314 \Delta T_{\text{ad,c}} + 0.0314 \Delta T_{\text{ad,h}} + \Delta T_c \left(\frac{T_h - T_c}{T_c \eta_{\text{reg}}} \right). \quad (\text{B.6})$$

To evaluate the regenerator efficiency, the total entropy generated needs to be determined (refer to Equation 2.9). The entropy terms that will be considered are \dot{S}_{ht} , \dot{S}_{cond} , \dot{S}_{void} , and \dot{S}_{other} . The pressure drop entropy is not included here because this entropy is absorbed in the fluid pump loss. All entropy terms (except \dot{S}_{other}) must be multiplied by 2 to account for the hot and cold blows for each overall cycle of the heat transfer fluid. Unless otherwise stated, all

material properties have been evaluated at 175 K. Again, the same approximation for the hot and cold end temperatures is used when evaluating these terms as was used above. Rewriting the heat transfer entropy equation gives:

$$\dot{S}_{ht} = 2 \left[\frac{\dot{Q}_r}{N_{tu} + 1} \left(\frac{1}{T_c} - \frac{1}{T_h} \right) \right] \quad (\text{B.7})$$

where: $\dot{Q}_r = \dot{m}_f c_p (T_h - T_c) = 64.9 \text{ kW}$;

$$N_{tu} = 500.$$

This gives $\dot{S}_{ht} = 1.28 \text{ W/K}$. The longitudinal conduction entropy equation is

$$\dot{S}_{cond} = 2 \left[\frac{\lambda a_c (T_h - T_c)^2}{L T_h T_c} \right]. \quad (\text{B.8})$$

The value of λ can be estimated from [113]:

$$\frac{\lambda}{\lambda_f} = \epsilon_{A1} + \left[\frac{1 - \Psi}{\frac{k_m}{\lambda_f} (1 - \epsilon_{A1})} + \frac{\Psi}{\epsilon_{A2} + \frac{k_m}{\lambda_f} \epsilon_{A3}} \right]^{-1} \quad (\text{B.9})$$

where: $\lambda_f =$ effective fluid conduction due to gas conduction and dispersion (eddy diffusivity effects) $= \dot{m}_f c_p d_p / (2a_c \alpha) = 2.1 \text{ W/mK}$;

$\epsilon_{A1}, \epsilon_{A2}, \epsilon_{A3} =$ fractions of cross sectional area devoted fluid-fluid, fluid-solid, and solid to solid conduction paths (the assumed values

are 0.3076, 0.6914, and 0.001 respectively for loose packed, 40% porous particle bed);

ψ = correlation parameter = 0.134 and,

k_m = solid conductivity = 10.7 W/mK.

With these values, $\lambda = 5.44$ W/m.K, and from Equation B.8, $\dot{S}_{\text{cond}} = 3.48$ W/K.

The fluid entrainment entropy equation is:

$$\dot{S}_{\text{void}} = 2 \left[\frac{\dot{Q}_{\text{nf}} \Delta T_{\text{nf,ave}}}{T_{\text{nf}}^2} \right] \quad (\text{B.10})$$

where: \dot{Q}_{nf} = heat transfer between fluid and solid in the no-flow region = 5.8 kW;

$\Delta T_{\text{nf,ave}}$ = average temperature difference between solid and fluid in the no-flow region = 0.53 K, and

T_{nf} = average no flow system temperature = 175 K.

The value of \dot{S}_{void} is 0.2 W/K.

The value of \dot{S}_{other} will include entropy producing mechanisms as heat leaks, bypass fluid mixing, eddy currents, friction effects and others. Rough back of the envelope calculations indicate that the magnitude of the entropy should be less than the two major entropy producing systems (longitudinal conduction and solid/fluid heat transfer). A conservative value is estimated at 1.0 W/K.

Finally, the value of η_{reg} is found from equation 2.9:

$$\eta_{\text{reg}} = \frac{\dot{W}_{\text{rev}}}{\dot{W}_{\text{act}}} = \frac{\dot{Q}_c (T_h/T_c - 1)}{\dot{Q}_c (T_h/T_c - 1) + T_h \dot{S}_{\text{gen}}}. \quad (\text{B.11})$$

With $\dot{S}_{\text{gen}} = 1.28 + 3.48 + 0.2 + 1.0 = 5.96 \text{ W/K}$, the regenerator efficiency is 36.6%.

Returning to Equation B.6 and substituting values results in a $\Delta T_{\text{ad,h}} = 8.2 \text{ K}$.

ΔT_h can be found from Equation B.1 applied to the hot end (with the appropriate substitution for ΔT_{void}):

$$\Delta T_h = \Delta T_{\text{ad,h}} - \Delta T_{\text{ht}} - 0.0314 \Delta T_{\text{ad,h}} - \Delta T_{\text{wash}} / 2. \quad (\text{B.12})$$

From Equation B.12, ΔT_h is 5.9 K.

Appendix C

Other Investigated Magnetic Refrigerants

In the process of down selecting magnetic materials with large magnetic entropy or adiabatic temperature changes and useful magnetic phase transition points, the material's magnetic phase structure was analyzed. In Section 4.2, the magnetic phase structure for several of the heavy rare earth elements are presented as well as the magnetic ordering temperatures for the Gd-Dy alloy system. Other magnetic refrigerant were investigated and prepared from different heavy rare earth alloy systems. These systems include Gd-Y, Gd-La, Gd-Ho, Gd-Er, Tb-Y, Tb-La, Tb-Dy, Tb-Ho, Tb-Er, Dy-Y, Dy-La, Dy-Ho, Dy-Er, Ho-Er, and Gd-Tb. There were a total of 56 samples made and they have predicted magnetic phase transition temperatures in the 110 K to 300 K range. All of these samples await characterization by UQTR's magnetometer to confirm transition temperatures and measure magnetization. For each of the alloy systems shown mentioned above, the transition temperature can be estimated as well as a qualitative estimate of how the magnetic entropy will be distributed from the magnetic phase diagrams. Most of these diagrams are available in *Landolt and Boernstein* [114]. If the rare earth elements are well characterized, reasonable approximations can be made for the behaviour of the alloyed systems. In the

case of alloys containing elements with no magnetic moments (e.g. yttrium and lanthanum), the magnetic moment is diluted and the phase structure of the resulting system needs to be closely studied to get an estimate of the magnetic properties. Naturally, magnetic testing is required to confirm the behaviour of any alloy system.

Other alloys have been investigated but not prepared. The most promising from this group is the Tb-Yb alloy system. Figure C.1 shows the magnetic phase diagram for this system [115].

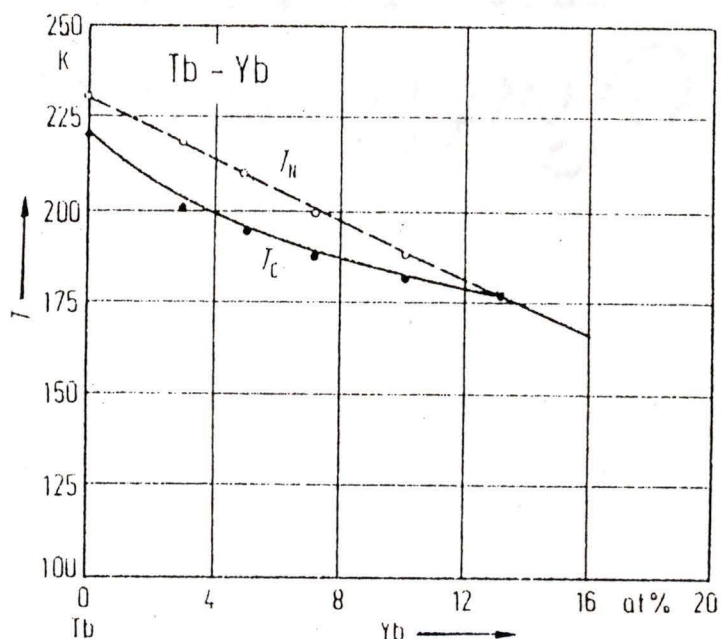


Figure C.1: Magnetic phase diagram for Tb-Yb alloy system (T_N = Neel temperature, T_C = Curie temperature).

In this system, with increasing amounts of ytterbium, the magnetic phase structure departs only slightly from ferromagnetic and even returns to ferromagnetic after approximately 14% Yb atomic weight. This is desirable

because it indicates that the magnetic entropy might be liberated in a small temperature region which leads to high entropy/unit volume and large adiabatic temperature changes. Also desirable is the fact that it requires only small amounts of diluting ytterbium to drive the transition temperature of the system down. If the alloy remains ferromagnetic at higher amounts of Yb, and the transition temperature line remains linear, it will require about 32% Yb to make a Tb-Yb alloy that has a transition temperature at 110 K. On a linear scale, this means that the Tb magnetic moment will be diluted by 32%. This would still leave a sizeable ΔT_{ad} at the cold end of the AMRR prototype (about 5 or 6 K at 6 T applied field).

Appendix D

Regenerator Simulation Computer Program

A 1-D fortran computer program was written to simulate the performance of potential AMRR regenerators. The program does a steady state entropy analysis on the given regenerators for specified operating conditions and calculates the overall figure of merit based on those input conditions. The program will also calculate a transient regenerator temperature profile to use when estimating the total effect of longitudinal conduction on the effective N_{tu} . This section of the code needs to be used in conjunction with empirical data. Figures 5.1.3a and 6.1.3a were generated using this program.

c **1-D REGENERATOR SIMULATION PROGRAM**

c
c This program calculates the figure of merit for wire screen,
c packed particles and crossed-rod regenerator geometries. The
c entropy producing effects factored into the FOM calculations
c include fluid/solid heat transfer, pressure drop, fluid carry
c over into the magnetized/demagnetized no-flow region, and
c longitudinal conduction. At present, the conduction effects
c are not calculated because adequate correlations for screen
c (and to some extent,particle) geometries could not be found. A
c transient regenerator subroutine has been written to help
c estimate the overall conduction effects but it requires
c empirical data to compare with (also in the works). The
c regenerator operation is simulated by an input data file
c supplied by the user that defined the important fluid and
c solid parameters. All output is written to a file.

c

c

c

c The following is a brief description of the subroutines in the
c program:

c

c **regen2** - main control structure, reads in user input data, calls
c main subroutines

c

c **screen** - calculates the heat transfer and pressure drop data for
c wire screen regenerators, mesh and wire diameter are variables

c

c **crossrod** - calculates the heat transfer and pressure drop data
c for crossed rod regenerators, mesh and wire diameter are variables

c

c **particle** - calculates the heat transfer and pressure drop data
c for packed particle bed regenerators, mesh and wire diameter
c are variables

c

c **exergy** - calculates the figure of merit of each regenerator
c geometry by doing an entropy production analysis, is called from
c each of the main regenerator subroutines

c

c **profile** - sets up transient profile calculations for all regenerators

c

c **solid** - calculates the solid material's transient regenerator
c temperature profile using implicit finite difference upwind scheme

c


```

if (reply .eq. 1) call screen
if (reply .eq. 2) call crossrod
if (reply .eq. 3) call particle
c write(*,*) 'Do you wish to choose another geometry? (y/n)'
c read(*,*) answer
c if (answer .eq. verify) goto 99
  stop
  end
c
c
c SUBROUTINE to calculate wire geometry regenerator properties
c
c
  subroutine screen
  implicit real*8 (a-h,o-z)
  real*8 kf,km,ntu,mesh
  common/blk1/x,y,z,flow,rho,rhomat,cp,cpmat,visc,pr,kf,km
  common/blk2/poros(50),wmesh,re(50),htarea(50),h(50),ntu(50)
  common/blk3/pdrop(50),roadmin,rodmax,rodinc,cont,fric(50)
  common/blk10/n
  dimension as(50),red(50)
  character verify/'y'/,answer

c
c select wire and mesh sizes
c
  write(*,*) 'Enter wire mesh'
  read(*,*) wmesh
  write(*,*) 'Do you wish to vary the rod diameter (y/n)'
  read(*,*) answer
  if (answer .eq. verify) then
    write(*,*) 'Enter max wire diameter (microns)'
    read(*,*) rodmax
    write(*,*) 'Enter minimum wire diameter (microns)'
    read(*,*) roadmin
    write(*,*) 'Enter wire diameter increment (microns)'
    read(*,*) rodinc
    wiremax=rodmax/1000000.0
    wiremin=roadmin/1000000.0
    wireinc=rodinc/1000000.0
    wiredia=wiremin
  else
    write(*,*) 'Enter wire diameter (microns)'
    read(*,*) wiredia

```

```

        wiredia=wiredia/1000000.0
        wiremax=wiredia
        wiremin=wiredia
        wireinc=1
    end if
c
c convert to other metric units
c
    cont=1
    mesh=wmesh/2.54*100.0
    vreg=x*y*z
    pr=visc*cp/kf
    n=1
    do while (wiredia .le. wiremax)
c
c calculate porosity (with changes to reflect the screen weaving)
c
        xtd=1/mesh
        xt=xtd/wiredia
        theta=atan(wiredia/xtd)
        poros(n)=1-3.14/4/xt
c
        xrodporos=1-3.14/4/xt
c
        poros(n)=1-(1-xrodporos)/cos(theta)
c
c calculate surface area (alpha) and hydraulic radius (as(n) is
c m**2, and htarea is m**2/m**3) (note: left as(n) same as Xrods)
c
        htarea(n)=3.14/(xt*wiredia)
        as(n)=htarea(n)*vreg
        rh=poros(n)/htarea(n)
c
c calculate fractional opening (ratio of min. free flow area
c to total frontal area, sigma in paper)
c
        fo=(xt-1)**2/xt**2
c
c calculate re (to take into account the effect of weaving angle)
c
        G=flow/(poros(n)*x*y)
        Gmax=flow/(fo*x*y)
        xrodre=4*rh*G/visc
        re(n)=xrodre*cos(theta)
        red(n)=re(n)*wiredia*htarea(n)/4/fo
c

```

```

c calculate correlation Reynold's number.
c
  if (re(n) .ge. 1800) then
    f=0.96
  else
    f=1.155-.0601*dlog10(re(n))
  end if
  reprime=re(n)*(1-f*poros(n))/(f*poros(n))
c
c calculate h and ntu
c
  st=(.375*reprime**(-.375))/pr**(2.0/3.0)
  h(n)=st*G*cp
  ntu(n)=h(n)*as(n)/(flow*cp)
c
c calculate drag coefficient (cd)
c
  cd=10**(1.33/(poros(n)**2.0)*(red(n)**(-.33))-.54/poros(n))
c
c calculate fanning friction factor (fric)
c
  thick=2.0*wiredia
  fric(n)=cd*(rh/thick)*(poros(n)/fo)**2
c
c calculate pressure drop
c
  deltap=cd*(Gmax**2.0)*z/(2.0*thick*rho)
  pdrop(n)=deltap/z
  wiredia=wiredia+wireinc
  n=n+1
  end do
  call exergy
  call output3
return
end
c
c
c SUBROUTINE crossrod calculates cross rod regenerator properties
c
c
c
  subroutine crossrod
  implicit real*8 (a-h,o-z)
  real*8 kf,km,ntu,mesh
  common/blk1/x,y,z,flow,rho,rhomat,cp,cpmat,visc,pr,kf,km

```

```

common/blk2/poros(50),wmesh,re(50),htarea(50),h(50),ntu(50)
common/blk3/pdrop(50),wiremin,wiremax,wireinc,cont,fric(50)
common/blk10/n

dimension as(50),red(50)
character verify/'y'/,answer
c
c select wire and mesh sizes
c
write(*,*) 'Enter cross rod mesh'
read(*,*) wmesh
write(*,*) 'Do you wish to vary the wire diameter (y/n)'
read(*,*) answer
if (answer .eq. verify) then
  write(*,*) 'Enter max wire diameter (microns)'
  read(*,*) rodmax
  write(*,*) 'Enter minimum wire diameter (microns)'
  read(*,*) rodmin
  write(*,*) 'Enter wire diameter increment (microns)'
  read(*,*) rodinc
  wiremax=rodmax/1000000.0
  wiremin=rodmin/1000000.0
  wireinc=rodinc/1000000.0
  wiredia=wiremin
else
  write(*,*) 'Enter wire diameter (microns)'
  read(*,*) wiredia
  wiredia=wiredia/1000000.0
  wiremax=wiredia
  wiremin=wiredia
  wireinc=1
end if
c
c convert to other metric units
c
cont=2
mesh=wmesh/2.54*100.0
vreg=x*y*z
pr=visc*cp/kf
n=1
do while (wiredia .le. wiremax)
c
c calculate porosity
c

```

```

    xtd=1/mesh
    xt=xtd/wiredia
    poros(n)=1-3.14/4/xt
c
c calculate surface area (alpha) and hydraulic radius (as(n) is
c m**2, and htarea is m**2/m**3)
c
    htarea(n)=3.14/(xt*wiredia)
    as(n)=htarea(n)*vreg
    rh=poros(n)/htarea(n)
c
c calculate fractional opening (ratio of min. free flow area
c to total frontal area, sigma in paper)
c
    fo=(xt-1)**2/xt**2
c
c calculate re
c
    G=flow/(poros(n)*x*y)
    Gmax=flow/(fo*x*y)
    re(n)=4*rh*G/visc
    red(n)=wiredia*Gmax/visc
c
c calculate correlation Reynold's number
c
    if (re(n) .ge. 1800) then
        f=0.96
    else
        f=1.155-.0601*dlog10(re(n))
    end if
    reprime=re(n)*(1-f*poros(n))/(f*poros(n))
c
c calculate h and ntu (must correct correlation for difference
c between cross rods and screens, i.e. weaving angle)
c
    theta=atan(wiredia/xtd)
    st=(.375*cos(theta)**(-.375)*reprime**(-.375))/pr**(2.0/3.0)
    h(n)=st*G*cp
    ntu(n)=h(n)*as(n)/(flow*cp)
c
c calculate drag coefficient (cd)
c
    cd=10**(1.33/(poros(n)**2.0)*(red(n)**(-.33))-0.54/poros(n))
c

```

```

c calculate fanning friction factor (fric)
c
  fric(n)=cd*(1-3.14/(4*xt))**3.0/(2*(3.14*(xt-1)**4.0/xt**5.0))
c
c calculate pressure drop
c
  thick=2.0*wiredia
  deltap=cd*(Gmax**2.0)*z/(2.0*thick*rho)
  pdrop(n)=deltap/z
  wiredia=wiredia+wireinc
  n=n+1
  end do
  call exergy
  call output3
return
end
c
c
c SUBROUTINE particle calculates particle regenerator properties
C
C
subroutine particle
implicit real*8 (a-h,o-z)
real*8 kf,km,ntu
common/blk1/x,y,z,flow,rho,rhomat,cp,cpmat,visc,pr,kf,km
common/blk2/poros(50),wmesh,re(50),htarea(50),h(50),ntu(50)
common/blk3/pdrop(50),partmin,partmax,partinc,cont,fric(50)
common/blk4/ht,ast,ac,acm,condft,condmt
common/blk10/n
dimension as(50),pdrop2(50),condm(50)
dimension vpart(50),pdrop1(50),coburnj(50),condf(50)
character verify/'y'/,answer
open (1,file='input.dat')
c
c read in particle size range
c
write(*,*) 'Do you wish to vary the particle diameter? (y/n)'
read(*,*) answer
if (answer .eq. verify) then
  write(*,*) 'Enter maximum particle diameter (microns)'
  read(*,*) partmax
  write(*,*) 'Enter minimum particle diameter (microns)'
  read(*,*) partmin
  write(*,*) 'Enter particle size increment (microns)'

```

```

    read(*,*) partinc
else
    write(*,*) 'Enter the particle diameter (microns)'
    read(*,*) partmin
    partmax=partmin
    partinc=1.0
end if
write(*,*) 'Enter the porosity'
read(*,*) void
wmesh=0
cont=3
diamax=partmax/1000000.0
diamin=partmin/1000000.0
diainc=partinc/1000000.0
nmax=(partmax-partmin)/partinc+1
vreg=x*y*z
c pr=visc*cp/kf
dp=diamin
n=1
af=x*y
ac=void*x*y
acm=(1-void)*x*y
do while (n .le. nmax)
    poros(n)=void
c
c calculate surface area (as(n) is m**2 and hteare(n) is
c m**2/m**3)
c
    vmat=vreg*(1-poros(n))
    vpart(n)=(4.0/3.0)*3.14159*(dp/2.0)**3.0
    as(n)=(vmat/vpart(n))*4.0*3.14159*(dp/2.0)**2
    ast=as(n)
    htarea(n)=((vmat/vpart(n))*4.0*3.14159*(dp/2.0)**2)/vreg
c
c calculate ntu and h
c
    G=flow/ac
    re(n)=dp*G/visc
c
c calculate h Denton's correlation (Kay's and London)
c
    coburnj(n)=0.23*re(n)**-0.3
    h(n)=(G*cp*.23*re(n)**-0.3)/pr**(2.0/3.0)
    ht=h(n)

```

```

c
c calculate ntu
c
c      ntu(n)=h(n)*as(n)/(flow*cp)
c
c calculate pressure drop/unit length using J&S correlation
c
c      reprime=flow*dp/(visc*x*y)
c      fric(n)=180.0*((1-poros(n))/reprime)+1.8
c      pdrop1(n)=fric(n)*flow**2.0*(1-poros(n))/(rho*(x*y)**2.0*dp
&          *poros(n)**3.0)
c
c calculate pressure drop/unit length using T&F correlation
c
c      pdrop2(n)=((1-poros(n))/poros(n))*(285*(1-poros(n))**2.0
&          /poros(n)/re(n)+1.75)*G**2.0/dp/rho
c
c calculate average pressure drop/unit length
c
c      pdrop(n)=(pdrop1(n)+pdrop2(n))/2.0
c
c calculate conductivities (effective fluid and solid cond.)
c
c      condf(n)=flow*cp*dp/(2*ac)
c
c input effective fluid conductivities for transient profile
c
c      write(*,*) 'Enter the effective fluid conductivity (W/m.K)'
c      read(*,*) condft
c      condm(n)=km
c      condmt=condm(n)
c
c call subroutine to calculate transient temperature profile
c
c      write(*,*) 'Do you want a transient profile? (y/n)'
c      read(*,*) answer
c      if (answer .eq. verify) then
c          call profile
c      end if
c      dp=dp+diainc
c      n=n+1
c          end do
c          call output3
c          call exergy

```

```

return
end
c
c subroutine exergy to calculate the figure of merit for each
c geometry type
c
c subroutine exergy
c
implicit real*8 (a-h,o-z)
real*8 kf,km,ntu,mnf
common/blk1/x,y,z,flow,rho,rhomat,cp,cpmat,visc,pr,kf,km
common/blk2/poros(50),wmesh,re(50),htarea(50),h(50),ntu(50)
common/blk3/pdrop(50),roadmin,rodmax,rodinc,cont,fric(50)
common/blk10/m
common/blk9/sht(50),spd(50),svoid(50),sgen(50),fom(50)
c
c
c equations to calculate entropy produced
c
th=240
tc=110
deltc=3.5
delth=8.4
deltnf=(deltc+delth)/2
freq=5
tave=(240+110)/2
qreg=flow*cp*(th-tc)
qload=700
wrev=qload*(th/tc-1)
regvol=x*y*z
totvol=regvol*3
flvol=flow/rho
n=1
nmax=m-1
do while (n .le. nmax)
  sht(n)=2*qreg/(ntu(n)+1)*(1/tc-1/th)
  spd(n)=2*flvol*pdrop(n)*z/th
  if (poros(n) .gt. 0.4) then
    factor=(1-poros(n))/(1-0.4)
    freq=5*factor
  else
    freq=5
  end if
  mnf=poros(n)*totvol*rho*freq

```

```

    qnf=mnf*cp*deltmf
    acnf=htarea(n)*totvol/12
    hnf=h(n)/3
    deltsf=qnf/(hnf*acnf)
    svoid(n)=2*(qnf*deltsf/tave**2)
    sgen(n)=sht(n)+spd(n)+svoid(n)
    fom(n)=wrev/(wrev+th*sgen(n))
    n=n+1
end do
call output4
return
end
c
c
c subroutine profile
c
c subroutine to calculate transient temp profiles
c
implicit real*8 (a-h,o-z)
real*8 kf,km
common/blk1/x,y,z,flow,rho,rhomat,cp,cpmat,visc,pr,kf,km
common/blk5/xstep,u,bfluid,bsolid,gammaf,gammas,apo,ndnum
common/blk6/tfo(150),tso(150),tf(150),ts(150),tn(150)
common/blk7/etime,tstep
c
c set time and space steps
c
write(*,*) 'Enter the value of the time step (sec)'
read(*,*) tstep
ndnum=100.0
xstep=z/ndnum
u=flow/(rho*ac)
bfluid=ht*ast/(ac*cp*z)
bsolid=ht*ast/(acm*z)
gammaf=condft/cp
gammas=condmt
apo=rhomat*cpmat*xstep/tstep
etime=0
diff=1000
c
c initialize grid
c
ti=300
do 10 i=1,ndnum

```

```
    tfo(i)=ti
    tso(i)=ti
    tf(i)=ti
    ts(i)=ti
10  continue
c
c  set up iteration loop
c
  do while (diff .gt. .1)
  call fluid
c
c  transfer data from tri-diagonal matrix solver to fluid temps
c
  do 20 i=1,ndnum
    tf(i)=tn(i)
20  continue
  call solid
c
c  transfer data from tri-diagonal matrix solver to solid temps
c
  do 30 i=1,ndnum
    ts(i)=tn(i)
30  continue
c
c  check tolerance
c
  diff=tf(1)-tf(ndnum)
c
c  store old temperature values
c
  do 40 i=1,ndnum
    tfo(i)=tf(i)
    tso(i)=ts(i)
40  continue
  etime=etime+tstep/60
  call output1
  call output2
  end do
  return
  end
c
c  subroutine solid will calculate the fluid temperature profile
c  at individual time steps
c
```

```

subroutine solid
implicit real*8 (a-h,o-z)
real*8 kf,km
common/blk1/x,y,z,flow,rho,rhomat,cp,cpmat,visc,pr,kf,km
common/blk4/ht,ast,ac,acm,condft,condmt
common/blk5/xstep,u,bfluid,bsolid,gammaf,gammas,apo,ndnum
common/blk6/tfo(150),tso(150),tf(150),ts(150),tn(150)
common/blk8/const(150),a(150),b(150),c(150)
tsurr=320
aw=gammas/xstep
ae=gammas/xstep
ap=ae+aw+apo+bsolid*xstep
const(1)=bsolid*tf(1)*xstep/2.0+apo/2.0*tso(1)-ht*tsurr
b(1)=ae+apo/2.0+bsolid*xstep/2.0-ht
c(1)=-ae
do 10 i=2,ndnum-1
  a(i)=-aw
  b(i)=ap
  c(i)=-ae
  const(i)=bsolid*tf(i)*xstep+apo*tso(i)
10 continue
const(ndnum)=bsolid*tf(ndnum)*xstep/2.0
&          +apo/2.0*tso(ndnum)+ht*tf(ndnum)
a(ndnum)=-aw
b(ndnum)=aw+apo/2.0+bsolid*xstep/2.0+ht
call tdm
return
end
c
c subroutine fluid will calculate the fluid temperature profile
c at individual time steps
c
subroutine fluid
implicit real*8 (a-h,o-z)
real*8 kf,km
common/blk1/x,y,z,flow,rho,rhomat,cp,cpmat,visc,pr,kf,km
common/blk4/ht,ast,ac,acm,condft,condmt
common/blk5/xstep,u,bfluid,bsolid,gammaf,gammas,apo,ndnum
common/blk6/tfo(150),tso(150),tf(150),ts(150),tn(150)
common/blk8/const(150),a(150),b(150),c(150)
f=rho*u
d=gammaf/xstep
peclet=f/d
c

```

```

c try upwind scheme (i.e. a(|pecllet|)=1)
c
  apeclet=1
  aw=d+f
  ae=d
  ap=ae+aw+bfluid*xstep
  const(1)=aw*320+bfluid*ts(1)*xstep
  b(1)=ap
  c(1)=-ae
  do 10 i=2,ndnum-1
    a(i)=-aw
    b(i)=ap
    c(i)=-ae
    const(i)=bfluid*ts(i)*xstep
10 continue
  const(ndnum)=ae*tf(ndnum)+bfluid*ts(ndnum)*xstep
  a(ndnum)=-aw
  b(ndnum)=ap
  call tdm
  return
end
c
  subroutine tdm
c
c This subroutine will invoke a tridiagonal matrix solver to solve
c for temperature arrays imported from other subroutines.
c
c
c
  implicit real*8 (a-h,o-z)
  common/blk5/xstep,u,bfluid,bsolid,gammaf,gammas,apo,ndnum
  common/blk6/tfo(150),tso(150),tf(150),ts(150),tn(150)
  common/blk8/const(150),a(150),b(150),c(150)
  dimension gam(150)
c
c begin matrix solving (tridiagonal matrix solver from Numerical
c Recipes)
c
  bet=b(1)
  tn(1)=const(1)/bet
  do 10 i=2,ndnum
    gam(i)=c(i-1)/bet
    bet=b(i)-a(i)*gam(i)
    tn(i)=(const(i)-a(i)*tn(i-1))/bet
10 continue

```

```

do 20 i=ndnum-1,1,-1
  tn(i)=tn(i)-gam(i+1)*tn(i+1)
20 continue
return
end

```

c

c This subroutine will output the fluid transient data to a file
c called fluid.dat.

c

```
subroutine output1
```

c

```

common/blk5/xstep,u,bfluid,bsolid,gammaf,gammas,apo,ndnum
common/blk6/tfo(150),tso(150),tf(150),ts(150),tn(150)
common/blk7/etime,tstep
implicit real*8 (a-h,o-z)
open(1,file='fluid.dat',access='append')
if (etime .eq. tstep/60) then
  write(1,40)
  write(1,50)
  write(1,60)
end if
write(1,100) etime,tf(1),tf(25),tf(50),tf(75),tf(100)
40 format("TITLE = \"Fluid Temperature Profile\"")
50 format("VARIABLES= \"Etime\", \"HotEnd\", \"1/4\", \"1/2\", \"3/4\", \"ColdEnd\"")
60 format("ZONE T= \"Fluid\"")
100format(f6.3,1x,5f8.3)
return
end

```

c

c This subroutine will output the solid transient data to a file
c called solid.dat.

c

```
subroutine output2
```

c

```

common/blk5/xstep,u,bfluid,bsolid,gammaf,gammas,apo,ndnum
common/blk6/tfo(150),tso(150),tf(150),ts(150),tn(150)
common/blk7/etime,tstep
implicit real*8 (a-h,o-z)
open(1,file='solid.dat',access='append')
if (etime .eq. tstep/60) then
  write(1,40)
  write(1,50)
  write(1,60)
end if

```

```

write(1,100) etime,ts(1),ts(25),ts(50),ts(75),ts(100)
40format('TITLE = "Solid Temperature Profile"')

50 format('VARIABLES="Etime","HotEnd","1/4","1/2","3/4","ColdEnd"')
60 format('ZONE T="Solid"')
100format(f6.3,1x,5f8.3)
return
end
c
c
c subroutine output3 to write property results
c
c subroutine output3
c
implicit real*8 (a-h,o-z)
real*8 ntu
common/blk2/poros(50),header,re(50),htarea(50),h(50),ntu(50)
common/blk3/pdrop(50),varmin,varmax,varinc,cont,fric(50)
if (cont .eq. 1) then
open (2,file='screenout.dat')
write(2,*) 'TITLE="These data are for screens"'
write(2,*) 'VARIABLES=poros,dwire,re,htarea,h,ntu,pdrop,fric'
end if
if (cont .eq. 2) then
open (2,file='rodout.dat')
write(2,*) 'TITLE="These data are for crossrods"'
write(2,*) 'VARIABLES=poros,dwire,re,htarea,h,ntu,pdrop,fric'
end if
if (cont .eq. 3) then
open (2,file='partout.dat')
write(2,*) 'TITLE="These data are for particles"'
write(2,*) 'VARIABLES=porosity,dp,re,htarea,h,ntu,pdrop,fric'
end if
write(2,20) header
size=varmin
i=1
do while (size .le. varmax)
write(2,25) poros(i),size,re(i),htarea(i),h(i),ntu(i),pdrop(i),
& fric(i)
size=size+varinc
i=i+1
end do
20 format('ZONE T="Mesh = ',f6.1)
25 format(f5.2,f7.1,f7.1,1x,f7.0,1x,f6.0,1x,f5.0,1x,f8.0,f7.4)

```

```

30 format(f9.4)
   return
   end
c
c
c subroutine output4 to write property results
c
   subroutine output4
c
   implicit real*8 (a-h,o-z)
   real*8 ntu
   common/blk2/poros(50),header,re(50),htarea(50),h(50),ntu(50)
   common/blk3/pdrop(50),varmin,varmax,varinc,cont,fric(50)
   common/blk9/sht(50),spd(50),svoid(50),sgen(50),fom(50)
   if (cont .eq. 1) then
     open (2,file='fomscreen.dat')
     write(2,*) 'TITLE="These data are for screens"'
     write(2,*) 'VARIABLES=re,poros,size,sht,spd,svoid,sgen,fom'
   end if
   if (cont .eq. 2) then
     open (2,file='fomrod.dat')
     write(2,*) 'TITLE="These data are for crossrods"'
     write(2,*) 'VARIABLES=re,poros,size,sht,spd,svoid,sgen,fom'
   end if
   if (cont .eq. 3) then
     open (2,file='fompart.dat')
     write(2,*) 'TITLE="These data are for particles"'
     write(2,*) 'VARIABLES=re,poros,size,sht,spd,svoid,sgen,fom'
   end if
   write(2,20) header
   size=varmin
   i=1
   do while (size .le. varmax)
     write(2,25) re(i),poros(i),size,sht(i),spd(i),svoid(i),sgen(i),
     &           fom(i)
     size=size+varinc
     i=i+1
   end do
20 format('ZONE T="Mesh = ',f6.1)
25 format(f6.2,f6.2,2x,f7.2,2x,f6.3,2x,f6.3,2x,f5.3,2x,f6.3,2x,f5.3)
30 format(f9.4)
   return
   end

```

VITA

Surname: Reid
Given Names: Christopher Edwin John
Place of Birth: Fort William, Ontario
Date of Birth: 65/07/07

Education Institutions Attended

University of Victoria 1992 to 1995
University of Manitoba 1986 to 1990

Degrees Awarded

M.A. Sc. University of Victoria 1995
B.A.Sc. University of Manitoba 1990

Publications

1. C. E. Reid, J. A. Barclay, J. L. Hall, and S. Sarangi, "Selection of magnetic materials for an active magnetic regenerative refrigerator", *Journal of Alloys and Compounds*, 207/208 (1994): 366-371.
2. C. E. Reid and T. Villa, "A pneumatic vibration dissipator", U.S. Patent, 1995.

Partial Copyright Licence

I hereby grant the right to lend my thesis to users of the University of Victoria Library, and to make single copies only for such users or in response to a request from the Library of any other university, or similar institution, on its behalf or for one of its users. I further agree that permission for extensive copying of this thesis for scholarly purposes may be granted by me or a member of the University designated by me. It is understood that copying or publication of this thesis for financial gain shall not be allowed without my written permission.

Title of Thesis: Development of Magnetic Refrigerants for Active Magnetic Regenerative Refrigerators

Author:

A large black rectangular redaction box covers the author's signature. A horizontal line extends from the right side of the box.

(Signature)

CHRISTOPHER EDWIN JOHN REID

(Name in Block Letters)

May 31, 1995

(Date)